Materials & Design 222 (2022) 111063

Contents lists available at ScienceDirect

Materials & Design

journal homepage: www.elsevier.com/locate/matdes

In-situ monitoring of sub-surface and internal defects in additive manufacturing: A review

Youssef AbouelNour *, Nikhil Gupta

Composite Materials and Mechanics Laboratory, Mechanical and Aerospace Engineering Department, New York University, Tandon School of Engineering, 6 MetroTech Center, Brooklyn, NY 11201, USA

HIGHLIGHTS

- In-situ process monitoring methods can create a closed-loop AM process capable of defect correction and control, to ensure process stability and repeatability.
- Integration of monitoring methods and machine learning in the AM process can help in continuously evaluating the quality of material deposition and developing intervention methods for correcting the defects in-situ.
- Simultaneous use of imaging methods provides a way to study melt pool dynamics in 3D and detect sub-surface defects in printed components with sizes as small as 50 μm.
- When combined with data fusion concepts, ex-situ validation using XCT can lead to an in-depth evaluation of defects, as well as an assessment of the quality of in-situ monitoring methods.

GRAPHICAL ABSTRACT

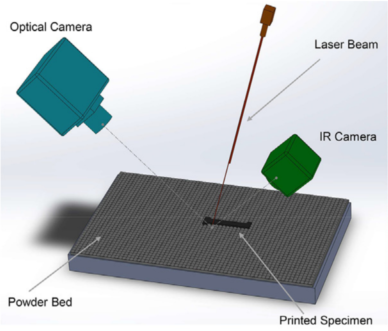

Figure 1: An off-axis optical systems presenting use of an optical camera and an IR camera for in-situ monitoring of a LPBF process printing a standard dog-bone specimen.

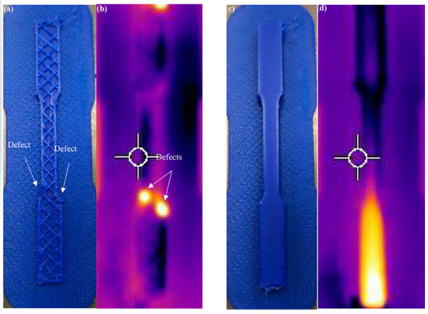

Figure 2: (a-b) Defects detected mid-process using monitoring methods (i.e., visual and thermal imaging, respectively) cannot be seen in (c-d) visual and thermal images of the final part.

ARTICLE INFO

Article history:
Received 5 November 2021
Revised 7 July 2022
Accepted 12 August 2022
Available online 18 August 2022

Keywords:
Real-time process monitoring
In-situ monitoring
Imaging methods
Acoustic methods

ABSTRACT

Additive Manufacturing (AM), or 3D printing, processes depend on a user-defined set of optimized process parameters to create a component. Monitoring and control of AM processes in real-time can help achieve process stability and repeatability to produce high quality parts. By applying in-situ monitoring methods to the AM process, defects in the printed parts can be detected. In this review, application of both imaging and acoustic methods for the detection of sub-surface and internal defects is discussed. Imaging methods consist of visual and thermal monitoring techniques, such as optical cameras, infrared (IR) cameras, and X-ray imaging. Many studies have been conducted that prove the reliability of imaging methods in monitoring the printing process and build area, as well as detecting defects. Acoustic methods rely on acoustic sensing technologies and signal processing methods to acquire and analyze acoustic signals, respectively. Raw acoustic emission signals can correlate to particular defect mechanisms using

---

* Corresponding author.
E-mail addresses: ywa201@nyu.edu (Y. AbouelNour), ngupta@nyu.edu (N. Gupta).

https://doi.org/10.1016/j.matdes.2022.111063
0264-1275/

Defect detection
Signal processing

methods of feature extraction. In this review, representation and analysis of the acquired in-situ data from both imaging and acoustic methods is discussed, as well as the means of data processing. Ex-situ testing techniques are introduced as methods for verification of results gained from in-situ monitoring data.

1. Introduction

In an Additive Manufacturing (AM) process, a computer-aided design (CAD) file is created and sliced for manufacture by a layer-by-layer material deposition process. AM has proven to be a flexible and cost-efficient technique. It eliminates many constraints that are imposed on geometry, material, and time by conventional manufacturing methods. As the adoption of AM methods in industrial scale production increases, the need to address the consistency and efficiency of these technologies has emerged. Some studies have focused on making the process more energy- and resource-efficient by recycling excess printing material, reducing waste, and reducing resource consumption [1–4]. This review focuses on monitoring techniques to track, analyze, and limit defects that occur in AM.

In-situ monitoring methods have been applied to all seven AM classes, as categorized by the ASTM F42 standard, to better understand the events that occur during an AM build. In-situ, or in-process, monitoring, offers a resourceful way to track and control the print quality by enabling defect detection, reducing material wastage, and providing a means of defect correction [5–7].

For print quality control, AM processes depend on a user-defined set of optimized process parameters such as printing temperature, laser power, printing process speed and sample orientation. They are also affected by external factors like the quality and consistency of the filament or binder, impurities in the feed powder, vibrations in the system, or power surges [8]. The dependence of AM on a number of internal and external factors decreases process stability and repeatability, which can lead to defect formation in the printed part. Defects can form either on the surface of the geometry, in the sub-surface, or internally, affecting the part's integrity and mechanical properties. Surface defects appear on the top layer of the print. Sub-surface defects occur at $\sim$ 1–500 μm below the top layer of the print. They can be visualized in-situ due to the penetration of light in the region of interest (ROI) and reflection back to the monitoring device, as gathered from various articles reviewed in this work. Internal defects occur at depths > 500 μm from the surface. Both sub-surface and internal defects can appear in different forms such as pores, voids, or internal cracks in the process zone. These will be defined in more detail in *Section 2*.

Integration of monitoring methods in the AM process can help in continuously evaluating the quality of material deposition and developing intervention methods for correcting the defects as soon as they start to evolve. The optimization of in-situ monitoring methods has benefited greatly from research conducted to monitor the consolidation of the feed material in the build area for understanding and analyzing the effects of process parameters on AM build quality (*see* Tables 1 and 2*)*. The focus of recent research has been on gathering critical information about defect formation: events leading up to defect formation and after continuation of the print [9]. Furthermore, current research is geared towards predicting and alternating the process parameters of the machine by integrating Machine Learning (ML) within the in-situ monitoring system to create a closed-loop control process.

In accordance with the growing widespread interest in in-situ monitoring for AM processes, authors have continuously reviewed and classified the existing literature. A comprehensive review of in-situ monitoring and metrology of metal-based AM is presented in [10]. This includes both powder bed fusion (PBF) and directed energy deposition (DED). Similarly, inclusive reviews of in-situ monitoring in material extrusion processes are presented in [11] and [12]. A review based on multi-sensor process monitoring and data fusion techniques in AM is given in [13]. Other authors reviewed literature specific to a single AM process and classified studies based on the utilized methods or outcomes. For PBF, a recent thorough review based on a classification of in-situ measurement levels is provided in [14], a review presenting a different classification of in-situ sensing methods and control requirements is provided in [15], and one based on image processing of acquired in-situ data is provided in [16]. For DED, in-situ monitoring is covered in great detail in [17].

Here, a more comprehensive overview of in-situ monitoring in AM is presented. This review offers a categorization of defects and defect formation mechanisms based on imaging and acoustic methods. It also presents a variety of different monitoring and signal processing methods that can be used in synchrony for in-situ defect detection, as well as a framework for their simultaneous use, which has not been presented before.

In this review, in-situ monitoring methods will be classified into two distinct categories: imaging methods and acoustic methods. Both offer an efficient, non-destructive testing (NDT) technique to trace the onset or propagation of sub-surface and internal defects in components printed using AM processes. Other measurement techniques, such as interferometry, IR spectroscopy, and impedance testing, have also been used with AM methods for data collection and process stability analysis. Tables 1 and 2 present an overview of studies in which in-situ monitoring methods were used in the seven classes of AM. The tables highlight whether monitoring was done on the surface of the component or in the sub-surface and internally. As observed in the tables, in-situ monitoring methods have been used for build area monitoring, process optimization, and data collection for all AM classes other than sheet lamination.

In a PBF process, parameters such as behavior of the powder material in each layer, the laser scanning velocity, energy output, temperature fields, and oxygen content have been measured and analyzed to study the melt pool [18–25]. For vat photopolymerization, in-situ monitoring has been conducted to study curing conditions and material properties [26–37]. For binder jetting, droplet sensing and surface defect detection have been performed using a variety of in-situ monitoring methods [38–47]. In DED, studies covered experiments on both metal powder and metal wire material deposition for analysis of the melt pool and concepts such as temperature distributions and melting modes during powder deposition [48–75] and wire deposition [76–79]. Other studies in DED focused on defect detection and control of part properties [80–91]. For material jetting, impedance testing has been used for defect detection [92,93].

For material extrusion, filament bonding failures, material properties, and part quality have been studied [94–111]. One common conclusion from monitoring all AM processes is the influence of process parameters on the printing process. Thus, studying material properties and metrology needs in AM is a key aspect to

Table 1

Research studies on in-situ monitoring of vat photopolymerization, binder jetting, DED, material jetting and sheet lamination.

In-situ Monitoring Method	Devices Used	Monitoring Objective	Reference
Vat Photopolymerization			
Polymers			
IR Spectroscopy; Thermography	NIR spectrometer; Pyrometer	Chemical composition, temperature	[26]
Thermography	IR Camera	Temperature profiles	[27]
Thermography	Pyrometer	Reaction parameters, monomer structures	[28]
Interferometry	Mach-Zehnder interferometer; DMD	Height of cured parts, curing conditions	[29 30 31 32 33]
IR Spectroscopy; Ultrasonic Reflectometry	NIR spectrometer; US cell	Chemical composition, curing conditions **	[34]
Thermography	IR Camera	Curl distortion, curing conditions	[35]
IR Spectroscopy	NIR spectrometer	Material perturbation †	[36]
X-ray micro-tomography	Synchrotron X-ray 3D Imaging	Effects of induced defects; Deformation behavior **	[37]
Binder Jetting			
Liquid Materials; inks			
Visual Imaging	Optical camera	Droplet speeds	[38]
Visual Imaging	Optical camera; Piezo sensor	Droplet jetting behavior, Defect Detection	[39]
Micro-sensing	Transmissive sensor	Droplet sensing, Defect Detection	[40]
Impedance Testing; Visual Imaging	*T*-junction waveguide; Optical camera	Droplet sensing, data collection	[41 42]
Other Materials			
Visual Imaging; Thermography	Optical camera; IR Camera	Data collection, Defect Detection	[43]
X-ray Imaging	X-ray imaging system	Droplet sensing, droplet analysis	[44]
Acoustic Emissions; Quasi-static Indentation	AE sensors	Failure modes, Defect Detection **	[45 46]
Visual Imaging; Scalar Diffraction	Optical camera	Defect Detection, quality control	[47]
Directed Energy Deposition (DED)			
Metal Powders			
Thermography; Sensing	IR Camera; Optoelectronic sensor	Melt pool analysis, temperature distributions, Defect Detection	[48 49]
Thermography	Pyrometers	Melt pool analysis, temperature distributions	[50 51 52 53 54]
Visual Imaging; Thermography	Optical cameras; Pyrometers	Melt pool analysis, temperature distributions	[55 56 57 58]
Thermography	IR Camera; Pyrometers	Melt pool analysis, temperature distributions	[59 60 61]
Thermography	IR Camera	Melt pool analysis, temperature distributions, deposition process	[62 63 64 65 66]
Visual Imaging	Optical camera	Deposition process, temperature distributions	[67 68]
Thermography	Pyrometers; PSU computer	Deposition Process, temperature distributions, defect correction	[69 70 71]
Acoustic Emissions	Acoustic sensors/transducers	Process conditions, quality monitoring, crack initiation **	[80 81 82 83 84]
Visual Imaging	Optical spectrometer	Composition analysis	[85]
Visual Imaging	Optical spectrometer	Defect Detection **	[86]
Acoustic Emissions	Acoustic sensors	Powder mass flow rate measurement **	[87]
Acoustic Emissions	Acoustic sensors	Data collection, Defect Detection **	[88 90]
X-ray Imaging	X-ray imaging system	Melt pool analysis, melting modes, powder flow rates	[72 73 74 75]
Metal Wire			
Thermography	Pyrometers	Melt pool analysis, temperature distributions	[76]
Thermography	IR Camera	Deposition process, temperature distributions	[77]
Visual Imaging	Optical Spectrometer; Optical camera	Deposition process, temperature distributions	[78 79]
Visual Imaging	Optical camera; 3D scanner	Deposition process, in-process control	[89]
Acoustic Emissions	Pre-polarized Microphone	Defect Detection **	[91]
For more information about DED processes, see [10].			
Material Jetting			
Polymers			
Impedance Testing	Piezoelectric ceramic (PZT); AE sensors	Defect Detection **	[92 93]
Sheet Lamination			
No significant in-situ monitoring research to date.			

Note: ** indicates the study was conducted for sub-surface or internal measurement.
† indicates the study was done on ceramic materials, not polymers.
"Acoustic sensors" are indicative of piezoelectric sensors only; other acoustic sensors are explicit.

Table 2
Research studies on in-situ monitoring of PBF and material extrusion.

In-situ Monitoring Method	Devices Used	Monitoring Objective	Reference
Powder Bed Fusion (PBF)			
Laser			
Thermography	IR Camera; Pyrometer	Device integration	[123]
Visual Imaging; Thermography	Optical cameras; Pyrometer	Device integration	[124 125 126 127]
Visual Imaging	Optical cameras	Device integration	[128]
Visual Imaging	Optical camera; Photodiode	Melt pool analysis	[129 130 131 132 133]
Visual Imaging	Optical camera	Powder consolidation, powder bed and melt pool analysis	[134 135 136 137 138 139]
Visual Imaging	Optical camera	Melt pool analysis, data collection for machine learning and defect detection	[140 141 142 143]
Visual Imaging	Optical camera; Photodiode	Defect Detection, defect correction	[144]
Thermography	IR Camera	Melt pool analysis	[145]
Visual Imaging; Thermography	Optical camera; Pyrometer	Powder consolidation, melt pool analysis	[23 25 146 147]
Thermography	IR Camera	Melt pool analysis	[148 149 150 151 152 153 154 155]
Thermography	Pyrometers	Powder consolidation	[24]
Thermography	Thermocouple; Transducer	Temperature distributions, melt pool stability	[156 157]
Visual Imaging; Thermography	Optical cameras; Pyrometers	Defect Detection	[158 159 160 161]
Thermography; Acoustic Emissions	IR Camera; Acoustic sensors	Data collection, signal processing, Defect Detection **	[162]
Thermography; X-ray Imaging	IR Camera; Optical camera; X-ray imaging	Defect Detection **	[20]
Visual Imaging/High-fidelity Video	High frame-rate optical camera	Melt pool analysis, powder consolidation	[22 100 163 164]
Visual Imaging/High-fidelity Video	High frame-rate optical camera	Melt pool analysis, melting modes	[165 166 167 168 169 170 171]
Visual Imaging/High-fidelity Video; Thermography	High frame-rate optical camera; Pyrometer	Melt pool analysis, data collection and analysis, part quality **	[172]
Visual Imaging	High-resolution optical camera; Projector	Fringe projection for surface topography measurements	[173]
X-ray Imaging	X-ray imaging system	Melt pool analysis, melting modes **	[73 174 175 176 177 178 179 180]
Visual Imaging; Thermography; XCT	Optical camera; IR Camera; X-ray imaging	Defect Detection **	[181 182]
Acoustic Emissions	Acoustic sensors	Density measurements, part quality **	[183]
Acoustic Emissions	Acoustic sensors	Defect Detection **	[117 170 184 185 186]
Acoustic Emissions	Acoustic sensors	Data collection, process quality monitoring **	[187 188]
Acoustic Emissions	FBG sensor	Defect Detection **	[189 190]
Acoustic Emissions	Pre-polarized Microphone	Defect Detection **	[191 192 193 194]
Acoustic Emissions	Pre-polarized Microphone	Melt pool analysis, feature extraction	[195 196 194]
Acoustic Emissions	FBG sensor	Data collection, process quality monitoring **	[197]
Interferometry	Interferometer (ICI device)	Process stability, melt pool analysis **	[198 199 200]
Thermography; Interferometry	IR Camera; Pyrometer; Microphone	Comparison of sensor characteristics; defect detection **	[201]
Electron Beam			
Thermography	IR Camera	Defect Detection	[202 203 204 205]
Thermography	IR Camera	Parameter and melt pool analysis, surface quality	[206 207 208 209 210]
Thermography; XCT	IR Camera; CT scanning	Defect Detection, defect correction **	[211 212]
Material Extrusion (i.e., Fused Filament Fabrication (FFF))			
Visual Imaging	Optical camera	Data collection, defect detection	[94 108]
Visual Imaging	Optical camera	Part quality, geometry profile	[109 110]
Visual Imaging	Laser triangulation system	Device integration, data collection	[95]
Visual Imaging	Digital microscopes	Defect Detection, defect correction	[121]
Visual Imaging	Optical cameras; LEDs	Defect Detection, data correlation	[213]
Thermography	IR Camera	Emissivity measurement and correction **	[96]
Acoustic Emissions	Acoustic sensors	Filament breakage (using polymers)	[97 98]
Acoustic Emissions	Acoustic sensor/accelerometer	Data collection, defect detection, process failures **	[99 100 101 102]
Visual Imaging; XCT	µCT	Tool path prediction	[103]
Acoustic Emissions	Transducers	Filament bonding failures, process inspection	[104]
Acoustic Emissions	Acoustic sensors; Transducers	Filament bonding failures	[105]
Acoustic Emissions	Doppler vibrometer; Transducer	Data collection, defect detection	[106]
Thermography; Acoustic Emissions	FBG sensors; Thermocouples	Residual strain, temperature profiles	[111]
Acoustic Emissions	Acoustic sensors	Defect Detection **	[107]

Note: ** indicates the study was conducted for sub-surface or internal measurement.
Unless otherwise noted, research on PBF processes utilized metal powders as the feed material.
Unless otherwise noted, research on material extrusion processes utilized ABS as the feed material.
"Acoustic sensors" are indicative of piezoelectric acoustic sensors only; other acoustic sensors are explicit.

understanding the influence of the numerous parameters on the build quality [112,113].

Three major focus areas of research on AM in-situ monitoring over the past few years are: (1) integrating methods to monitor the sub-surface of the printed geometry for defects and shape of the build area or melt pool, (2) integrating methods to track temperature distributions and acoustic emissions within the printed part for internal defect detection, and (3) applying ML algorithms to correct 3D prints in real-time using the data acquired from monitoring methods. The majority of this research has been conducted on two AM processes, PBF and Fused Filament Fabrication (FFF), which is a classification of material extrusion processes. These AM processes will constitute the focus of this review.

2. Defect characterization

A variation in optimum process parameters or the occurrence of thermal distortion in the system can develop microstructural changes in the build that can lead to the formation of defects [114,115]. Generally, any undesired features present in the structure of a part is termed as a defect. Although the defects can range from undesired microstructural deviation and geometrical distortions, the present work is focused on only the undesired geometrical features present in the manufactured parts. Types of defects observed in parts manufactured by AM include pores, voids, cracks, balling, lack-of-fusion (LoF) voids, delamination, warping, and keyhole porosity [8,20,108,116–119]. Delamination and warping are specific to FFF processes, while LoF voids, balling, and keyhole porosity are specific to metal-based AM processes, such as PBF or DED. In addition, while delamination, warping, and balling are considered only as surface defects due to their visibility on the top layer or outside perimeter of a printed part, all other types of defects listed above can occur on the surface, sub-surface, or internal of the part.

Cracking mainly results from thermal and tensile stresses within the part. Cracks tend to form along grain boundaries [6]. They can appear both during the printing process or in the aftermath due to microstructural changes in the printed part. In metal-based printing, voids occur due to LoF and trapped gases in the part, which form in metal powder due to the melting process [119]. In FFF, voids occur due to a variety of reasons, such as underfill, incorrect process parameters, or a clogged nozzle [11]. Balling, or melt ball formation, occurs when molten material forms into spheres rather than solidified layers due to inadequate laser-powder bed interaction. Defect formation in PBF and FFF processes will be discussed in detail to facilitate the understanding of sub-surface and internal defect detection.

2.1. Defect formation in fused filament fabrication

FFF refers to an extrusion-based AM process in which bulk material is melted in a chamber by a heat source then extruded under pressure using a tractor-feed system [120]. Important process parameters are the number of outer layers, infill degree, infill type/pattern, sample orientation on the build plate, infill rate (or printing speed), layer thickness, and printing temperature. In an FFF process, the material that is being extruded from the nozzle must be in a semisolid state to properly bond to the solid structure [120]. Therefore, the molten material in the nozzle and reservoir must be maintained at the correct temperature. The temperature differential between the chamber and the surrounding atmosphere should be kept at a minimum and the cooling process should be controlled [96].

In FFF, mechanical stresses are the main driver to defect formation. They are driven by factors such as process parameters, part size, and temperature distributions [121]. The higher the heat transfer between layers, the better adhesion between them, which limits delamination and warping, leads to smaller voids in the printed part, and produces parts with better mechanical properties [122]. Low adhesion can cause internal stresses in the part. Furthermore, when a layer is printed, it undergoes cooling at a certain rate depending on the blower speed, print material and part size. Insufficient cooling causes contractions in the deposited material, which can lead to insufficient material solidification and layer adhesion [105]. Fig. 1 demonstrates three common print quality classifications: under-extrusion, good quality (optimal), and over-extrusion [109]. Under-extrusion can lead to defects such as voids

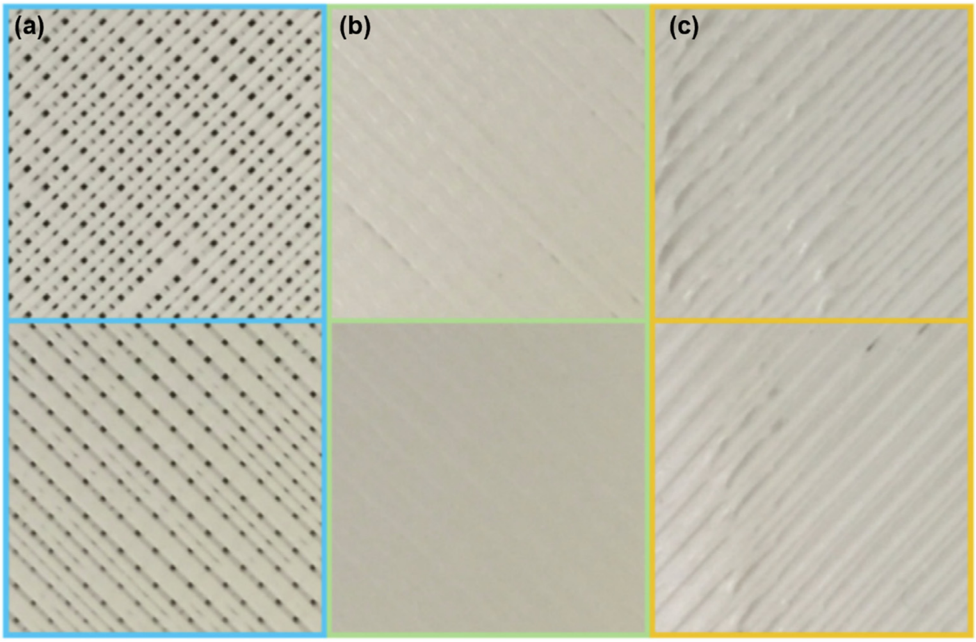

Fig. 1. Common print quality classifications in FFF (a) under-extrusion, (b) good quality, (c) and over-extrusion [109].

and delamination while over-extrusion can lead to mechanical stresses, residual strains, and warping [11,121].

Part orientation on the build plate is also a key parameter that must be considered. Parts that are printed "on the edge" have proven to show the best values of tensile strength, and hence, less possibility of defect formation [122]. A part's position on the build plate also affects the magnitude of developed residual strains and generated temperature gradients of the part during fabrication [111]. These are all factors that can affect real-time measurements (i.e., strain, temperature profiles) obtained using in-situ monitoring methods.

2.2. Defect formation in powder bed fusion

In PBF processes, close control over melt pool behavior is crucial to maintaining the surface quality and dimensional accuracy of manufactured parts [214–216]. An understanding of powder properties is also needed [113,217–219]. Experiments on powder flow measurements and powder delivery mechanisms in DED processes have helped in choosing optimum powder flow rates and spatial powder spread distances [66,75]. Within the melt pool, microstructural changes can occur due to melting and vaporization of the powders and substrate, powder motion and ejection, powder spatter, solidification of the powder or molten material, or changes in the vapor depression zone, which all may lead to defect formation [20,164–169,176–178]. Variables such as scanning patterns, overhang zones, and acute corners can lead to overheating and bad surface quality [130,220]. High temperatures, rapid heating and cooling, and large changes in temperature gradients can affect the energy density of the system, which can lead to defect initiation in the printed part [20,221,222]. Hence, defect formation is also directly correlated to temperature gradients within the system. This theory has been heavily supported by studies of laser welding and laser cladding processes (also see *DED* in Table 2 for laser cladding processes), which are similar in theory and procedure to LPBF processes [72,197,223–227].

Heating of metal powder in the melt pool can be characterized into conduction-mode melting and depression-mode melting, which is more commonly known as "keyhole-mode" melting [165,174,228]. Conduction-mode melting is driven by Marangoni convection, and occurs at melting point of the material when the energy deposited during the heating of a material exceeds heat conduction capacity. Keyhole-mode melting occurs when the temperature of the material reaches boiling point due to the intensity of energy density and vaporization. A high melt pool temperature makes powder particles melt faster when they are closer to a keyhole cavity, or depression zone, which leads to a decrease in surface tension near the defect. Keyhole-mode melting can form defects such as voids, weld lines (i.e., voids that form in gap-like or line-like shapes as a result of the separation and incomplete reconnection of areas of the melt pool due to keyhole mechanisms), or pores, for which they are known as keyhole porosities. Typically, conduction-mode melting occurs first, followed by keyhole-mode melting. The two melting modes have been modelled in literature – one study planted micro-tracers and traced their movement in the vicinity of the laser-powder bed interaction using high-resolution synchrotron X-ray imaging [178]. Overall, melt pool behavior can be attributed to five major driving forces: (1) Marangoni convection, (2) vapor plume, (3) vaporization induced recoil pressure, (4) hydraulic pressure, and (5) buoyancy [178]. This will be discussed more in *Section 3.2.3*.

In-situ and ex-situ NDT have been integrated in LPBF processes to better understand melt pool behavior. In different studies, researchers have used monitoring systems to track spatter ejection behavior and vapor depression due to overmelting, which has led to numerous conclusions about the melt pool [116,163,164,166,168,171,228]. Two kinds of spatter phenomena are characterized to occur in the melt pool: (1) droplet spatter, which is due to the convective transport of liquid or vaporized metal out of the melt pool, and (2) powder spatter, which is caused by non-metallic powder particles blowing away from the melt pool. Overall, the ejection behavior of the droplet column of the melt pool affects the protrusion of the melt track.

During the laser melting process, a vapor plume cloud is formed perpendicular to the vapor depression wall due to the natural direction of the laser beam on the powder bed. As demonstrated in Fig. 2, the metal vapor expands impacting the rear wall of the depression and leading to the formation of spatter ejection. Spatter ejection in turn limits formation quality and leads to microstructural changes in the part, which can negatively impact the part's mechanical properties, such as tensile strength and yield strength [168]. Under different melting conditions, spatter behavior can be explained by considering laser heated zones (LHZs) and the correlation between specimen and spatter positions on a build area. Compared to laser spot size, LHZs and surrounding areas affected by spatter ejection can be quite large, as demonstrated by the randomness in spatter ejection in Fig. 2. Hence, monitoring of surrounding areas of the LHZ is required in addition to the LHZ

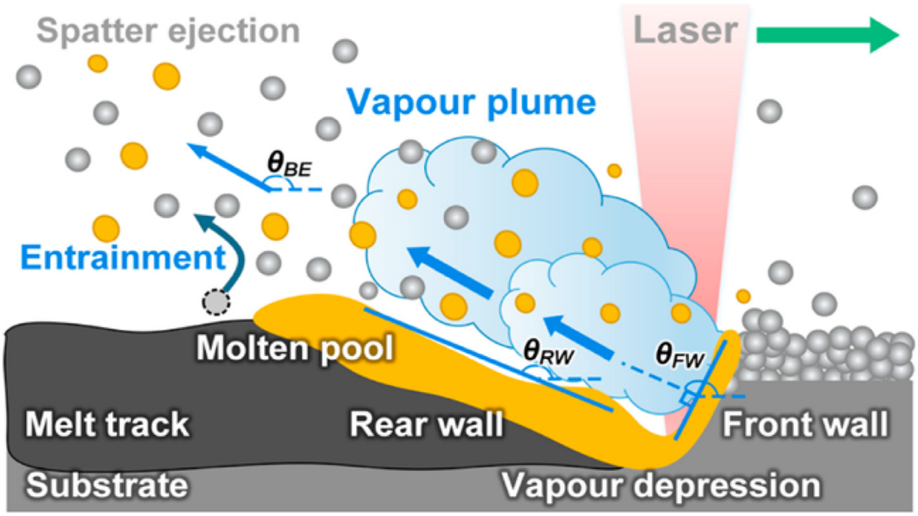

Fig. 2. Correlation between melting regime, tail depression, and spatter ejection [164].

itself. Furthermore, as seen in Fig. 2a, spatter behavior can be plotted and tracked using image-processing methods and statistical descriptors [116,166].

Overall, defect formation is heavily influenced by process parameters and melt pool characteristics. For example, high tensile residual stresses and fluctuations in energy density in the part are correlated to increasing scanning depth and scan rate [19,214,222,229,230]. Therefore, process parameter optimization and energy density control can limit microstructural changes that occur in manufactured parts, and hence, mitigate the formation of melt track defects [164–167,178]. One thorough review classifies three key defects in relation to process parameters [5]. As seen in Fig. 3, keyhole porosity appears in the high power and low velocity region of the graph, while LoF voids appears in the low power and high velocity region [5,230]. Balling appears in the region of high power and high velocity.

Process parameter adjustment and optimization provides an approach to mitigate defect formation. For instance, LoF voids can be mitigated by reducing scan line spacing and layer thickness. A second approach recommends increasing laser power or reducing laser velocity [5,230]. Keyhole porosities can be mitigated by reducing laser power. PBF may itself also act as a metallurgy method to improve the mechanical properties (i.e., ductility and ultimate tensile strength) of metallic materials due to the effects of process parameters [231]. Nevertheless, process parameter optimization may only be applicable, or necessary, at specific locations in a layer or particular instances during the print. Therefore, one of the main goals of in-situ monitoring is to determine the appropriate spatial and temporal locations for which real-time process parameter adjustments can mitigate defect formation.

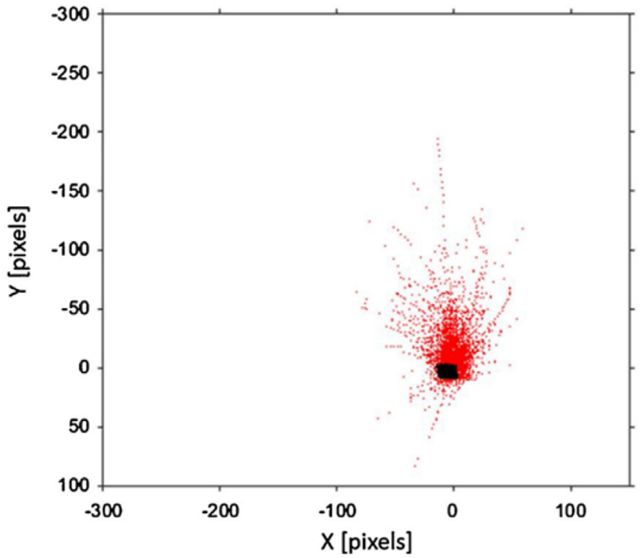

Fig. 2a. Spatter droplets (red) with respect to a LHZ (black) [166]. (For interpretation of the references to color in this figure legend, the reader is referred to the web version of this article.)

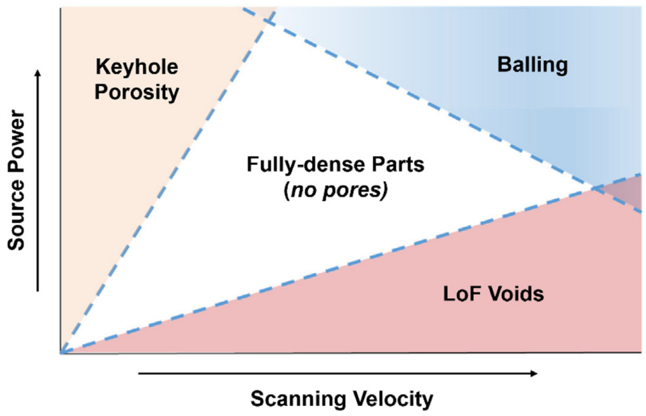

Fig. 3. Processing parameter influence on different types of defects in LPBF, adapted from [5].

3. In-situ monitoring for defect detection

As demonstrated in Table 2, imaging and acoustic methods have been extensively used for in-situ sub-surface and internal defect detection in PBF and FFF. These methods, as well as others used for surface defect detection, will be discussed in detail including capabilities, devices used, feasibilities, objectives, and results. Table 3 provides an outline of the devices used for in-situ monitoring of AM processes.

3.1. Data validation strategies

Data validation strategies are used for data correlation and overlaying, and provide a means to gain insight from the data collected using monitoring methods. Two common strategies have been used in literature and will be referenced in this review: (1) Post-Process Validation and (2) A-Priori Identification [18,181]. The former involves data acquisition through in-situ measurements followed by cross-comparison to data already gained from ex-situ techniques. The latter involves performing in-situ measurements, analyzing the data, and validating it by cross-comparison to data gained from ex-situ measurements of defects at the same locations. A-Priori Identification is favored due to the uniqueness of any individual CAD file and its correspondence to a specific

Table 3
Devices used for in-situ monitoring purposes.

In-situ Monitoring Method	Devices Used
Visual Imaging	Optical Cameras Charge-coupled device (CCD) Camera Complementary Metal Oxide Semiconductor (CMOS) Camera Photodiode High-frame Rate Camera Optical Spectrometer 3D Scanner/Projector
X-ray Imaging	X-ray Imaging System CT Scanner
Thermography; Temperature Measurement	Infra-red (IR) Camera Pyrometer Thermocouple Transducer
Spectroscopy	Near-infrared (NIR) Spectrometer Ultrasonic Spectrometer (US)
Interferometry	Inline Coherent Imaging (ICI) Device Mach-Zehnder Interferometer
Impedance Testing	*T*-junction Waveguide Piezoelectric Ceramics (i.e., lead zirconate titanate (PZT))
Acoustic Emissions	Piezoelectric Sensors (i.e., AE Sensors) ICP Microphone Fiber Bragg Grating (FBG) Sensor Doppler Vibrometer Transducer
Other Micro-sensing	Transmissive Sensor Optoelectronic Sensor

AM build. Cross-comparison of data becomes necessary to understand the accuracy of in-situ measurements. X-ray Computed Tomography (XCT) is an ex-situ technology that has proven to be a valuable tool for validation and evaluation of in-situ results. This will be discussed in more detail in *Section 4*.

3.2. Imaging methods

Imaging methods entail visual and thermal monitoring, using devices such as CMOS cameras, CCD cameras, IR imaging cameras, and X-ray imaging. They offer a non-contact method to measure thermal flow, thermal distortion, and changes in geometry of a 3D print by monitoring the printing process in defined space and time [96]. High-speed visible light communication (VLC) and IR thermal imaging can provide critical information such as surface melt pool dynamics, thermal signatures, and vapor plume appearance in the printed component. High-speed X-ray imaging can provide additional information about melt pool dynamics and vapor depression that cannot be seen by visible light and thermal imaging [20].

When multiple imaging methods are combined along with one or a series of mirrors, lenses, or fibers, they are referred to as an optical system. Optical systems are generally categorized into on-axis, off-axis, or coaxial systems. Early in-situ monitoring experiments provided the basis of device integration around the 3D printer, and attempted to define such systems [95,123–128]. These classifications have changed over the years with the development of new technologies and the integration of different sensors to the systems. On-axis systems use the optical path of the laser and scanner mirrors to emit onto the surface [128]. The laser beam is then focused on the build area for scanning using an f-theta objective lens. Laser and camera paths are usually directed through mirrors or beam splitters/expanders depending on the specific set up chosen. In off-axis systems, the optical path of the laser and the camera-based sensor are not on the same axis, as demonstrated in Fig. 4. Rather, the fixed camera is only limited to a finite area of the emitting surface.

Pictured in Fig. 5, a coaxial system uses multiple cameras or diodes with both direct optical paths and paths diverged by scanning mirrors, which makes it dependent on lens specifications. It can capture adequate surface area for observation [126]. Coaxial systems allow the sensors to accurately follow the position of the laser beam throughout the printing process [232]. With the integration of multiple sensors, they are also useful in providing a compromise between temporal resolution, spatial resolution, and cost of sensor. One study suggests a set of design criteria to determine the field of view (FOV) of imaging methods required in a coaxial system based on a theoretical approach [144].

Some disadvantages of coaxial systems are their poor brightness and inability to resolve pictures taken at high velocities and high resolutions. Improvements that have been made to overcome these challenges focus on creating external lighting for acquiring high-resolution data [18,19,25,125,126,233]. Lighting strategies have been studied to determine the optimal location and quantities of lighting sources in a monitoring system for defect detection [143]. The layouts of lighting sources were divided into categories such as bright and dark-field lighting, high- and low-angle lighting, and location with respect to camera position. It was determined that high-angle bright-field lighting located on the left side of the camera was optimal for illumination of the specimen being monitored in a PBF process and more susceptive to image segmentation [143].

3.2.1. Optical cameras

Optical cameras have been integrated in a variety of different systems to monitor melt pool behavior. Early studies used CCD cameras and pyrometers to monitor powder consolidation, part melting, overhang layers, and temperature distributions during a Selective Laser Melting (SLM) process [22–25,125,138,146,147]. A CMOS camera was used in a coaxial system to monitor and design a photodiode signal controller that tracked melt pool characteristics in a LPBF process and used them as signals [136]. The signal provided feedback to the system to control laser parameters using photoelectric signals [19,131,136]. Similarly, one study used two digital microscopes to monitor print quality (*see* Fig. 1) and a closed-loop quality control feedback system to adjust process parameters based on image texture analysis [121].

Other studies have combined optical cameras and photodiodes for melt pool analysis [129]. A photodiode can provide high temporal resolution with little cost [144]. Powder consolidation and powder bed issues have also been examined using optical cameras, and the melt pool has been monitored to understand melt pool characteristics [134]. Some studies have used optical cameras to collect data for training ML models [140–143].

CCD cameras have been used to monitor geometry profiles and surface defects in FFF [94,110]. Similarly, in a LPBF process, a complex optical system was built that utilized a 29-megapixel CCD camera, three independent light sources, and a series of attachments to collect typical process errors [137]. Images were captured at an angle with respect to the platform, and therefore, required a

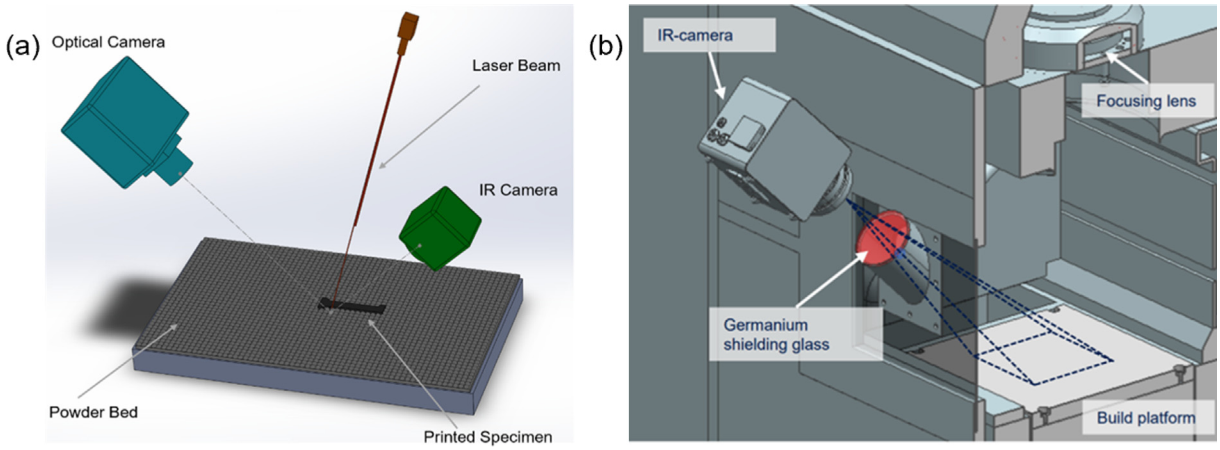

Fig. 4. Off-axis optical systems: (a) use of an optical camera and an IR camera for in-situ monitoring of a LPBF process printing a standard dog-bone specimen (b) use of a focusing lens and an IR camera at a 45° angle through Germanium shielding glass to monitor a PBF process on a build platform [150].

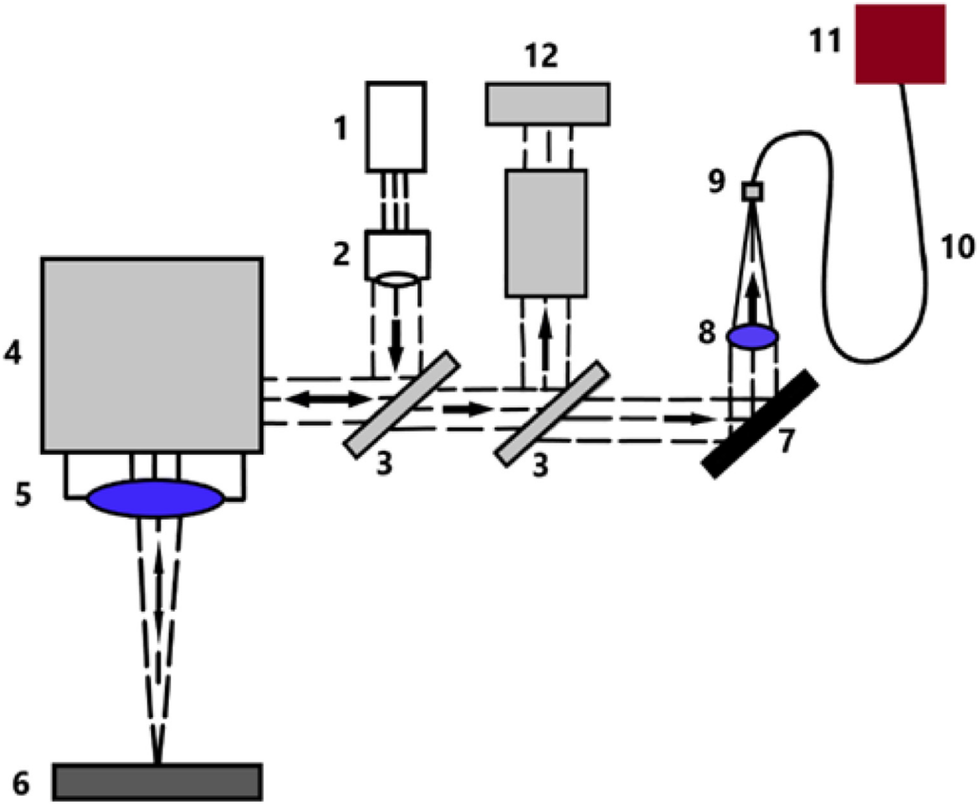

Fig. 5. Coaxial System with additional lighting. (1) fiber laser, (2) beam expander, (3) laser beam/thermal signal separating mirror, (4) scanner head, (5) F-theta lens, (6) powder bed, (7) mirror, (8) pyrometer lens, (9) fiber tip, (10) optical fiber, (11) pyrometer, and (12) CCD camera, adapted from [25,126].

correction from their perspective distortion using a tilt lens and a shift lens; this reduced the image resolution to ~ 24 µm/pixel, from 6576 × 4384 pixels to 4234 × 4234 pixels. An extension tube was used to reduce the minimum object distance of the lens. Irregularities of Inconel 625 were inspected and it was concluded that superelevations and poor support connections are the most critical errors that occur during the AM process [19,137]. This theory has since been refuted, as emphasized by research mentioned in *Sections 2 and 3*. Best quality surface images were collected when a light source was placed close to the build area and opposite to the camera.

In other work, an off-axis two-color pyrometer system consisting of two CMOS cameras (21 µm/pixel resolution) within the build chamber of a LPBF machine was used to monitor melt pool characteristics and detect surface defects with 120 µm resolution [160]. Pyrometry data collected was compared to pores identified using micro-computed tomography (µCT). Process irregularities were interpreted from deviations in melt pool temperatures and it was concluded that the detection of small features is hindered by sampling frequency [160]. Spatial locations for pores were predicted using outlier conditions and melt pool locations. The angle of the pyrometry camera was also found to affect minimum feature size identification – this has since been proven in research. By comparison with outlier melt pools using µCT, pores of 70 µm size could be identified. Optical cameras and pyrometers have also been used simultaneously for defect detection in a LPBF process [158,159,161].

Recently, a Basler optical camera was used in an in-situ monitoring system for defect detection in a nickel alloy fabricated by a LPBF process [181]. More details on this study will be introduced in *Section 3.2.4*. For the detection of overmelting, undermelting, and spatter ejection described in *Section 2.2*, one study used a high frame rate camera (36 µm/pixel resolution) for in-situ monitoring of a LPBF process printing Inconel 625 powder [116]. The high frame rate images, or video volumes, had an imaging window of 1024 × 256 pixels at high resolution, and were analyzed using statistical process control (SPC) charts. The SPC charts were used to identify violations in the data as indications of spatter initiation, pore formation, and anomalies [116].

Other studies utilized in-situ high-fidelity video recording, which offered both optical and thermal information, to track melt pool size, melting modes and melt pool behavior, such as spatter analysis, on the surface of the component [163–169]. High frame-rate or high-resolution optical cameras can also be combined with other devices. In one study, a high frame-rate optical camera was used along with a pyrometer for data collection and melt pool analysis of the sub-surface of a component built using stainless steel 316L powder [172]. The camera saved 256 × 256 pixels^2 video frames with a resolution of 14 µm/pixel. Sub-surface defects with a depth of ~ 200 µm were identified [161,172]. In another study, a high-resolution optical camera and a projector were used to accomplish fringe projection for surface topography measurements [173].

3.2.2. Thermography and temperature measurement

Thermography has been used extensively in PBF and FFF processes to monitor thermal activity during the print. Thermography is the analysis of spatial and temporal distribution of thermal parameters in objects [234]. It is typically performed by capturing infrared images or thermograms, which are thermal maps in which the distribution of the infrared thermal radiant energy emitted by the ROI is represented by a series of colors.

Thermographic devices convert emitted energy from ROI into images. Thermocouples and pyrometers are used to measure the temperatures of distinct objects. They can be categorized as thermography devices due to their use for analysis of temperature in objects [234]. Pyrometers have high temporal resolutions and are more sensitive to process deviations than other thermographic devices, such as IR cameras [201]. Thermocouples have been used to measure temperature distributions within the melt pool to determine melt pool stability and correlations between process parameters [156,157]. Other thermal detectors have been used to detect inferior part quality by measuring and evaluating properties such as thermal diffusivity, thermal conductivity, and energy density [146,150,151].

3.2.2.1. Infrared imaging. IR cameras are generally calibrated for blackbodies, which means they are heavily dependent on emissivity values. To provide accurate temperature and imaging information, IR cameras must be calibrated for the respective material being imaged and to the atmosphere of the print [20,96]. IR cameras have been used for various types of melt pool analysis in PBF processes [148,149,152–155,169]. They have been found to have better direction-dependent sensitivity compared to pyrometers and are better at detecting interlayer defects in printed specimens in-situ [201].

Accurate IR measurement requires sufficient information about the material's radiation heat flux. In general, the sum of the absorption, reflection, and transmission of radiative energy from a surface is equal to the total incident radiative flux. Radiosity is the sum of reflectivity and emissivity from a surface. IR cameras measure radiosity, which is then converted into images. The emissivity of a material, or surface, has a big effect on radiosity; therefore, data from IR cameras must be corrected to reflect the true emissivity of a material.

Two materials have been widely used in FFF processes in recent years: Polylactic Acid (PLA) and Acrylonitrile Butadiene Styrene (ABS). To determine the effect of ABS properties on monitoring capabilities, emissivity values of ABS washers in three different colors – red, white, and blue – were determined and used to correct IR data points from the IR camera [96]. Adjustments were made to account for room temperature changes. It was found that there was a strong correlation between temperature and emissivity of ABS. At higher temperatures, the emissivity of the ABS parts decreased for all colors, and white ABS had a lower emissivity than red or blue ABS as temperature increased. Following these measurements, an algorithm used the results from the white ABS polymer to correct the IR data points in-situ. As seen in Fig. 6, errors of up to 15 % were found in temperature measurements. This correlates to a difference of 36 °C between camera readout temperatures and actual temperatures. The procedure for emissivity correction can be repeated for other materials and build geometries to ensure feasibility. Different studies have utilized their own emissivity calibration techniques. A study on an Electron Beam Melting (EBM) process determined that post-processing analysis of IR intensity data can be sufficient for emissivity calibration, which can in turn be used for the approximation of thermal gradients along with other temperature-related properties [205].

IR cameras can be utilized to determine information about AM process parameters with the help of emissivity correction techniques. An early study utilized a FLIR Phoenix RDAS™ IR camera and pyrometer in an SLM process to find that the instrument can capture surface temperatures of the part with < 1 mm resolution [123]. Tangential speeds of particles travelling forward and backward along their trajectory were estimated. Another early study utilized an InfraTec Jade III mid-wave IR (MWIR) camera with an optical resolution of 320 × 240 pixels to determine the relationships between process parameters and melt pool characteristics in a Selective Laser Sintering (SLS) process [145]. Two experimental setups were made. The first setup had the IR camera in place of the x-y scanner head, almost perpendicular to the power bed. An optical resolution of 1.5 mm/pixel was achieved, and temperature distribution on the bed's surface was measured. The second setup had the IR camera adjacent to the scanner head at a 23° angle from the normal z-axis, enabling measurement of melt pool temperature at an optical resolution of 0.35 mm/pixel. Analysis revealed the dependence of mechanical properties on part orientation. IR cameras have also been used in several EBM experiments for melt pool and surface quality analysis, as well as process parameter analysis and modification [202–210].

Recent studies have utilized IR cameras for in-situ monitoring of AM processes for defect detection. A FLIR SC3000 IR camera with a spatial resolution of 320 × 240 pixels was used in an off-axis system to monitor the vapor plume that formed from the melting of

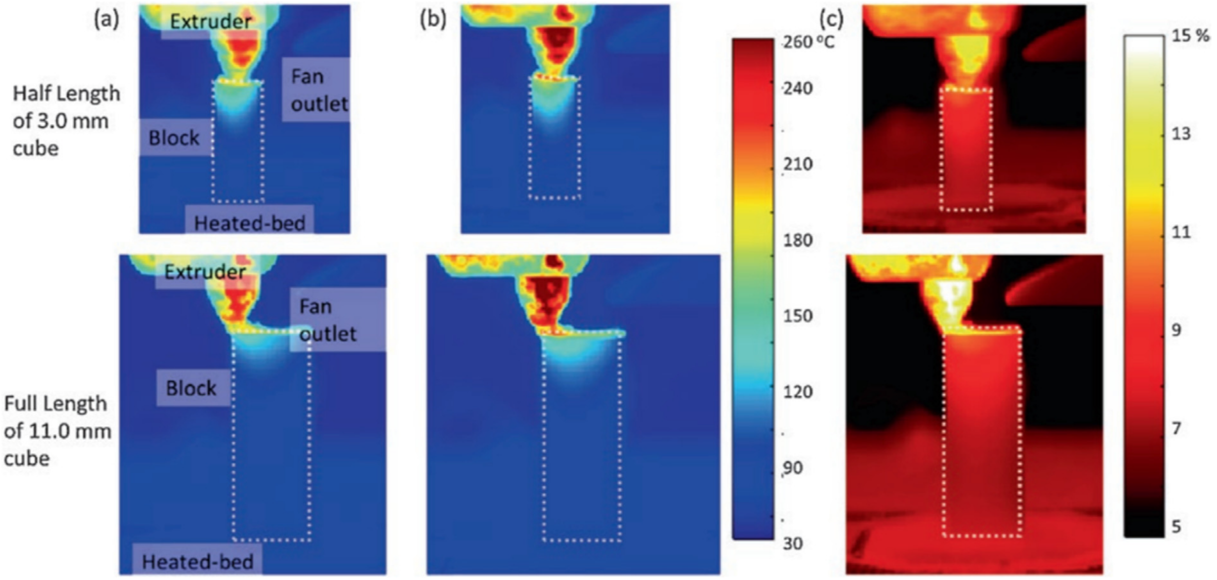

Fig. 6. IR camera images of three cubes printed with white ABS filament. Images captured the printing process in two instances: halfway (3 mm) and at completion (7 mm) of the printing process. (a) Camera readout, or uncorrected, temperatures; (b) corrected temperatures based on emissivity; (c) temperature difference between uncorrected and corrected temperatures showing errors present in the results [96].

zinc powder in an SLM process [155]. A multivariate control-charting scheme was used to monitor the ROI statistical descriptors chosen and compare them with stable operating conditions. The two statistical descriptors used were (1) the temperature of the ROI and (2) the average intensity of all the pixels belonging to the ROI. The in-situ monitoring process was successful in determining the stability of the AM process by detecting out-of-control conditions. A variation from stable conditions demonstrated process instability, which in turn indicated defect formation. Given that the monitored layers were non-consecutive, an instable condition can be signaled to the printer in advance, stopping the print thereafter.

Combined with other monitoring methods, IR cameras can be used for sub-surface defect detection. One study utilized a FLIR A65 IR Camera (640 × 512 pixel resolution) along with three acoustic sensors for sub-surface defect detection in a PBF process [162]. The combination of two monitoring methods allowed for the ease of linking AE signals to normal variations in process conditions. Sub-surface defect detection was performed ex-situ, where AE signals were compared to the cross sections of the printed part. Through this method, sub-surface defects were spotted at ~ 200–500 μm below the surface [162]. This method has the potential of in-situ monitoring and control of the printing process if it is combined with an ML algorithm capable of performing the required data fusion in real time.

Similarly, while experimenting with an EBM process, a combination of thermography, using a FLIR SC645 IR camera (640 × 480 pixel resolution), and input analysis through additional tools, allowed for sub-surface defect detection and real-time process control [211,212]. In the first study, IR images and layer information that were gathered using virtual instruments from LabVIEW software were used to determine the parameter modifications needed to improve part quality [211]. Parameter modification was based on the concept of microstructural gradients and grain-size differences in EBM-fabricated parts. For more details on grain size fundamentals, refer to [211]. ARCAM EBM control software along with the application of Microsoft Visual Basic 2010 allowed for automatic process parameter changes, and therefore, in-situ defect correction. The system focused on mapping of the coordinates of different elements within the user interface followed by mouse click simulation of the chosen elements. Layer information, such as the part's average temperature, was used to change parameters in-situ. However, mouse click simulation provided parameter modification with a slight time delay. This was due to two factors: (1) the use of two computing systems, which led to a ~ 10 s time delay for each modified parameter and (2) a three-layer delay for parameter modifications to take effect. If an application programming interface (API) is utilized with the ARCAM EBM control software (instead of Microsoft Visual Basic 2010) for direct communication, instantaneous parameter modifications would be possible. For the detection of instable conditions, IR images were first transformed from gray-scale images into binary images, and then image segmentation was performed by applying a threshold for specific pixel intensities [211]. If any temperature reading is outside of the user-defined temperature range, then a signal can be sent to the printer to stop the print. In a similar manner, porosity detection can be achieved by comparing porosity levels in the part to a user-defined acceptable range for porosity. In this experiment, spherical defects with sizes of 600–900 μm were embedded in the print and successfully detected using the mentioned procedure.

In the second study, in-situ monitoring and defect correction was attempted through the comparison of IR thermographs of the print to results obtained through CT scanning of the printed component [212]. The CT scanning technology used was capable of detecting defects as small as 40 μm. Porosities with a size of 100–2000 μm were embedded in the part as spheres, triangular prisms, cylinders, or cubes; some multilayered defects were made to appear within three to four layers of the print. IR thermographs of a pixel size of 264.6 μm were collected in-situ. During analysis, it was found that defects < 600 μm were not detected by the IR camera. This might have been due to quality and capabilities of the EBM printer or melting of subsequent layers affecting these small features [212]. Larger defects (>600 μm) and multilayer defects were visible in the IR thermographs, as well as CT scanning results. However, the measured geometry of the embedded defects between IR thermographs and CT scanning results differed by about 60 % in area. In-situ defect correction was conducted through both hot isostatic pressing (HIP) and re-melting of the affected areas.

3.2.3. X-ray imaging

X-ray imaging is an imaging method that has been used for in-situ monitoring and control of print quality by gathering information about sub-surface defects and other unique characteristics of the melt pool. An influential AM process system design is key to allow for real-time process monitoring of the build area using X-rays [235]. Note the distinction between X-ray imaging (radiography) for in-situ monitoring and XCT for ex-situ analysis: X-ray imaging is a method used to monitor the print in real-time while XCT is used for post-print analysis. Fig. 7 illustrates a typical X-ray imaging system used for in-situ monitoring.

High-speed and high-resolution X-ray imaging have been used to acquire critical information such as melt pool dynamics, melt pool variation, and vapor depression formation [20,73,75,174,177,178]. Information about melt pool dynamics and variations in melting modes can help mitigate defect formation in an additive manufactured part.

One advantage of X-ray imaging is its ability to identify the solid–liquid interface in the melt pool and observe changes in the depression zone, hence its use for melt pool analysis. In one study, X-ray imaging was used to monitor a LPBF process for melt pool analysis [177]. The high-speed high-energy X-ray imaging system used consisted of an undulator-generated pink beam with the harmonic energy at 24 keV, a detection system to capture the transmitted beam, a scintillator to convert the X-ray signal to visible light, and a high-speed camera (2 μm/pixel resolution) to capture the visible light [176,177]. The system captured X-ray images of the AlSi10Mg material in the melt pool. ImageJ was used to reduce noise and enhance contrast of the X-ray images, which made it possible to identify the solid–liquid interface of the melt pool in the images. It was found that laser power and scan speed had different effects on the formation of depressions in the printed component. When laser power and scan speed were increased simultaneously, all three melt pool dimensions increased – melt

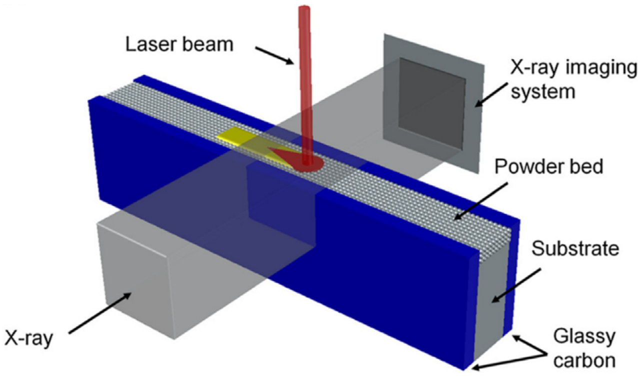

Fig. 7. X-ray imaging system for in-situ monitoring of a LPBF process [177].

pool volume increased by three orders of magnitude – and different melting modes were observed. Moreover, energy absorption of the system increased, which caused the variations in melt pool modes. As confirmed with other studies as well, laser power and laser scan speed have greater impacts on melt pool depth and width, respectively.

Further, flow micro-tracers were mixed with the feedstock powder for use in characterizing melt pool dynamics using an X-ray imaging system [178]. It was determined that as the micro-tracers' distance from the depression increased, their average and maximum speeds decreased. As demonstrated in Fig. 8, the tracer particles provided 3D melt pool dynamics which helped characterize the dominant driving forces in each melting mode. Vaporization was found to be the main driving force for fluid flow along depression-zone walls, while Marangoni effect was responsible for flow movement from high- to low-temperature region on the melt pool surface. The potential of in-situ X-ray imaging for defect characterization and detection is apparent with full-field mapping of melt flow. Phenomenon such as spatter ejection and vapor plume emission can be identified with X-ray imaging and defect mitigation is possible with an approach similar to that in [155] and other studies.

Other studies utilizing high-speed and high-resolution X-ray imaging to monitor the melt pool during laser melting of metal powders have obtained similar conclusions [73,174–176,179,180]. The main focus was characterizing keyhole-mode melting with great detail by considering the complex flow of the melt pool during the later stages of laser heating. The addition of diffraction techniques can give critical information about phase evolution and lattice contraction [175]. Using XCT for X-ray imaging has also proven to be a vital tool for the detection and evaluation of sub-surface defects. This will be discussed further in *Section 4.1* of this review.

3.2.4. Simultaneous use of imaging methods

Two or more imaging methods can be combined simultaneously for in-situ monitoring and control of an AM process. Combined with data overlaying techniques, they can create a 3D assessment of melt pool dynamics and temperature gradients to understand the events leading up to the formation of defects in the printed component. Currently, data overlaying and data fusion techniques are in early stages, and research into unified fusion theory is ongoing [13]. However, several studies have successfully demonstrated the capabilities of this approach.

In one study, simultaneous high-speed IR and X-ray imaging (Fig. 9) were used to track melt pool dynamics, vapor plume dynamics, solidification, and powder spatter and ejection, as well as detect sub-surface detects of Ti-6Al-4 V and pure tungsten in a LPBF process [20]. An IR camera (Telops Fast M3K) was placed at two different locations in the printer to capture thermal signatures: perpendicular and parallel to the laser scanning, to provide top and side views of the part, respectively. The spatial resolution of this IR camera is dependent on the frame rate: 3.1 and 90 kHz provide resolutions of 320 × 256 and 64 × 4 pixels, respectively [20]. The IR camera was calibrated using a modified version of the Stefan-Boltzmann equation to report data points that reflected the true emissivities of the plate and powder bed. The pixel size of the IR detector was 30 μm; each pixel was representative of a 30 × 30 μm area in average temperature. The X-ray imaging system was set up in the same manner as [177], but with a harmonic energy of 25 keV. Four different IR thermal filters were used, each calibrated with a specific temperature range. Experiments were conducted with a different combination of parameters: material, laser power, laser scan speed, IR thermal filter, IR orientation, IR frame rate, and powder use.

Simultaneous use of IR and X-ray imaging made it possible to study melt pool dynamics in 3D [20]. Vapor plume dynamics and

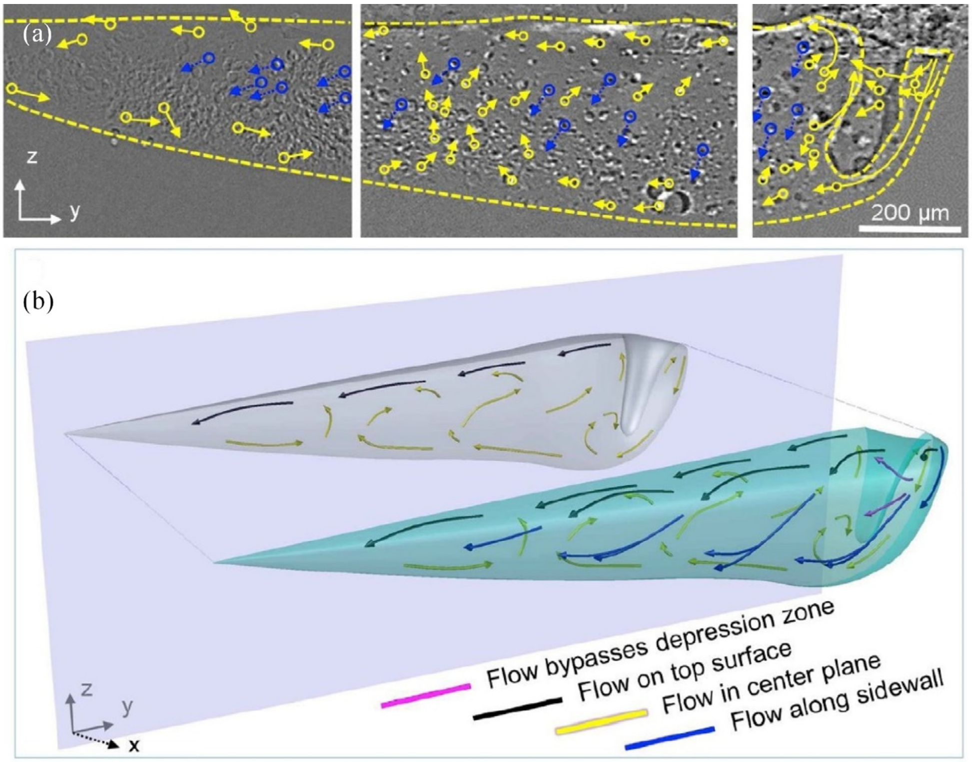

Fig. 8. Melt flow behavior under keyhole-mode melting. (a) X-ray images showing instantaneous liquid flow in the y-z projection plane, and (b) 3D reconstruction of the melt pool. (Refer to paper for more X-ray images of the melt pool in different projection planes) [178].

spatter ejection were visible at a low temperature range (273–524 K) in Ti-6Al-4 V using IR imaging as shown in Fig. 10. These behaviors were invisible in X-ray imaging due to the high density. When porosities were intentionally formed in the printed component due to increased laser power (364 W) and scanning speed (0.4 m/s), they were tracked at a temperature range of 537–1567 K with the assistance of X-ray imaging [20]. It was also found that as IR frame rate increases, a more continuous cooling transition to the solid phase takes place, which demonstrates a more accurate thermal profile. Lastly, vapor depression, or a sub-surface defect, with a size of ~ 200 μm and a depth of ~ 150 μm was present in IR and X-ray images. Scanning with no powder present also revealed key thermal features through the IR camera [20].

The synchronization of IR and X-ray images allowed for the identification of thermal signatures that appeared due to the formation of surface and sub-surface defects, as well as the observation of surface and sub-surface phenomena that led to the formation of defects such as keyhole porosities [20]. This technology has the potential for defect correction if data can be synchronized in real-time and feed back to the system for parameter optimization. In another study, a monitoring process utilizing a FLIR SC7600 IR camera and a Basler optical camera was created to detect spatial and temporal distributions of sub-surface and internal defects in CM247-LC nickel-based superalloys [181]. A Pythagorean geometry was manufactured using a LPBF Renishaw AM-250 system. The optical camera was used to take pictures of every layer before and after powder spreading. IR data was only collected for strategic layers where large changes in the geometry occurred. The IR camera, with a spatial resolution of 640 × 512 pixels and a length of 100 μm/pixel, was calibrated based on peak intensity, rate of decay, and the number of gyrations. Sixteen cubes of 15 × 15 × 15 mm^3 were made, each with a different combination of process parameters. Laser power was the only parameter kept constant at 200 W.

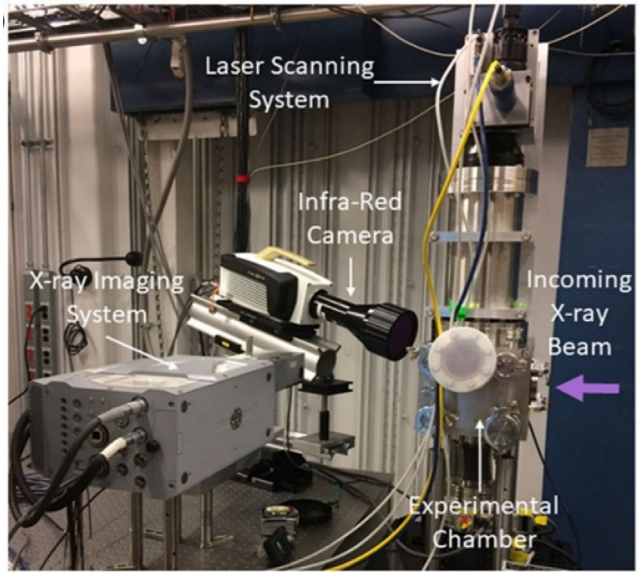

Fig. 9. Monitoring of an SLM process using simultaneous IR and X-ray imaging [20].

Optical images from the Basler camera provided the spatial location of defects. The distribution of surface porosities and cracks were found to be spatially variant in different length scales across the geometries. The top 25 % of build height was found to be more vulnerable to defect formation. Furthermore, variations of IR thermal signatures were found to show defect formation tendency as shown in Fig. 11c-j.

Sub-surface defects of 50–1000 μm were visible using in-situ monitoring methods [181]. Internal defects could be identified through a combination of in-situ optical and IR imaging and ex-situ analysis using XCT [181]. Fig. 11a and 11b show a processed in-situ optical image and an XCT image with corresponding defects at similar locations. Validation of in-situ feature extraction with ex-situ data was possible at a depth of 30–50 μm from the surface. (See *Section 4.1* for more details about the use of XCT in this study). However, the optical camera illuminated inconsistent lighting patterns, asserting the need for additional processing of optical images. The in-situ process also had a tendency of showing false positives in the data as some areas in a layer may have been remelted due to high laser intensities. It was found that local preheating due to laser scan lengths can cause a difference in results

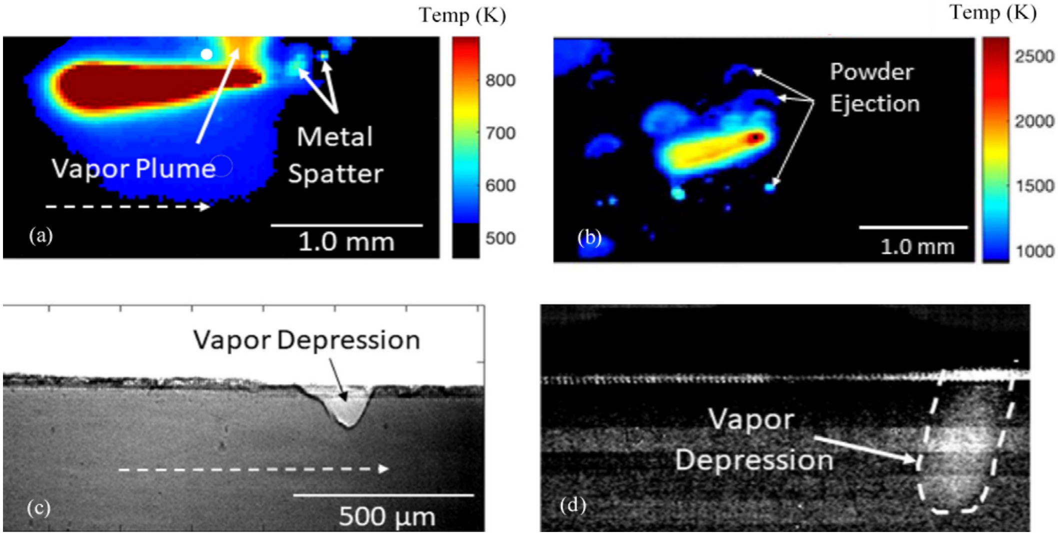

Fig. 10. (a) IR imaging of Ti-6Al-4 V showing vapor plume, metal spatter, and vapor depression (or keyhole porosity) with a filter allowing a temperature range of 273–524 K with no powder used, (b) IR imaging of Ti-6-Al-4 V mid-scan showing powder ejection with a filter allowing 537–1567 K and laser power of 364 W, (c) X-ray imaging of Ti-6Al-4 V with a filter allowing 273–524 K showing vapor depression, but not vapor plume, and (d) X-ray imaging of pure Tungsten showing vapor depression with a filter allowing 828–2773 K and laser power of 520 W, adapted from [20].

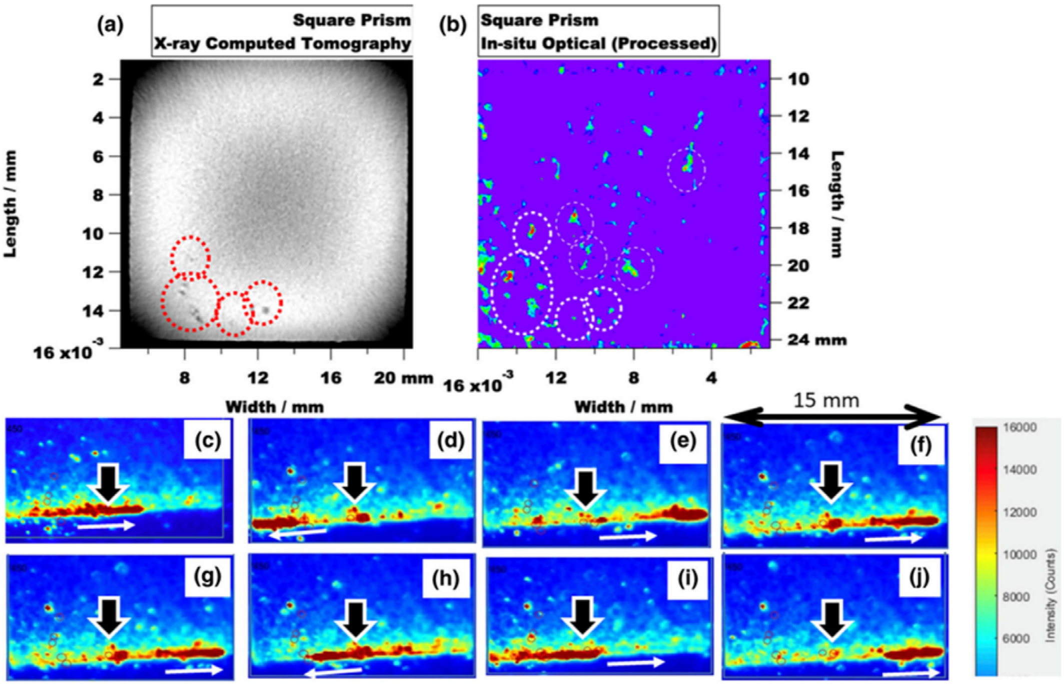

Fig. 11. (a) XCT data of a printed layer in a CM247-LC nickel-based alloy showing internal defects (b) processed in-situ optical image of the same layer showing sub-surface and internal defects at multiple locations (c-j) IR data from the same layer highlighting the formation of permanent defects (highlighted by the black arrows) after the passing of a laser beam [181].

and can produce several inaccurate representations of defect formations [181]. These aspects must be taken into account to obtain accurate results.

In a similar monitoring process, in-situ defect detection was performed using a mid-wave IR (MWIR) camera (100 μm/pixel) and a CMOS camera (50 μm/pixel) to study the effects of thermal distortions on the integrity of the print [182]. Results were verified by ex-situ inspection using μCT. Both cameras were placed on the top of the machine outside of the build chamber; a beam splitter was used to allow for both cameras to observe the same area of the build plate. The specimen, printed using stainless steel powder, consisted of two adjacent 5 mm^3 cubes on top of a 10 × 10 × 5 mm^3 base. Layer thickness was 50 μm. The MWIR camera recorded thermal videos of the print with a frame rate of 900 Hz and a spectral range of 2–5.7 μm. The CT scanner was capable of detecting defects of > 14 μm. Data overlaying of optical, IR, and μCT data was accomplished through elastix 4.9, an image registration software [182]. Determination of actual temperature values was not feasible due to limited camera spatial resolution and the non-linear relationship between intensity and temperature. However, areas with defects correlated to increases in optical and thermal signatures compared to the average signature values. Additionally, an artificial defect planted in layers 61–74 of the base was visible in both optical and IR images [182]. This defect was identified in images of layer 75 of the print, but not in layer 77, implying that the monitoring process was capable of only sub-surface defect detection with 50 μm layer thickness. An IR camera and CT scanning have also been used in another study to detect and correct sub-surface defects during processing [212]. In-situ defect correction was achieved by remelting of depressed areas. The success of each imaging method in defect area measurement varied: CT scanning yielded ~ 60 % smaller defect sizes than IR imaging, which detected defects > 600 μm in size [212].

Another experiment on a LPBF process that used high-speed pyrometry and optical imaging to monitor the melt pool drew similar conclusions [161]. Thermal emissions were collected from the entire melt pool with a 200 μm-core multimode fiber that transports light to the pyrometer. A high-speed machine vision camera captured 256 × 256 $pixels^2$ images with a spatial resolution of 17 μm/pixel. The amplitude of signals was used to identify conduction and keyhole mode transition zones. A relationship between increasing laser powers, decreasing velocities, and increasing signatures was obtained. Pyrometer signals were correlated to pore formation using ex-situ X-ray radiography to create a probability correlation for defect formation [161]. This comparison can provide a standard for pore creation probabilities in a printed part, allowing for some predictability of defect formation.

Table 4 summarizes research studies in which sub-surface defect detection was achieved using in-situ monitoring. These details include critical information such as defect size and defect depth from the uppermost surface of the printed component, as well as information pertaining to the devices used for monitoring and programming used for data analysis.

3.3. Acoustic methods

Acoustic methods include acoustic emissions (AE) sensing, ultrasonic measurement through deliberate excitation, and inline coherent imaging (ICI). AE sensing relies on piezoelectric acoustic sensors that convert the energy from stress waves, or acoustic signals, into electrical signals, which are then measured [8]. ICI is a low-coherent interferometric imaging technique that uses acoustic interferometers to measure physical characteristics of sound waves, hence its classification as an acoustic method [198–200]. Due to the low cost of sensing technologies, acoustic methods can be implemented in a variety of manufacturing environments.

Acoustic signals are measurable in AM and can be studied to understand the complex dynamics of AM processes [187,188]. By processing the raw AE signals, one can acquire data corresponding to internal defect formation in a printed part [190,236]. Signal processing methods are capable of providing a source for feature extraction and information mining from the acquired signals.

Table 4
Results and details of sub-surface defect detection using in-situ monitoring methods.

AM Process	Devices Used	Pixel Length (μm/pixel)	Resolution (pixels)	ML/Programming	Depth of Defects (μm)	Defect Size (μm)	Reference
LPBF	High-frame rate optical camera	14	256 × 256	CNN, SeDANN, RNN, SVM, KNN	∼ 200	∼ 80–400	[172]
	Pyrometer	–	–				
LPBF	IR Camera	–	640 × 512	–	200–500	200–500	[162]
	Acoustic sensors	–	–				
EBM	IR Camera	–	640 × 480	ARCAM EBM Software; Microsoft Visual Basic 2010	70	600–900	[211]
EBM	IR Camera	264.6	640 × 480	–	3-4X layer height	> 600	[212]
LPBF	IR Camera	100	–	elastix 4.9; Amira ZIB Edition 2019	∼ 100	∼ 400	[182]
	CMOS Camera	50	–				
LPBF	IR Camera	30	320 × 256	–	∼ 150	∼ 200	[20]
	X-ray Imaging	2	–				
LPBF	IR Camera	100	640 × 512	Python, ImageJ, IgorPro, MATLAB	∼ 50	50–1000	[181]
	Basler Optical Camera	–	–				

Types of signal processing methods include time or frequency domain methods, neural networks, waveform-based methods, clustering, and probability distribution methods [8,9,98,117,183,237]. The application, advantages and disadvantages of several of these signal processing methods as they relate to in-situ monitoring in AM will be discussed in detail in *Section 3.3.2*.

3.3.1. AE equipment and sensing technologies

In AM, acoustic signals can generate due to internal structural changes, such as residual stresses, defect formation or crack propagation, or external factors, such as movement of the printer or its components, electromagnetic interference, turbulent flow of fluids, frictional noise, impact, or other conditions that create background noise [8,183,185]. An AE-based monitoring system is capable of detecting these signals that travel as a result of the printing process [8,91]. The working principle of an AE sensing system with a piezoelectric acoustic sensor is demonstrated in Fig. 12. Raw AE signals, or transient electric waves, are collected by the sensor and then transported through a series of external devices: a low-noise preamplifier, a data filtering device, an amplifier, a signal processing unit and finally, a data storage unit. Acoustic sensors have excellent location- and direction-dependent sensitivities, which makes them highly sensitive to process deviations [201].

Raw AE signals are typically gathered in bulk datasets, and therefore, are hard to distinguish between [98,184]. To ensure proper acquisition of AE signals, acoustic sensors can depend on a certain sensitivity or frequency range to operate. According to the Nyquist-Shannon sampling theorem, a continuous signal can be properly sampled only if it does not contain frequency components higher than one half of the sampling rate [238]. This is essential to determine the correct sampling rate for signal acquisition in order to perfectly transform the continuous signal to discrete values. In addition to a sampling rate, a threshold limit can be appropriately chosen and logged to the sensors. The threshold limit is particularly helpful in qualitatively representing process malfunctions when the background noise level is either constant or changing gradually [98,170]. Fig. 13 shows the potential errors associated to thresholding, where a low threshold limit can result in premature triggering by the background noise and a high limit can result in missing the actual signal offset [170]. For more information on image thresholding techniques and algorithms, refer to [239].

By integrating segmentation techniques to the signal acquisition device, only the desired AE signals are gathered, which prevents the overflow of storage with unnecessary data. The AE data that is collected can then be correlated to surface, sub-surface, and internal defects that have formed in the printed component. Thus, AE has been implemented in AM processes for in-situ monitoring [240,241].

Piezoelectric transducers are the most commonly used AE sensors [8]. Piezoelectric AE transducers work based on the piezoelectric effect and the sensitivity and allowable frequency range of these transducers can be limited such that not all noise is detected by the device [117].

In addition to piezoelectric sensors, other types of sensors that have been used for AE are airborne and pre-polarized ICP microphones, Fiber Bragg Grating (FBG) sensors, and heat-resistant

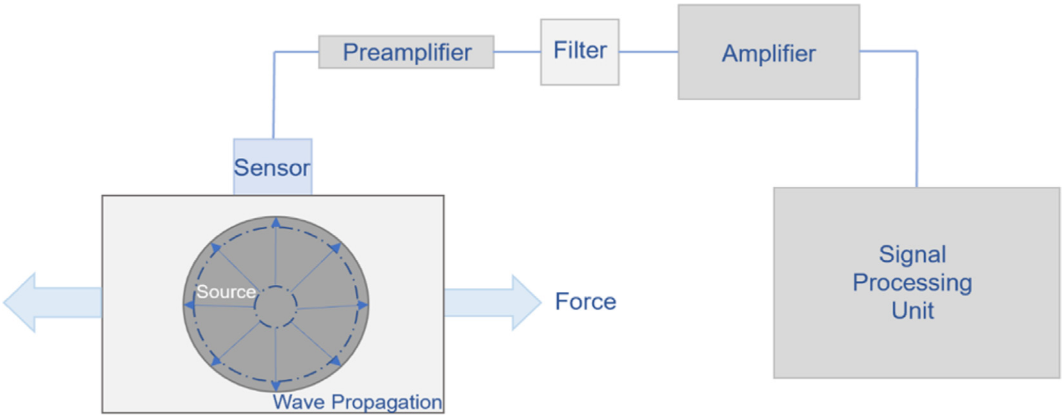

Fig. 12. Acoustic Emission sensing through the generation and capture of signals using piezoelectric acoustic sensors, adapted from [8].

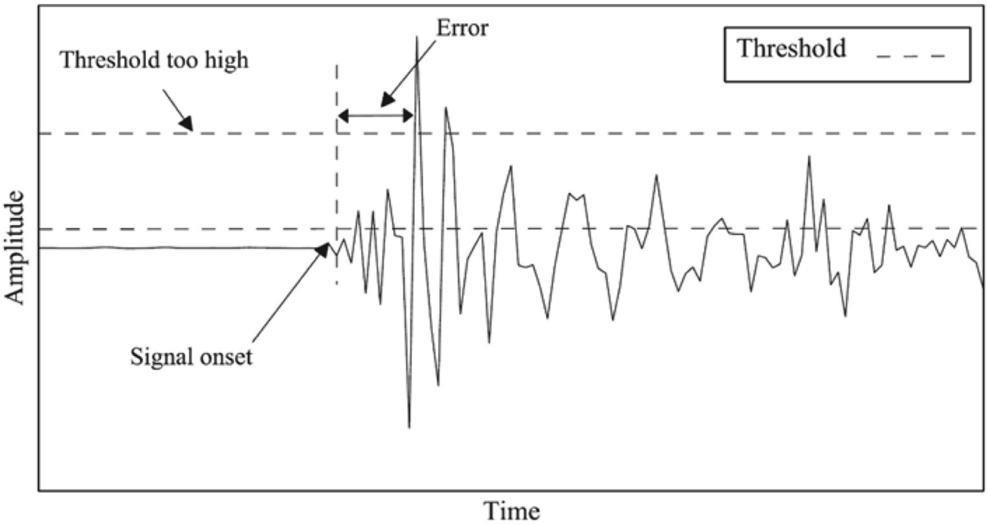

Fig. 13. Potential errors in detecting the onset time of AE signals using threshold limit [170].

transducers [8,101,102,104,106,189,190,191,195,198]. Although an FBG sensor is constructed inside the core of an optical fiber, it is considered an acoustic device due to its use for the collection of acoustic emissions and vibrations during real-time process monitoring: the stress waves created during the AM process result in the extension and compression of the FBG structure. FBG sensors have high sensitivity, fast response, signal integrity, and insensitivity to radio frequency interference [111]. However, they are thermal sensitive and cannot distinguish between the effects of temperature and strain on wavelength shifts [111].

In one study, an FBG sensor was mounted on a Concept M2 machine (Fig. 14) to detect airborne acoustic signals with high sensitivity [189]. Process parameters were intentionally altered to form pores in the printed specimens. Signal processing methods were used to classify the features of the manufactured parts by grouping the energies of frequency bands. Parts were classified as low, medium, and high quality depending on the concentrations of pores in the parts. In another study, FBG sensors were used in conjunction with thermocouples to determine residual strains of printed parts in-situ [111]. Temperature values of the extruded material needed to remain below or close to its glass transition temperature. It was found that strain profiles are variable and spatial-dependent throughout the printing process [111].

3.3.2. Signal processing methods

Signal processing methods are required to analyze the signals recorded during in-situ monitoring of the AM process. Acoustic signals that are correlated to defect formation can result from internal structural changes such as deformation, crack initiation, crack propagation or growth, phase transformations in the microstructure, pore formation, or delamination [98,117,183,185,189]. These signals can be filtered, grouped, and analyzed for features to be presented as patterns of defect formation. Feature reduction techniques can be used to decrease computation complexity [196].

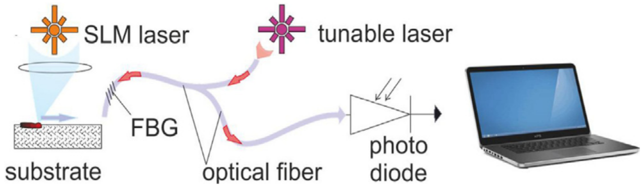

Fig. 14. FBG sensor setup for acoustic emission testing [189].

Features that affect source localization are ones derived from AE signal onset time (marked in Fig. 13): duration, number of counts, rise time, and counts to peak [98]. Other significant AE features that can be recognized by signal processing methods are amplitude, energy density, duration, peak amplitude frequency, probability distribution, and Kurtosis. While the majority of signal processing methods can be applied to both digital image signals and acoustic signals, this review will mainly cover their use for acoustic signal analysis.

Examples of AE signal processing methods include time domain analysis, frequency domain analysis, time–frequency domain analysis, convolutional neural networks (CNN), K-means clustering, support-vector machine (SVM), and continuous wavelet transform (CWT) or wavelet packet transform (WPT) [8,9,84,90,98,101,159,183,185,189]. Using these signal processing methods, signal characteristics (i.e., features) can be extracted and used to derive information about defect formation. For example, some defects can produce waveforms that can be both similar and different in shape, which can be differentiated using CWT or WPT [9]. Likewise, certain frequency values correspond to certain defect mechanisms (i.e., balling, lack-of-fusion), which can be shown using frequency-domain techniques [82,117]. Fig. 15 displays the range of frequency levels for different types of defects.

In general, it is more beneficial to find a signal with various AE events as to increase the efficiency of the AE testing process. This can be accomplished by using signal processing methods for temporal domain analysis. For example, one study was able to track times of occurrence and locations of AE events by conducting single-layer modeling tests with data collected using piezoelectric AE sensors and a wireless sensor node [186]. AE events corresponding to pores and microcracks that formed in the specimen were detected with an error of a few millimeters [186]. By analyzing the signals in each layer, it was possible to identify all the defects in every layer of the printed component. Fig. 16 shows the typical steps for defect detection using in-situ monitoring and signal processing for feature extraction.

3.3.2.1. Neural Network methods.

Artificial neural networks (ANN) are powerful tools in ML used for predictive modeling, data classification, data clustering, and adaptive control, along with many more statistical techniques [242,243]. For example, in one study,

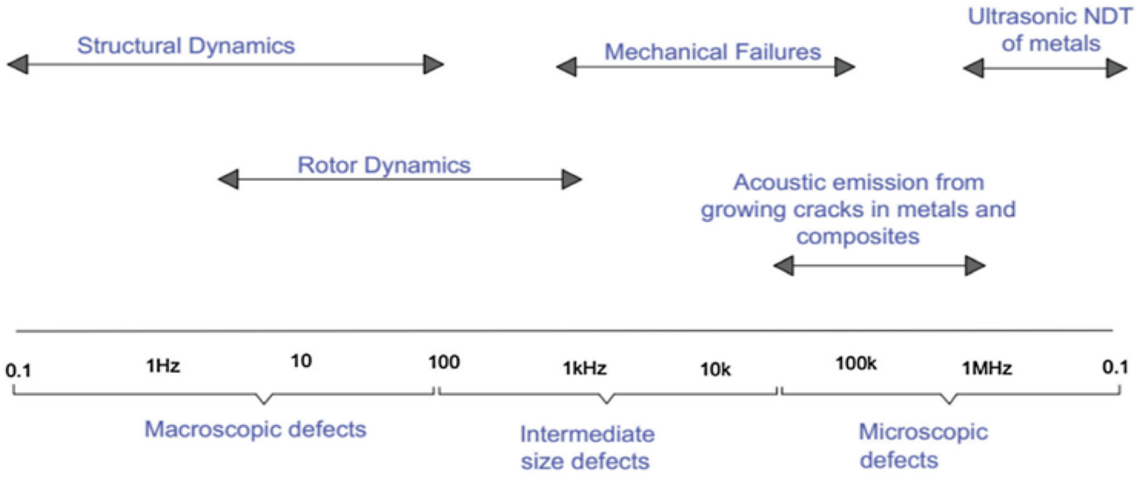

Fig. 15. AE frequency levels/ranges for different types of defects [8].

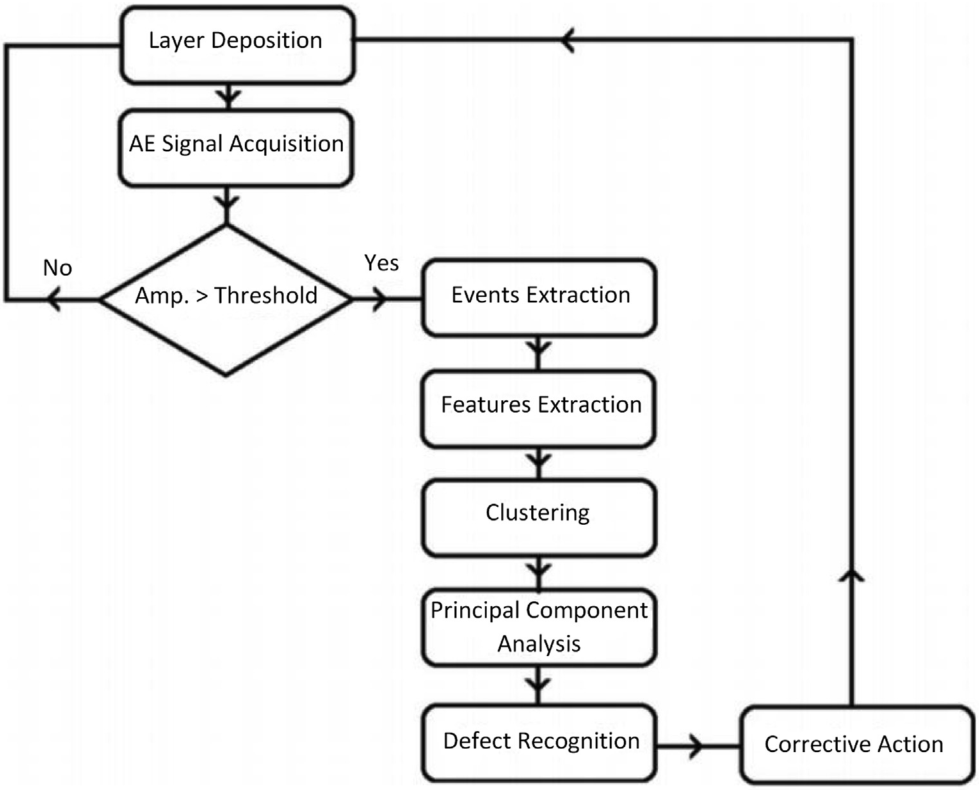

Fig. 16. Typical steps in AE analysis [90].

a deep ANN was used for classification of melt pool images captured using a high-speed camera [242]. Seven specimens were created and images of the melt pool were captured from layers 50 through 99. The purpose of the ANN was to classify the images based on laser power. The ANN was trained by varying the number of hidden layers and nodes. Classification failure rates of laser conditions were determined. In another study, an ANN was used to classify signals recorded using an acoustic sensor and to detect pores in parts manufactured using SLM [184]. Large datasets were difficult to manage; however, it was concluded that acoustic signals are suitable to characterize the SLM process.

Several subcategories of ANNs exist that serve different purposes and require sets of data with varying sizes. One common subcategory of ANNs in this field is Convolutional Neural Networks (CNN), which are used specifically for image processing. CNNs can capture spatial and temporal dependencies of an image, as well as provide successive projection of the data into higher dimensionality spaces [143,243]. In one study, a CNN was utilized to detect defects by processing geometrical anomalies to extract features from an FFF process [243]. A digital single-lens reflex (DSLR) camera was mounted at the top of a printer and directed down towards the build plate. Images were captured at regular intervals, resized, and analyzed in real-time using the CNN. This model has the potential to detect defects then pause the printing process.

Another study proposed a multi-defect threshold segmentation algorithm and several CNNs for defect extraction and classification, respectively [143]. The segmentation algorithm was used to extract features from images captured of four types of powder beds with embedded defects. Different lighting strategies were used as discussed in *Section 3.2*. Three common CNNs were used for defect classification: AlexNet, Visual Geometry Group (VGG)-16, and Residual Network (ResNet)-50. AlexNet was determined to be the most effective due to its low algorithm-processing speed and high classification accuracy [143]. In a similar study, VGG-16 and ResNet-18, a different variant of a residual network corresponding to 18 layers, were used to study the implementation of transfer learning to the two CNNs for reducing training time when monitoring different materials for the same defect formation mechanisms [244]. The four mechanisms studied were balling, LoF voids, keyhole pores, and conduction-mode melting. Spectrogram images corresponding to the four mechanisms were computed using wavelet transforms. ResNet-18 outperformed VGG-16 during classifications of build quality for two different modes of transfer learning. Monitoring for defect detection of two different materials using AE sensing and signal processing methods can be simplified and optimized using transfer learning.

In a study of a laser welding process, three different CNN algorithms were used to classify conduction welding, stable keyhole and unstable keyhole melting conditions [227]. In practice of Post-process Validation, these conditions were first identified through X-ray radiographic imaging, where mechanisms of keyhole formation are found to be analogous to those in metal AM processes such as LPBF: a balance of recoil pressure and surface tension is required for stable keyhole formation [227]. AE signals were collected using an acoustic sensor attached to the samples, i.e., rectangular plates of an aluminum alloy. AE signatures were classified with accuracies of 85–99 % with one of the three CNN algorithms used. It was also possible to distinguish between the formation and removal of pores [227].

In recent research, two semi-supervised CNNs based on Variational Autoencoder (VAE) and General Adversarial Network (GAN) were used for anomaly detection for a LPBF process [193]. Semi-supervised models are useful when it is difficult to have a balanced dataset between investigated regimes or when only one class, out of all identified classes, is of interest [193]. In this study, acoustic signals of defects such as balling, LoF voids, and keyhole pores were collected using a microphone, and the two CNNs were trained for defect detection. The VAE- and GAN-based CNNs were capable of distinguishing between defects with 96 and 97 % accuracy, respectively. Note that these two models cannot be generalized, as they are dependent on factors such as powder size distributions and process parameters. For more information on VAE and GAN, see [193].

A Spectral Convolutional Neural Network (SCNN) provides a few advantages to the typical CNN [9,189,190]. It is a feature extraction tool that is able to process data from more complex structures compared to a CNN while using less computational power. This is done by using irregular convolutional operations to extract features. When complex data is input into the system, this feature extraction tool can be used to guide the network during the training procedure, optimizing its structure. A disadvantage of SCNNs is that categorization is not as accurate [189,190]. For example, sample quality can often be misclassified when an attempt is made to categorize. Another disadvantage is the algorithm's dependence on the signal acquisition window, or window span. Temporal resolution, stability, spatial resolution, and sensitivity to noise are all factors that rely on window span; for example, increasing window span can decrease sensitivity to noise, but only at the expense of temporal resolution [9].

In a study aimed at collecting AE signals off a Concept M2 machine using a FBG sensor, the goal was to locate concentrations of pores that had formed in the component manufactured using Cl20ES stainless steel powder [189,190]. Process parameters were altered to create three build components of different qualities and porosity content: 0.07, 0.30 and 1.42 % porosity for low, medium, and high quality, respectively. To overcome the disadvantages of SCNNs, signals were collected in two running windows: a short running window (SRW) and a long running window (LRW) [189,190]. This allowed the SCNN to analyze data from both windows simultaneously. Graphical representations were created for both a SRW and LRW, which were measured in milliseconds (ms). The simultaneous use of two running windows allowed stable analysis of the presence of noise. As displayed in Fig. 17, this also helped obtain optimal window sizes: 80 and 160 ms for SRW and LRW, respectively.

Using the SCNN and wavelet decomposition, porosity – or internal defects – was detected with an accuracy of 83–89 % [190]. Overall feature representation accuracy was in the range of 78–91 %. Highest classification accuracy was achieved for the part with medium quality (refer to [190] for details on process parameters). Additionally, the ML algorithm was able to identify if a pore had disappeared, or been removed, as a result of subsequent laser scanning. With the designation of running time windows, the SLM process was categorized into a set of events with unique raw AE signals. This helped in detecting the stable-unstable transitions that occur in an AM process due to the constant changes in process parameters. In a continuation of this study, reinforcement learning (RL), a subset of ML, was used to classify the quality of the three build components [245]. Classification of the quality was accomplished with an accuracy of 74–82 %, slightly less than that categorized using SCNN. Overall, the ultimate goals are to use the SCNN to predict forthcoming defect formation in the build component, as well as use the AE in-situ monitoring technique to create a closed-loop AM process and prevent defect formation.

One study used another form of ANNs, a Sequential Decision Analysis Neural Network (SeDANN), to analyze data obtained through optical imaging and thermography monitoring and to predict single-track quality by fusing sensing modalities [172]. A high-speed 256 × 256 pixels^2 video camera with a spatial resolution of 14 μm/pixel and an infrared pyrometer with a sampling rate of 100 kHz were used for in-process sensing. SeDANN was found to out-perform many other ML approaches due to its adaptation of physic-based process features to correlate process signatures with quality metrics [172]. Compared to the CNN used in that work, SeDANN predicted the standard deviation of single tracks with

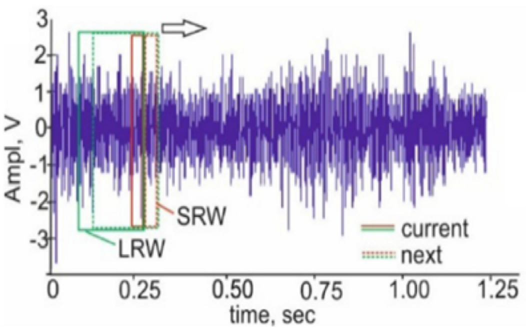

Fig. 17. A typical raw AE signal with optimal window sizes of 80 ms (SRW) and 160 ms (LRW) [190].

40 % better prediction fidelity (R^2) in one-tenth of the computation time [172].

In other work, a Deep Belief Network (DBN) was used to classify acoustic signals of five defect patterns that occur in a SLM process [192]. A DBN is a probabilistic graphic model, where every layer is subsequently built on patterns of data captured from successive layers to achieve dimension reduction, pattern analysis, and classification [192]. Repeated layer-by-layer unsupervised training of the DBN and supervised fine-tuning allows it to become more efficient for classification. In the study, AE signals were collected using a pre-polarized PCB microphone with a frequency range of 0 to 100 kHz [192]. Signals were preprocessed in three different ways: by the original, the FFT of the signal, and the FFT with denoising. Average classification rates were found to be 72.43, 95.93, and 95.87 %, for the original data, data after FFT, and data after FFT and denoising, respectively [192]. Therefore, the DBN model performs better without data preprocessing. Results were compared with other signal processing methods such as SVM, where average classification rates were found to be 67.82, 97.86, and 98.01 %, respectively. Overall, the DBN model performed better than SVM without data preprocessing, while SVM performed slightly better with data preprocessing. The DBN is capable of learning deep features of the data due to its training patterns, however, while SVM is not capable of identifying relationships from the data.

Another example of an ANN that has been used in sequence with monitoring methods for defect detection is a Recurrent Neural Network (RNN). An RNN is used to recognize sequential characteristics of a dataset. It has been used to predict the orientations of fibers in a µCT scan image of a 3D printed glass fiber reinforced polymer composite [103]. By storing previously acquired data, an RNN is capable of comparing all data in the dataset to recognize different patterns. However, the deviation of RNNs is relatively greater than those of CNNs. Other ANNs have also been used for ex-situ analysis, as discussed in more detail in *Section 4.1* [246].

3.3.2.2. Time domain and frequency domain. Time domain methods are used to analyze transient signals, or signals with data that varies in time [117]. Frequency domain methods are used to observe how the signals' energy varies over a range of frequencies [81,82]. They can both provide a variety of features that can indicate defect formation in a print. Recent in-situ monitoring research has combined acoustic monitoring methods with time and frequency domain methods for feature extraction and defect detection.

In one study, acoustic signals of five different extruder operating conditions in an FFF process were recorded [99]. The experimental setup was similar to that in Fig. 12 with the sensor, a Model MD acoustic sensor, built to eliminate approximately 2 dB of background noise. The sensor operates within a temperature range of −65 to 177 °C with a frequency response of 100–900 kHz. The sampling rate was chosen to be 5 M samples per second. For data classification, SVMs were constructed using the LIBVSM toolbox in MATLAB with time and frequency domain kernels [99]. Signal processing was used to extract features such as ABS-Energy, counts, and peak frequency.

Raw signals from the material loading state and the normal extruding state were recorded and analyzed [99]. It was found that with two-state identification, 100 % accuracy was possible. With multi-state identification, a slightly less accuracy of 97 % was achieved. It was also found that during state transition, time domain features are more sensitive than those of the frequency domain in the evaluation of extruder working conditions of the AM process [99]. ABS-Energy and RMS were found to be sensitive to sensor position. Nonetheless, high amplitudes were found to be indications of crack propagation in the build component. Through feature extraction tools, internal defect initiation can be monitored and defects can be detected. In-situ process control can be possible with the addition of feedback to the printer to create a closed-loop system.

AE waveforms have also been analyzed using time domain, frequency domain, and time–frequency domain methods to characterize the defects formed in a LPBF process [117]. In this study, defects were intentionally formed by varying scan speed and laser power, which would generally cause the energy density of the system to fluctuate. The powder used was gas atomized austenitic steel 316L with particle diameters of around 45 µm. A PAC AM4I acoustic sensor with a frequency range of 0–100 kHz was used to record raw AE signals. A low-pass filter of 100 kHz was added to set a threshold for allowable noise levels and frequencies. For all three methods, a sampling rate of 1 MHz and a window size of 5 ms was chosen. Four defect mechanisms were evaluated: balling, LoF voids, keyholes, and no pores – *no pores* refers to a dense component with entrapped gases that have yet to create complete pores [117]. Analysis involved determining the root mean square (RMS) distribution for the four defect mechanisms. In the time domain, it was found that the signal amplitude varied for each mechanism, increasing in the order: balling, LoF, *no pores*, and then keyhole [117]. Fig. 18 shows a close similarity between keyhole porosity and no pores present, as well as between balling and LoF.

In the frequency domain, frequency ranges were found to correspond to certain defects. The frequency range of 0–100 kHz (limited by the low-pass filter) was split into five equal bands: 0–20, 20–40, 40–60, 60–80, and 80–100 kHz. In the 0–20 kHz band, balling and LoF had the most energy density concentration. For key-

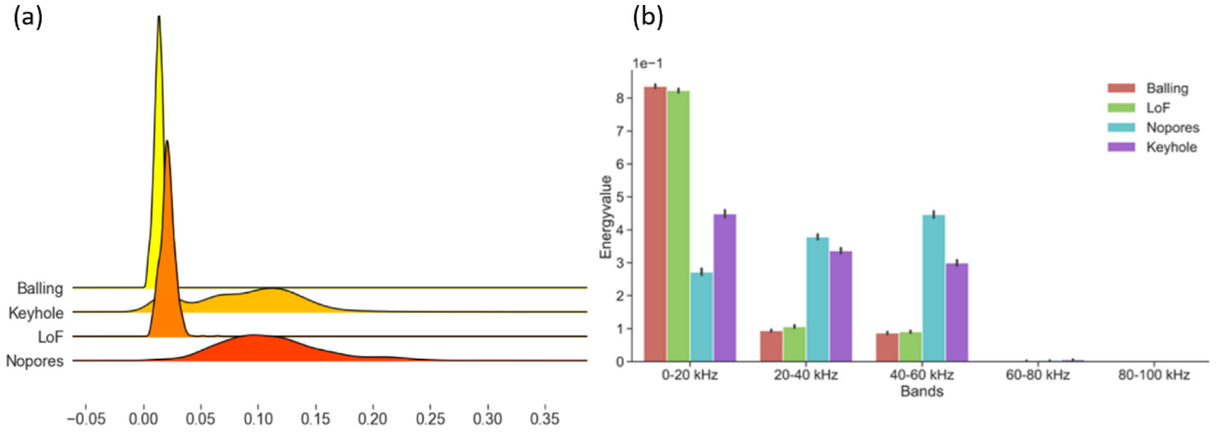

Fig. 18. (a) Distributions of RMS feature and (b) comparison of energy density concentrations for four different defect mechanisms [117].

hole and *no pores*, the energy density concentration was distributed over multiple bands in the frequency range.

Another type of frequency domain feature representation method measured Fast Fourier Transforms (FFT) of the four defect mechanisms. As seen in Fig. 19a, critical peaks occurred at frequencies of 10 and 40 kHz. This is in lieu with the time domain method, where these frequency bands are shown to correspond to the four types of defects. Balling and LoF showed higher power spectral densities at 10 kHz, while keyhole and *no pores* showed higher power spectral densities at 40 kHz. This indicates higher concentrations of energy over those frequency ranges. Peaks in data for keyhole and *no pores* may be the result of recoil pressure and vapor interaction with the material [117]. This information can be used as a baseline to classify defects based on spectral density; however, more research is needed to confirm these findings.

The results shown by the FFT plots (Fig. 19a) were in agreement with results provided by the 3D wavelet transformations (Fig. 19b), which is a subcategory of time–frequency domain analysis. Wavelet coefficient values were found to be higher at 10 kHz and 40 kHz, indicating defect formation. One piece of information that was gained exclusively through this technique was the discontinuity of the distinct peaks. This discontinuity may be a result of the window size or the predictability of the algorithm [117].

Overall, the four defect mechanisms were shown to be directly correlated to the energy density of the system. Balling, LoF, *no pores*, and keyhole all showed discrete energy levels. Frequency domain and time–frequency domain methods were shown to represent similar results. In a subsequent study by the same authors, similar results were confirmed [194]. The research went a step further by using different ML algorithms to determine whether the time, frequency, and time–frequency domain methods were material-dependent when classifying LoF voids, keyhole pores, and conduction-mode melting [194]. Three different material alloys (i.e., stainless steel 316L, bronze, Inconel) were analyzed. Four different ML algorithms were used for classification: Logistic Regression (LR), Random Forest (RF), SVM, and a CNN. For individual alloys, high classification accuracies were achieved: > 90 %, > 92 %, > 89 %, and > 92.5 % for LR, RF, SVM, and CNN, respectively [194]. When classifying the defect mechanisms for all three materials, an ML model was capable of a classification accuracy of > 86 %. Similar to [244], this study demonstrates the benefits of transfer learning during in-situ sub-surface defect detection and its use for process optimization.

A similar approach was taken in other research, where a prepolarized free-field condenser microphone was used to collect AE signals of a LPBF process in the frequency range of 2–20 kHz

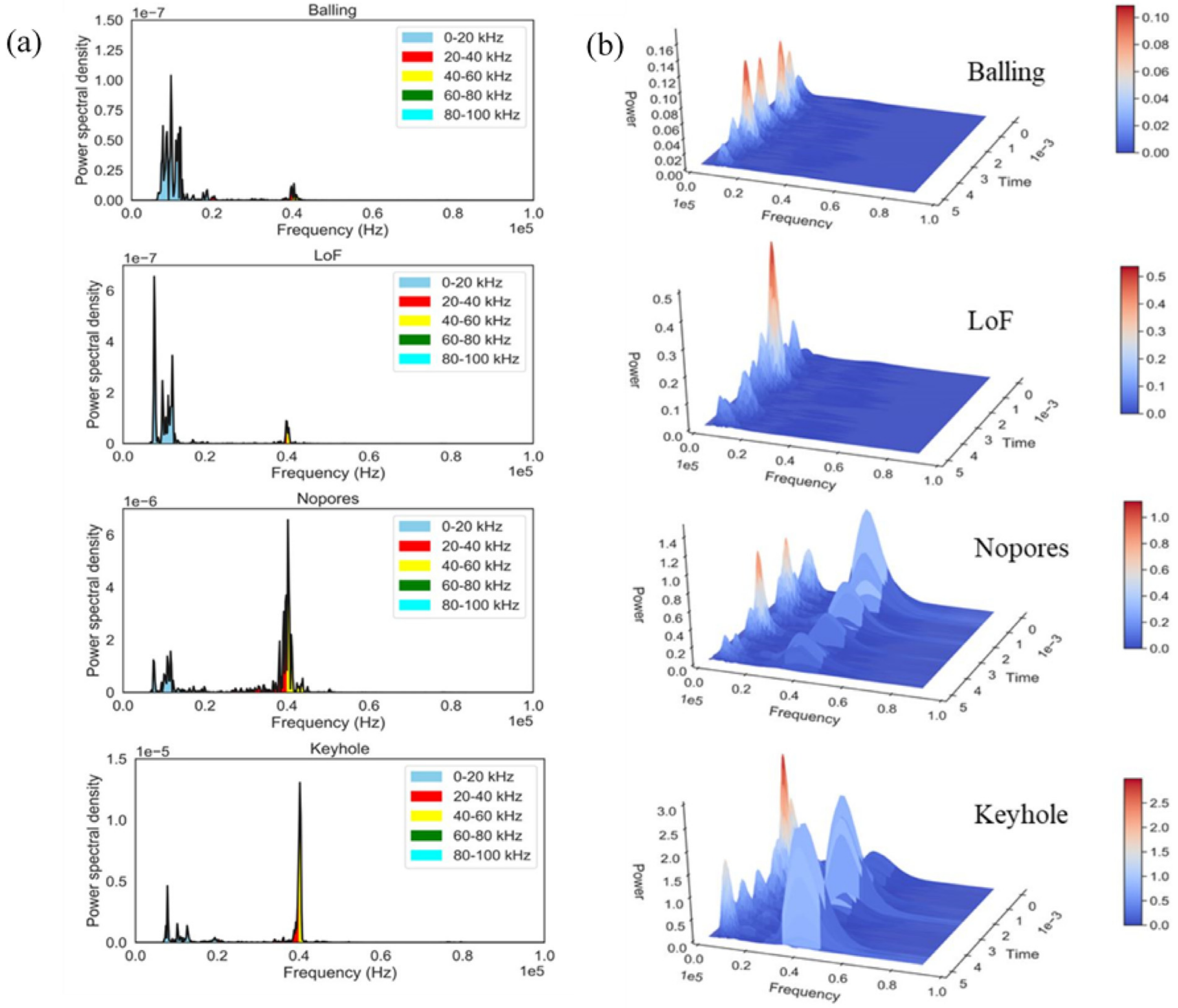

Fig. 19. Comparison of (a) FFT plots and (b) 3D wavelet representation of the acoustic signals for the four defect mechanisms [117].

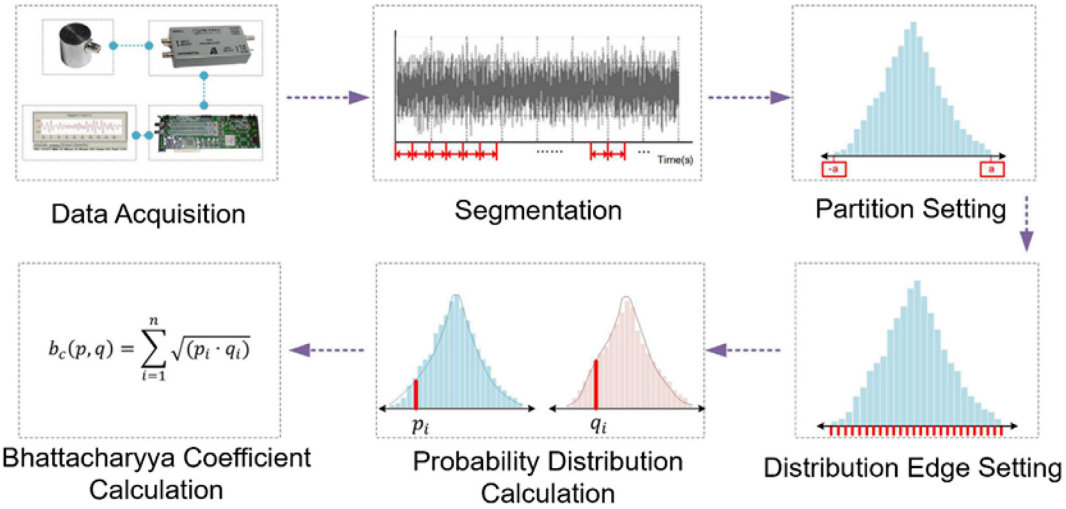

Fig. 20. Procedure for signal processing of AE signal using discrete probability distribution [98].

[195]. In this study, powder layer thickness was modified throughout the experiment. Single tracks were monitored and their geometries at different powder thickness values were analyzed along with FFT amplitudes and average intensities of the AE signals. A 2 kHz high pass filter was used to remove noise from the signals. It was found that AE signals change depending on layer thickness and AE energy increases with layer thickness [195]. As changes in powder layer thickness may correspond to defect formation, this approach has the potential to be used for in-situ monitoring of defect initiation and as a means of defect correction.

3.3.2.3. Probability distribution. Probability distribution can be used for signal processing to characterize signals based on the probability of occurrence, or likelihood, of all possible outcomes. Similar to other data reduction methods, probability distribution also aims to filter out a large number of undesired signals that are collected by acoustic sensors [97]. However, rather than reducing data by thresholding, which would disregard the actual information in the data, it reduces data using a filtration method that assesses the statistical characteristics of the raw AE signal [98]. Consequently, comparison of the data is based on either the asymmetry or overlap of the probability distribution of the AE signals [97,98]. Features are determined from the similarity of the amplitude distribution of each waveform that is output from a signal.

Raw AE waveforms consist of discrete voltage values that have various emissions. Separating these values is a difficult task that can be accomplished through comparison of the discrete probability distributions, or in other words, assessment of the instantaneous skewness – a measure of the asymmetry of the discrete probability distribution of a signal [97]. The process involves the following: elastic waves are collected by the transducer, converted into voltage signals, and then converted into analog signals using an analog-to-digital converter. These analog signals can then be used to determine probabilities.

Several studies of an FFF process have accomplished signal processing through the comparison of two probability distributions using the Bhattacharyya coefficient (BC) [97,98]. BC is a measure of the amount of overlap between two AE signals to produce two forms of similarities: an instantaneous similarity and a relative similarity [98]. The instantaneous similarity refers to the coefficient calculated for each adjacent time section of the probability distributions. The relative similarity refers to the coefficient calculated using the reference distribution. The value of BC is closer to one for signals that are the same or overlap and is closer to zero for those that are different. Fig. 20 demonstrates a step-by-step process for signal processing using discrete probability distribution. For evaluation of the signals, data is first acquired, filtered through using a boundary limit (i.e., segmentation), and then analyzed before it is ready for identification.

In an FFF process, filament feeding produces friction, and thus, generates signals that can be recorded. When the filament clogs the extruder or is no longer fed through it, friction diminishes, and hence, no signals are generated. Therefore, filament breakage mid-process can resemble defect formation; simulating it can also produce a significant change in signal representation that can be analyzed and used to develop defect correction technologies [97,98].

In one of the studies, filament was manually broken 200 mm before entering the extruder. Waveforms generated during the process were recorded using a heat-resistant transducer (100–1000 kHz frequency range) and captured by the data acquisition (DAQ) system as signals [98]. The sampling frequency was chosen to be 2.5 million samples per second (Ms/s), or 2.5 MHz, and waveforms were amplified by 40 dB to capture maximum emissions. Threshold-based features were extracted with a low threshold limit of 30 dB and a frequency of 10 kHz. These features included central frequency, rise time, amplitude and counts.

Two conditions were described to characterize a change in BC: before and after filament breakage. To calculate the similarities, the raw AE signal was split into sections of equal length. As displayed in Fig. 21, filament breakage corresponded to a decrease in BC. After a period of time of filament breakage, signals right before and after a chosen point became similar, which created a steady coefficient value. Compared to instantaneous similarity, the relative similarity comparison gave clearer results in regards to the decreasing BC, as emphasized by the clustering of blue data points in Fig. 21b. Hence, of the two forms of similarities, the relative similarity is more capable of recognizing a change in AE.

Signal processing using a probability distribution method is a viable way to recognize a change in AE signals, or a deviation in signal information. With optimal parameter selection beforehand, such as choice of distribution edge or partition, BC can be calculated promptly, making it a satisfactory method for in-situ monitoring for defect detection.

In a similar study, waveforms of filament bonding failures were collected using four piezoelectric transducers and then analyzed by comparing them to a characteristic value, which was determined by averaging a set of undamaged data sets [104,105]. The experi-

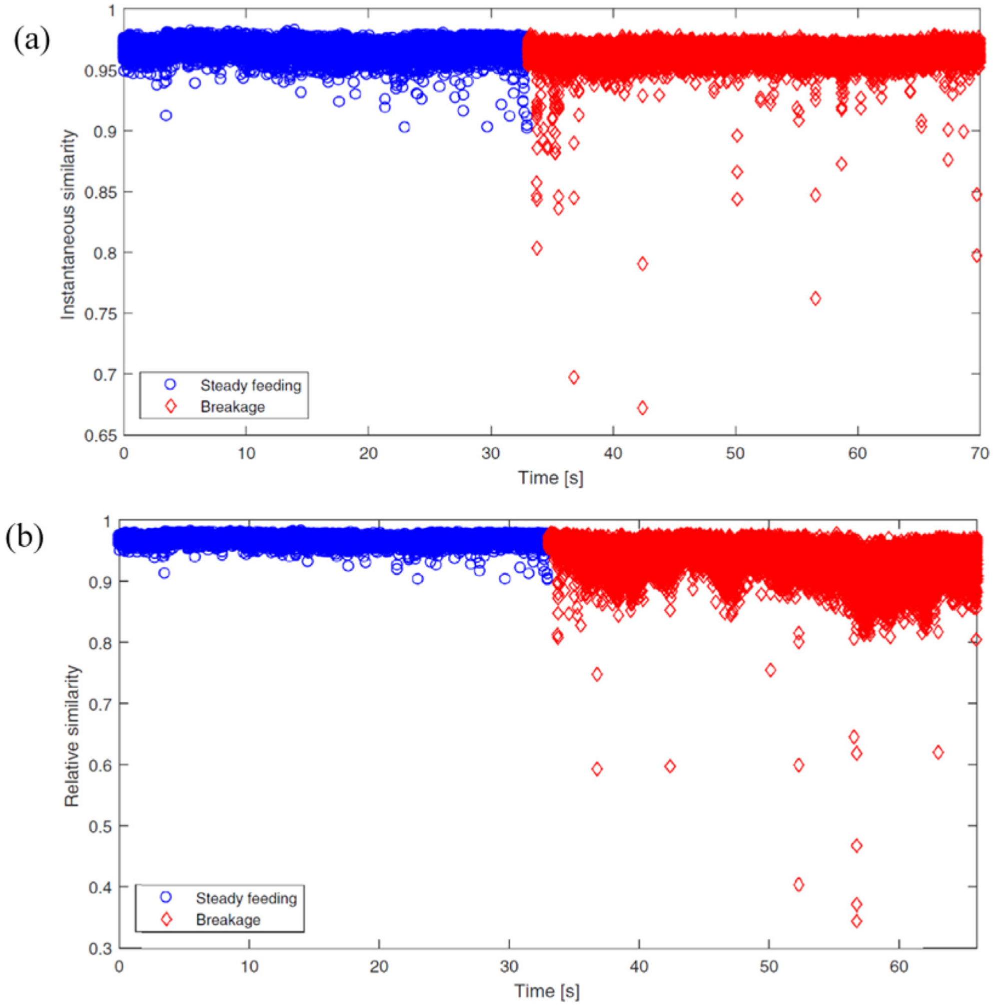

Fig. 21. Signal Processing using the Bhattacharyya coefficient (a) instantaneous similarity and (b) relative similarity [98].

ment utilized the concept of ultrasonic inspection, where transducers were used for deliberate ultrasonic excitation of the printer, leading to filament bonding failures, and hence, defect formation. A frequency range of 50–100 kHz was investigated, and a sampling rate of 0.333 Ms/s was chosen [104]. Signals were processed by calculating the Mahalanobis Distance, a probability distribution similar to BC. Data collection through acoustic signal acquisition and 3D data visualization was successful; however, results were inconclusive and did not provide a reliable means for defect detection. It was concluded, however, that AE signal acquisition using ultrasonic inspection and signal processing using this probability distribution technique can be utilized with more accuracy on different printers using a feed material of high-resolution plastic and metal, as signals would propagate with less attenuation and appear with less variance [104].

3.3.2.4. Statistical clustering. Clustering is a mining method used for data grouping, classification, and fault diagnosis [237]. It is a method that attempts to extract features from the data that are in proximity, rather than those that are deeper in the structure. One type of clustering algorithm used for signal processing in AM is K-means clustering [84]. This algorithm utilizes an objective function called the residual sum of squares (RSS), with the goal of minimizing the function to obtain a local minimum [84]. It is fast in processing large amounts of data, as well as efficient in classifying data points with predefined number of clusters or, in this case, process parameters. For these reasons, K-means clustering can be used for feature extraction and classification under different process parameters with good accuracy.

In a recent study, K-means clustering was used to classify different process conditions from acoustic signals gathered during a DED process that used Ti-6Al-4 V alloy powder as feedstock [81,84]. Transducers were mounted to the bottom of an adapter plate that carried the build plate on the other side. This adaptor plate was mounted on an additional plate to allow clearance for the acoustic sensors. An eight-channel DAQ system was used to continuously collect acoustic signatures at five different states. A sampling frequency of 5 MHz was chosen [81]. A bandpass filter was used that allowed frequencies in the range of 100–2000 kHz. Process conditions (i.e., optimum process, laser power, low powder feed) were classified into different variables. Features were extracted from the frequency response of the acoustic signatures. The range of frequencies observed were classified as either low (<800 kHz) or high (>800 kHz) frequency. It was found that process conditions can be classified under different frequency bands with 87 % accuracy. Background noise was differentiated from the process conditions using this signal processing method. Graphical representations of the clusters proved useful in evaluating the accuracy of process condition classification.

In another study of a DED process, K-means clustering was successful in distinguishing between cracks and porosities [90]. An acoustic sensor with a bandwidth of 100–1000 kHz was used to record signals of the AM process. Internal cracks and porosities were created by mixing the bulk Ti-6Al-4 V powder with tool steel powder. Typical steps of the DAQ and signal processing process resonate with Fig. 16. Only bandwidths within the range of 100 kHz to 1 MHz were detected. AE features such as rise time, peak amplitude, number of counts, energy, and frequency were extracted from the AE signals. Graphical representations of clusters were compared to analyze these features. Results clearly distinguished between internal cracks and porosities: cracks triggered signals with short durations and high amplitudes, while porosities produced signals with shorter decay time and less amplitude [90]. The signal energy was determined to be a key factor in effective signal processing.

In other research, a signal post-processing framework was introduced to reduce the number of features required to represent AE activity by utilizing clustering [236]. Data was also collected in-situ, but using scanning electron microscopy (SEM) and nano-indentation setups, rather than optical and acoustic methods. By analyzing the different features, their correlations and their variance, data clusters were formed that could be examined in relation to data acquired through in-situ monitoring methods. This framework has potential for use with AM technologies for defect detection through AE sensing.

4. Ex-situ validation for a-priori identification through XCT

XCT is an NDT technique that has been used for ex-situ quality assessment and defect detection in many fields, such as the medical field, where 3D printed medical components are evaluated for defect detection [247,248]. In AM, XCT can be used for defect detection validation, as well as dimension evaluation, density measurement, and roughness analysis to assist in control of the printing process [246,249,250]. Furthermore, when combined with data fusion concepts, ex-situ validation using XCT can lead to a better in-depth evaluation of defects.

The process of XCT is shown in Fig. 22, where a 3D-printed part is rotated about an axis and exposed to an X-ray source at different angles. X-ray images are collected from the X-ray source using a flat panel detector. These 2D gray-scale images are stacked to form a 3D dynamic of the specimen, which typically has a size of 1000 × 1000 × 1000 voxels [249]. Each point or pixel of an image for a given voxel is correlated to the average density and composition of the material being evaluated. Therefore, a long scan time of the examined part is required for high quality XCT images. This can lead to the accumulation of large file sizes, which is a major obstacle for in-situ monitoring and ex-situ validation technologies as ML algorithms are restricted by size capacity. For instance, if each voxel is a 2-byte integer, the entire 3D image stack will be stored as a 2-gigabyte file [249].

In past studies, XCT has been used to study the effects of process parameters on defects [19]. It was concluded that the control of laser power had the largest effect on avoiding defect formation. In recent years, XCT has been used to determine mechanical properties of 3D printed components, such as surface roughness and areal surface information effects [251–253]. It has also been used for fatigue analysis of 3D printed components as it corresponds to manufacturing defect size and locations [254,255]. Similarly, μCT has been used to examine the influence of internal and surface defects on the mechanical responses of defect-embedded lattice struts manufactured using LPBF [256]. From the μCT models, FEM models, and tensile testing results, surface defects were found to have considerable impacts on elastic and initial yielding responses, while internal defects had little to no influence on those values. μCT voxel size was found to affect both global mechanical response and localization [256].

More importantly, as highlighted earlier, XCT has been used for ex-situ validation and inspection of defect formation with great success [181,182,257]. In one study, images obtained using XCT provided similar defect locations to those captured using the Basler optical camera [181]. Validation of data was possible at a depth of 30–50 μm from the surface. Fig. 23 compares optical images captured in-situ to XCT images of a specific layer of the 3D printed Pythagorean geometry. Images were processed and overlaid to emphasize the comparison of defect locations. Large defects in the samples, with sizes of about 100 μm, could be easily identified using this technology, but smaller defects or cracking could not be seen, likely due to resolution limitations or complex cracking mechanisms [181]. As the laser completed a raster pattern at a particular section of a layer, areas with defects maintained a high IR intensity after the laser had already passed [181]. Furthermore, peaks in IR intensity signaled the formation of defects. Through cross-comparison of IR and XCT data, cracking tendency can be predicted.

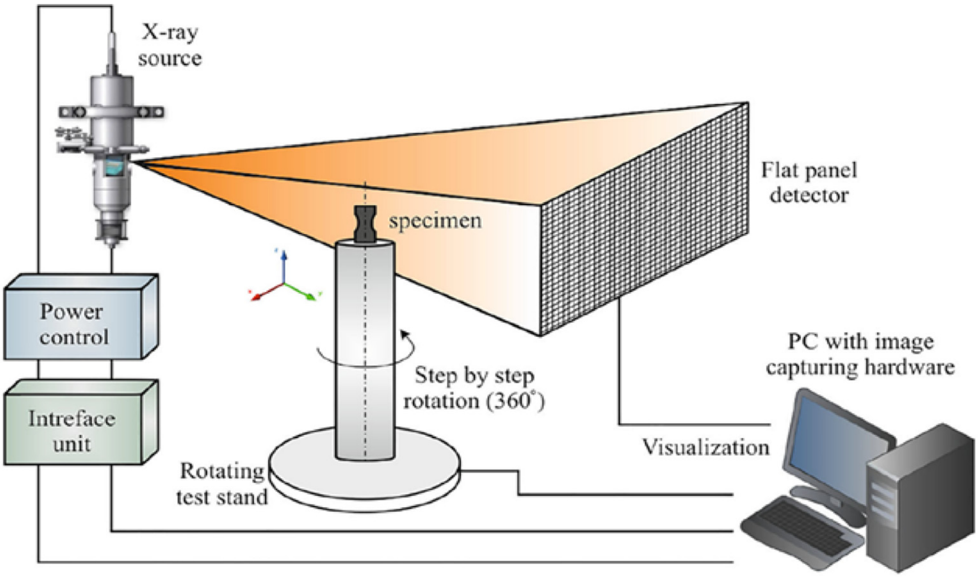

Fig. 22. Schematic of XCT Process [249].

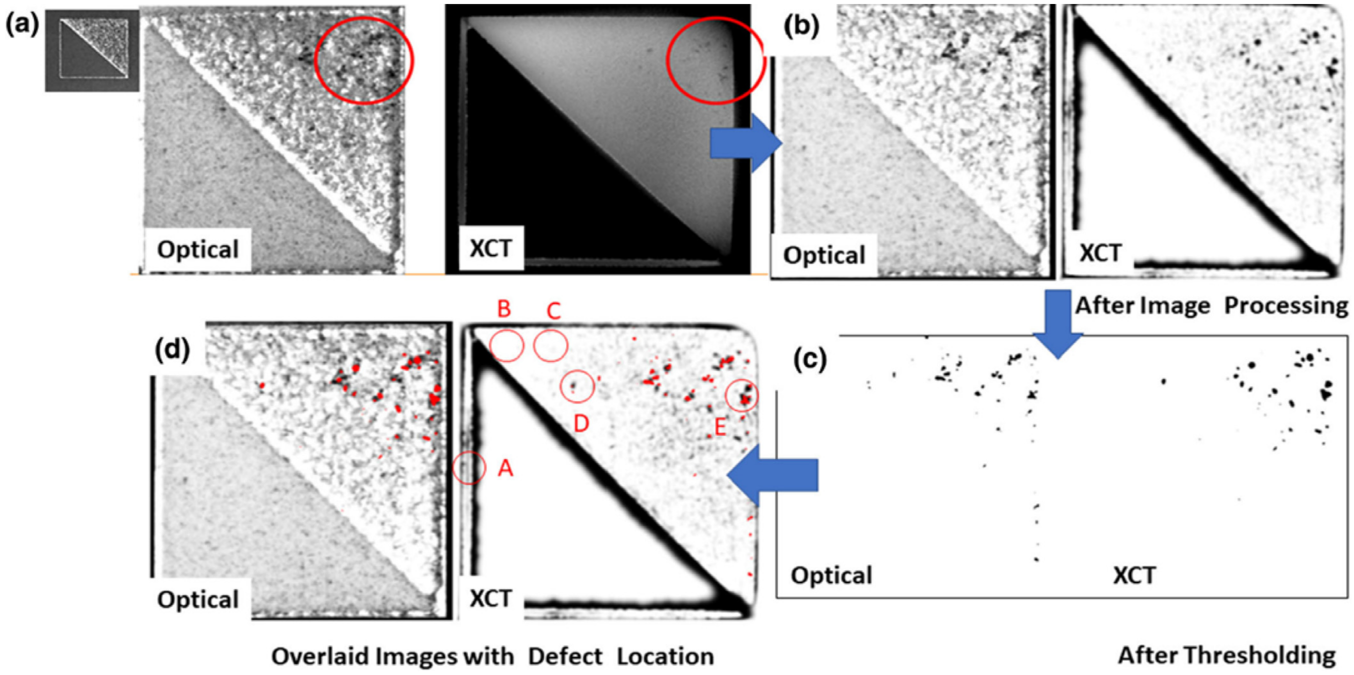

Fig. 23. Comparison between in-situ optical images and XCT images from the approximate location for the same layer (a) raw images, (b) images after processing to reduce background: normalization, contrast, pixel enhancement, and thresholding, (c) threshold images outlining defects, (d) overlaid images – a combination of *b* and *c* – showing correlation between in-situ optical images and XCT images with five distinct locations identified for analysis [181].

In another study, both NDT using µCT and destructive inspection were used to analyze and compare defect mappings from in-situ optical images to ex-situ data [182]. Data was collected, and raw signals were processed using the concept of time over threshold (TOT), or time over a defined apparent temperature. The scanning pattern used highlighted the pores and LoF voids in the three cubic-shaped specimens; differences in overlaid data could be correlated to defect formation and LoF void clusters. Destructive metallography was used to measure melt pool depth. Light microscopy helped in characterizing the parts based on volumetric energy density, melt pool depth, and defect formation [182]. Elastix 4.9 was used to overlay all datasets: Fig. 24 compares in-situ monitoring data to ex-situ validation data for two different layers in Volume B of the specimen. A contour map plot for a threshold value of 30 ms in the TOT map is overlaid on the other graphical representations to understand the similarities in the datasets, as well as

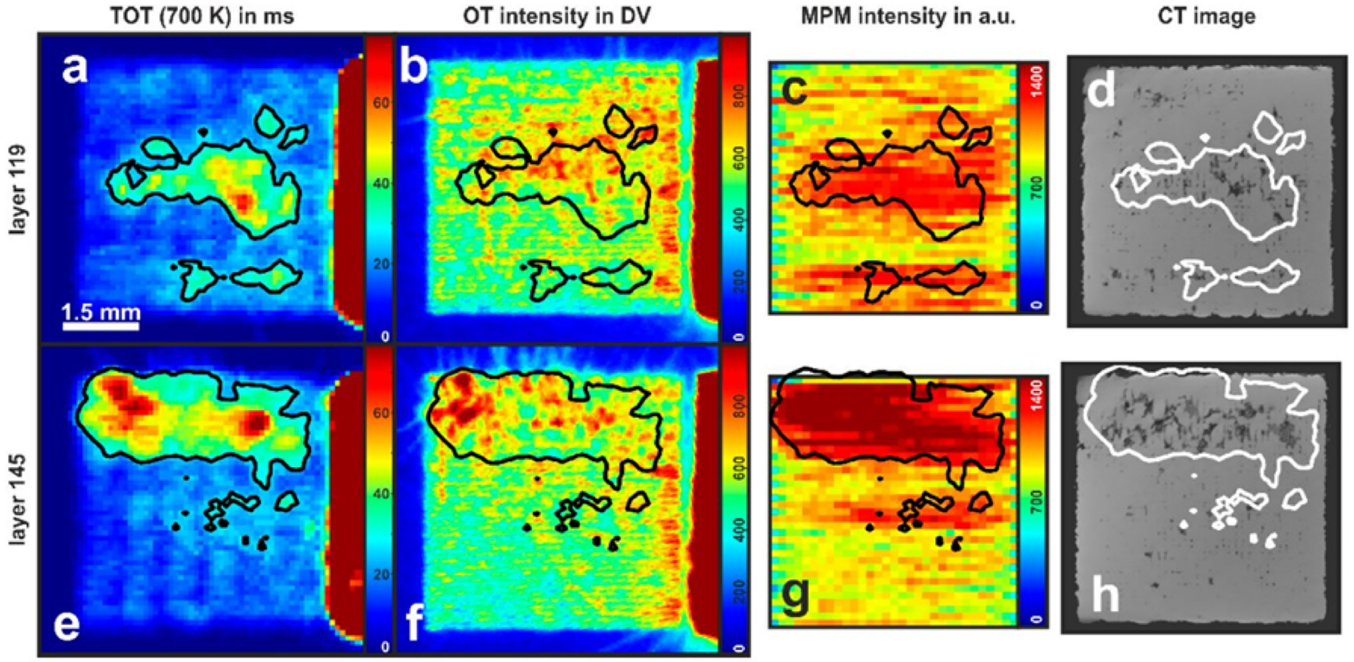

Fig. 24. Comparison of in-situ monitoring data – TOT (700 K), OT intensity, and MPM intensity – with µCT data for (a-d) layer 119 and (e-h) layer 145 of Volume B with low VED. A contour plot from the TOT (700 k) dataset at a threshold value of 30 ms is overlaid on other graphical representations to emphasize similarities in datasets [182].

identify any indication of defect formation in the specimen. As would be expected, Melt-Pool-Monitoring (MPM) intensity maps, gathered from commercial monitoring equipment, were shown to be more closely correlated to μCT data, followed by TOT (700 K) data, and then optical tomography (OT) intensity data. A binary overlap of thermographic anomalies and μCT data showed 71 % similarity in terms of defect detection. More stringent data fusion techniques are needed for a complete comparison of signals to detected defects [182].

Other works have combined ex-situ validation with ML methods for the purpose of defect detection. In several studies, in-situ image acquisition with a coaxial system combined with ex-situ XCT scanning of cross-sections was capable of detecting porosities that were then classified using neural network methods [232,258]. In another study, an ANN-based algorithm was applied to a μCT image dataset to identify defects in composites 3D printed using FFF [246]. Results were compared with observations obtained from SEM. As seen in Fig. 25, the resolution of μCT images is lower than that of SEM images, while SEM can capture more defects than μCT. Furthermore, the imaging artifacts may skew the results obtained on defects, especially those within geometries that are complex or challenging to manufacture. This may lead to overlapping projections, shadow effects and scattering, which can increase the presence of noise.

XCT for ex-situ inspection and validation has proven to be very important for understanding the capabilities and limitations of in-situ monitoring methods and devices. For example, a big drawback of in-situ analysis is that false positives can often appear in a dataset. An accumulation of heat from the laser can cause remelting and resolidification in certain areas of the printed component, which can lead to false-positive defect identification. With ex-situ validation, this can be avoided – one of the collected μCT images in [182] showed a defect in one layer that was later healed by the laser-material interaction in the subsequent layer above it. μCT has also been used to spot certain types of layered defects with ease due to its high spatial resolution [259].

Several limitations have been found to affect XCT data and analysis, such as pore size limits and energy densities. Increasing energy density in a region can reduce pore populations [260]. Also, materials with higher densities are more difficult to observe and evaluate using XCT due to a reduced exposure to X-ray beams. Overall, porosity levels and defect sizes captured using XCT technologies are limited by the chosen process parameters [261].

Aside from XCT, ex-situ verification can also be performed through other NDT methods such as neutron dark-field imaging and laser-scanning vibrometry. Neutron dark-field imaging (DFI) has been used to investigate microstructural features in additive manufactured steels through qualitative analyses of porosity levels

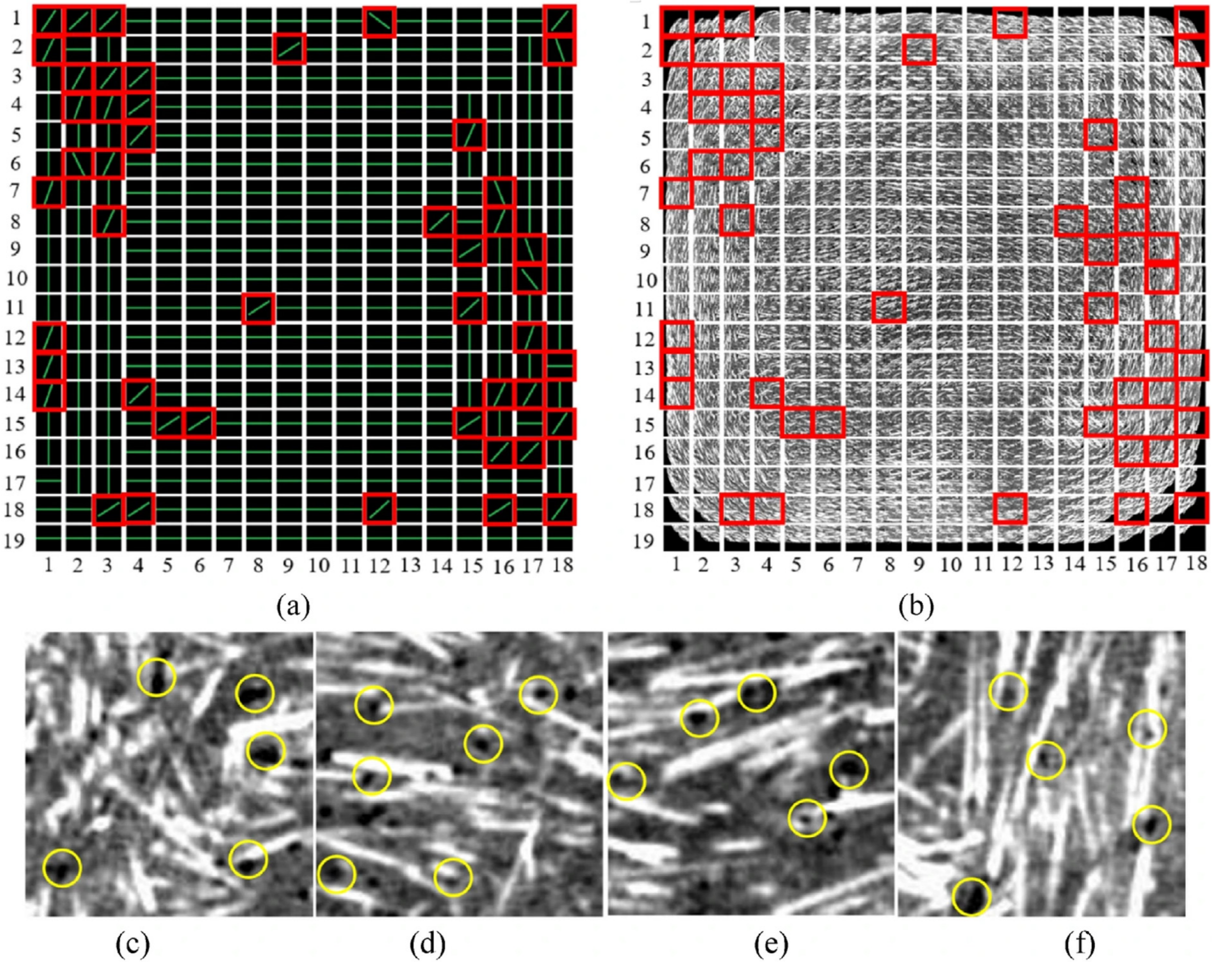

(a) (b)

(c) (d) (e) (f)

Fig. 25. (a) A machine learning algorithm is designed to segment each μCT image slice to an array of 19 × 19 images. (b) The fiber orientation in each slice is determined using an ANN based ML method. The deviation in the fiber orientation prediction from the actual direction is taken as an indication of a defect, which is confirmed by inspection of various segmented images in (c-f) [246].

and phase transformations [262]. Laser-scanning vibrometry has been used to evaluate the mechanical and dynamical behavior of parts manufactured using FFF [263]. Using regression models, the influence of process parameters on the elastic modulus of the printed rectangular prisms was evaluated.

5. Experimentation: Procedure and mitigation strategies

Introduced here, is a general procedure that can be followed, as well as basic guidelines and mitigation strategies that can be used to achieve accurate defect detection and/or in-situ defect correction with in-situ monitoring.

To perform an in-situ monitoring experiment, first, a 3D CAD model is created. Defects can be formed in the model in multiple ways. They can be intentionally input in the 3D geometry during design or created by manipulating the printing process parameters to form different concentrations throughout the structure, which can lead to the formation of defects [264]. Algorithms can also be developed to randomly insert defects in the sliced models or G-codes [265]. Irrespective of the method used, the model must be sliced before being input to the 3D printer for printing. A monitoring system setup around or within the 3D printer can consist of one or a combination of devices, such as those listed in Table 3, along with a DAQ system, if necessary. The monitoring system will then output raw data that can be used for in-situ analysis.

Critical information pertaining to detect formation can be extracted from the raw data using methods such as image processing, signal processing, data fusion or other image/signal registration methods. Data correlation can occur through either of the data validation strategies: Post-process Validation or A-Priori Identification. For example, data can be compared to that of a healthy 3D CAD model or G-code of the same geometry to identify out-of-control or instable conditions. The comparison can be made in a layer-by-layer manner in-situ, where as soon as a defect is detected in a given layer, the print comes to a stop. Data can also be acquired and used for ex-situ validation, using methods such as μCT.

To make use of data that is acquired during the layer-wise manufacturing process, algorithms can be developed and used to spot defects or out-of-control conditions as the part is being printed [9,103,172,189,190,245,264–268]. These ML algorithms can work to identify pores and defects in layers. For example, anomaly detection can be used to identify patterns in the data that relate to abnormal behavior. By utilizing data fusion techniques, multiple visual or XCT images can be overlaid to create an overall depiction of the printing process.

Moreover, image processing methods can be used to achieve a variety of different results. In a recent study, an algorithm was created that displayed colors on the surface of the layers when pores and defects were existent [264]. When analyzing layers without pores, no colors were present on the surface. In IR images, areas of materials with higher heat radiation can be signified by a general color scheme of which some colors correspond to flaws or irregularities. Image registration methods, such as Digital Image Correlation (DIC) methods, can also be used for both in-situ and ex-situ defect characterization, as well as real-time feedback control [213,269,270]. DIC allows for 3D full-field optical measurements of displacements, strains, deformations, or vibrations, and tracking and registration of the results. It can provide visual representations of these measurements for an accurate characterization of the process deviation [269]. For more information about DIC applications for in-situ monitoring in AM, refer to [213,270].

Monitoring methods introduced in this review present several disadvantages that need be addressed during experimentation. Some potential risks of image acquisition using optical and thermal imaging methods are limitations to spatial resolution and surface measurements, limitations to accurate thermographic measurements, and insufficient temporal resolution for the analysis of the transient events that occur during the printing process. These issues can be mitigated by acquiring better high-resolution and high-frame rate cameras for high quality image acquisition. Another potential risk is limited access to in-depth information of defects from images due to system noise and vibration. This can be amended through image processing algorithms such as contrast enhancement to develop clean images. Background subtraction can allow for more focus on specific regions of interest. Other factors of the monitoring setup that have effects on raw image data quality, such as camera position and angle, additional illumination, and the installation of camera shields, must be considered.

Accurate feature extraction and defect detection using AE in-situ monitoring can be achieved through optimal choice of acoustic sensors, sensing technologies, and DAQ modules. Background noise reduction and high signal-to-noise ratios can facilitate signal processing. Optimal sampling rates, threshold limits, and window spans can ensure that only required data is captured by the sensors for analysis. Passive filters can be used to limit acceptable frequency ranges. Some disadvantages of μCT for ex-situ validation are limitations identifying parts manufactured with high energy densities or specific process parameters. Such limitations can affect exposure capabilities of μCT, as well as pore size limits. They can be mitigated through appropriate choice of monitoring setups and printing process parameters.

6. Future work

Extensive literature review has allowed identifying several future research directions that can move the field forward. Developing a cost-effective and efficient monitoring setup is a major challenge requires deep understanding of the AM process and instrumentation. The combination of optical and acoustic methods for in-situ monitoring requires better understanding of the benefits each monitoring method can provide when used simultaneously. Furthermore, the need for data fusion techniques for real-time optical and acoustic signal processing is apparent. The application of data fusion in-situ is necessary to take full advantage of complex monitoring setups for defect detection. This would require knowledge of both the mechanical systems and ML models used.

Representation and analysis of acquired in-situ data from imaging methods, as well as the means of data processing, requires more research. The implementation of different ML algorithms to AM can improve data processing. By doing so, critical information about defect formation can be obtained: events leading up to defect formation and after continuation of the print. Defects can also be characterized by type and optimum process parameters for AM can be determined. Locations of failure in 3D printed components can be estimated prior to initiation and avoided in future manufacturing.

Regarding acoustic methods, future work can involve determination of optimal threshold limits and sampling rates for specific sensors and to develop a standard by which researchers can reference. Another potential research area is to experiment with low-pass filters for signal processing, possibly-one that allows higher frequency ranges. Moreover, the application of different time scales can help in understanding their effects on AE signal feature representation.

Defect correction methods are in early stages at this time. Some that have been introduced in literature include automatic process parameter adjustment and post-processing treatments, such as HIP. Future work in this area should involve determining the accuracy of current defect correction methods, as well as developing new strategies that make the AM process both time- and resource- efficient. All research into in-situ monitoring and control of the printing process should be built on the concept of developing a closed-loop process capable of instantaneous feedback.

7. Conclusions

In-situ monitoring methods can provide a means to detect internal or sub-surface defect formation in AM processes in real-time and help in understanding defect formation in 3D printed parts. A system can be established to monitor the defects as they form and develop strategies to mitigate their impact on product quality. A variety of process monitoring methods have been introduced in this review, as well as strategies and procedures that can be used to process monitoring data and acquire information relevant to defect initiation and formation.

Imaging methods utilize visual and thermal monitoring devices, such as high-speed optical cameras, IR cameras and X-ray imaging. Images captured using imaging devices can be examined for events leading up to defect formation using methods like image segmentation and statistical analysis. IR cameras were found to show sub-surface and internal defect formation tendency in the part with sizes up to 1000 μm, as well as detect vapor plume and powder spatter ejection in the printing process. X-ray imaging was found to identify depressions and other melt pool characteristics. Simultaneous use of imaging methods provided a way to study melt pool dynamics in 3D and detect sub-surface defects in printed components with sizes as small as 50 μm.

Acoustic sensors are used to record acoustic signals generated from the printing process, which are then analyzed to provide critical information about the formation of internal defects in a printed part. A variety of signal processing methods were found to facilitate feature extraction through techniques such as thresholding and background noise reduction. Certain frequency ranges, window sizes, time spans, and energy density concentrations were found to correlate to the formation of certain internal defects.

XCT was introduced on a unit- and micro-scale level. Unlike in-situ monitoring imaging methods, XCT is a post-printing ex-situ process for inspection and validation. XCT and in-situ optical images can be compared to estimate defect locations. XCT also provides a way to identify large or multi-layer defects in a printed component. More research is needed to improve data fusion and overlaying concepts, as well as provide complex data analysis techniques.

Despite their capabilities, some disadvantages of imaging methods are limited access to in-depth information, limitations to spatial resolution and surface measurements, limitations to accurate thermographic measurements, and insufficient temporal resolution for the analysis of the transient events that occur during the printing process. Disadvantages of acoustic methods include sensitivity to weak emission signals and background noise. This can disturb signal measurements and expose the vulnerabilities of signal processing methods.

Nonetheless, by integrating image and acoustic signal processing methods into the printing and monitoring process, real-time feedback control is plausible. Such methods can be used to identify defect initiation in a printed component and either stop the print or correct defects in-situ. Through the implementation of ML algorithms, data registration and segmentation can be accomplished. Defects can be characterized by type and optimum printing process parameters can be determined. Ultimately, in-situ process monitoring methods can create a closed-loop AM process capable of defect correction and control, to ensure process stability and repeatability.

Data availability

No data was used for the research described in the article.

Declaration of Competing Interest

The authors declare that they have no known competing financial interests or personal relationships that could have appeared to influence the work reported in this paper.

Acknowledgments

The work is supported by the SecureAmerica Institute grant from the Texas A&M Engineering Experiment Station and the National Science Foundation grant CMMI-2036802. The views expressed in this article are those of the authors and not of the funding agencies. The authors have collected literature to the best of their abilities and overlooking some papers is imperative in the vast amount of available literature.

References

[1] B. Poorganji, E. Ott, R. Kelkar, A. Wessman, M. Jamshidina, Review: Materials Ecosystem for Additive Manufacturing Powder Bed Fusion Processes, JOM 72 (1) (2019) 561–576.

[2] M. Lutter-Gunther, C. Gebbe, T. Kamps, C. Seidel, G. Reinhart, Powder recycling in laser beam melting: strategies, consumption moedling and influence on resource efficiency, Prod. Eng. Res. Devel. 12 (2018) 377–389.

[3] X. Yang, D. Zhao-wang, G. Xue-yi, T. Qing-hua, L. Yong, Towards a circular metal additive manufacturing through recycling of materials: A mini review, J. Central South University 27 (2020) 1134–1145.

[4] D. V. Betim, M. C. Heymann, O. L. G. Quelhas, R. G. G. Caiado and H. G. Costa, "Analysis of the Application of Additive Manufacturing in the Circular Economy: An Integrative Literature Review," in *Operations Management for Social Good*, Springer Proceedings for Business and Economics, 2020, pp. 1075-1084.

[5] J. Oliveira, A. LaLonde and J. Ma, "Processing parameters in laser powder bed fusion metal additive manufacturing," *Materials and Design,* vol. 193 (108762), 2020.

[6] T. DebRoy, H. Wei, J. Zuback, T. Mukherjee, J. Elmer, J. Milewski, A. Beese, A. Wilson-Heid, A. De, W. Zhang, Additive manufacturing of metallic components - Process, structure and properties, Prog. Mater Sci. 92 (2018) 112–224.

[7] R. Li, M. Jin and V. C. Paquit, "Geometrical defect detection for additive manufacturing with machine learning models," *Materials & Design,* vol. 206 (109726), 2021.

[8] M.S. Hossain, H. Taheri, In Situ Process Monitoring for Additive Manufacturing Through Acoustic Techniques, Journals of Materials Engineering and Performance 29 (10) (2020) 6249–6262.

[9] G. Masinelli, S.A. Shevchik, V. Pandiyan, T. Quang-Le, K. Wasmer, "Artificial Intelligence for Monitoring and Control of Metal Additive Manufacturing," in *Industrializing Additive Manufacturing,* Springer Nature Switzerland (2021) 205–220.

[10] S.K. Everton, M. Hirsch, P. Stravroulakis, R.K. Leach, A.T. Clare, Review of in-situ process monitoring and in-situ metrology for metal additive manufacturing, Mater. Des. 95 (2016) 431–445.

[11] A. Oleff, B. Kuster, M. Stonis, L. Overmeyer, Process monitoring for material extrusion additive manufacturing: a state-of-the-art review, Progress in Additive Manufacturing 6 (2021) 705–730.

[12] Y. Fu, A. Downey, L. Yuan, A. Pratt and Y. Balogun, "In situ monitoring for fused filament fabrication process: A review," *Additive Manufacturing,* vol. 38 (101749), 2021.

[13] L. Kong, X. Peng, Y. Chen, P. Wang and M. Xu, "Multi-sensor measurement and data fusion technology for manufacturing process monitoring: a literature review," *International Journal of Extreme Manufacturing,* vol. 2 (022001), 2020.

[14] M. Grasso, A. Remani, A. Dickins, B. M. Colosimo and R. K. Leach, "In-situ measurement and monitoring methods for metal powder bed fusion: an updated review," *Measurement Science and Technology,* vol. 32 (112001), 2021.

[15] R. McCann, M. A. Obeidi, C. Hughes, E. McCarthy, D. S. Egan, R. K. Vijayaraghavan, A. M. Joshi, V. A. Garzon, D. P. Dowling, P. J. McNally and D. Brabazon, "In-situ sensing, process monitoring and machine control in Laser Powder Bed Fusion: A review," *Additive Manufacturing,* vol. 45 (102058), 2021.

[16] B. Wu, X.-Y. Ji, J.-X. Zhou, H.-Q. Yang, D.-J. Peng, Z.-M. Wang, Y.-J. Wu, Y.-J. Yin, In situ monitoring methods for selective laser melting additive manufacturing process based on images - A review, China Foundry 18 (4) (2021) 265–285.

[17] Z.-J. Tang, W.-W. Liu, Y.-W. Wang, K.M. Saleheen, Z.-C. Liu, S.-T. Peng, Z. Zhang, H.-C. Zhang, A review of in situ monitoring technology for directed energy deposition of metals, The International Journal of Advanced Manufacturing Technology 108 (2020) 3437–3463.

[18] A. Charles, M. Salem, M. Moshiri, A. Elkaseer, S.G. Scholz, "In-Process Digital Monitoring of Additive Manufacturing: Proposed Machine Learning Approach and Potential Implications on Sustainability," in *Sustainable Design and Manufacturing*, Springer Nature, Singapore, 2020, pp. 297–306.

[19] Y. Wang, X. Chen, J. Jayalakshmi, R. A. Singh, K. Sergey and M. Gupta, "Process Parameters, Product Quality Monitoring, and Control of Powder Bed Fusion," in *Transactions on Intelligent Welding Manufacturing*, vol. 3, S. Chen, Ed., Singapore, Springer Nature, 2020, pp. 89-108.

[20] B. Gould, S. Wolff, N. Parab and C. Zhao, "In Situ Analysis of Laser Powder Bed Fusion Using Simultaneous High-Speed Infrared and X-ray Imaging," *JOM: the journal of the Minerals, Metals & Materials Society*, vol. 73, no. 1, 2020.

[21] T. G. Spears and S. A. Gold, "In-process sensing in selective laser melting (SLM) additive manufacturing," *Integrating Materials and Manufacturing Innovation*, vol. 5, no. 2, 2016.

[22] T. Furumoto, M.R. Alkahari, T. Ueda, M.S. Abdul Aziz, A. Hosokawa, Monitoring of laser consolidation process of metal powder with high speed video camera, Physics Procedia 39 (2012) 760–766.

[23] T. Furumoto, T. Ueda, M.R. Alkahari, A. Hosokawa, Investigation of laser consolidation process for metal powder by two-color pyrometer and high-speed video camera, CIRP Annals - Manufacturing Technology 62 (2013) 223–226.

[24] T. Furumoto, T. Ueda, N. Kobayashi, A. Yassin, A. Hosokawa, S. Abe, Study on laser consolidation of metal powder with Yb:fiber laser - Evaluation of line consolidation structure, J. Mater. Process. Technol. 209 (2009) 5973–5980.

[25] M. Pavlov, M. Doubenskaia, I. Smurov, Pyrometric analysis of thermal processes in SLM technology, Physics Procedia 5 (2010) 523–531.

[26] B. Falk, S.M. Vallinas, J.V. Crivello, Monitoring photopolymerization reactions with optimal pyrometry, Polym. Chem. 41 (4) (2003) 579–596.

[27] W. Hong, Y.T. Lee, H. Gong, Thermal analysis of layer formation in a stepless rapid prototyping process, Appl. Therm. Eng. 24 (2–3) (2004) 255–268.

[28] P. Lin, B. Falk, M. Jang, J.V. Crivello, Study of Laser-Induced Photopolymerizations by Optical Pyrometry, Macromol. Chem. Phys. 205 (15) (2004) 2040–2047.

[29] A. S. Jariwala, R. E. Schwerzel and D. W. Rosen, "Real-time interferometric monitoring system for exposure controlled projection lithography," in *ASME/ISCIE 2012 International Symposium on Flexible Automation*, Atlanta, 2012.

[30] J. Wang, C. Zhao, Y. Zhang, A. Jariwala and D. Rosen, "Process modeling and in-situ monitoring of photopolymerization for exposure controlled projection lithography (ECPL)," in *Proceedings of the 28th Annual International Solid Freeform Fabrication Symposium*, Atlanta, 2017.

[31] X. Zhao, Process measurement and control for exposure controlled projection lithography, Atlanta (2017).

[32] X. Zhao and D. W. Rosen, "Real-time interferometric monitoring and measuring of photopolymerization based stereolithographic additive manufacturing process: sensor model and algorithm," *Measurement Science and Technology*, vol. 28 (015001), 2017.

[33] X. Zhao, D.W. Rosen, An implementation of real-time feedback control of cured part height in Exposure Controlled Projection Lithography with in-situ interferometric measurement feedback, Addit. Manuf. 23 (2018) 253–263.

[34] I. Alig, D. Lellinger, S. Agarwal, H. Oehler, Monitoring of photopolymerization kinetics and network formation by combined real-time near-infrared spectroscopy and ultrasonic reflectometry, React. Funct. Polym. 73 (2) (2013) 316–322.

[35] K. Xu, Y. Chen, Photocuring Temperature Study for Curl Distortion Control in Projection-Based Stereolithography, J. Manuf. Sci. Eng. 139 (2017) 021002–21011.

[36] T. Hafkamp, G. van Baars, B. d. Jager and P. Etman, "Real-time feedback controlled conversion in vat polymerization of ceramics: A proof of principle," *Additive Manufacturing*, vol. 30 (100775), 2019.

[37] W. Wu, D. Qi, W. Hu, L. Xi, L. Sun, B. Liao, F. Berto, G. Qian and D. Xiao, "Synchrotron X-ray micro-computed tomography imaging of 3D re-entrant micro lattice during in situ micro compression experimental process," *Materials and Design*, vol. 192 (108743), 2020.

[38] K.-S. Kwon, Speed measurement of ink droplet by using edge detection techniques, Measurement 42 (2009) 44–50.

[39] T. Wang, T.-H. Kwok, C. Zhou, S. Vader, In-situ droplet inspection and closed-loop control system using machine learning for liquid metal jet printing, J. Manuf. Syst. 47 (2018) 83–92.

[40] A. Wang, T. Wang, C. Zhou and W. Xu, "LuBan: Low-Cost and In-Situ Droplet Micro-Sensing for Inkjet 3D Printing Quality Assurance," in *SenSys'17*, Delft, The Netherlands, 2017.

[41] T. Chang, O. Mays, S. Mukherjee, N. Watkins, A. Pascall, J. Jeffries and J. Tringe, "An in-situ millimeter-wave diagnostic for droplet characterization during jetting-based additive manufacturing processes," in *SPIE 11380, Nondestructive Characterization and Monitoring of Advanced Materials, Aerospace, Civil Infrastructure, and Transportation XIV*, 2020.

[42] T. Chang, S. Mukherjee, N. N. Watkins, D. M. Stobbe, O. Mays, E. V. Baluyot, A. J. Pascall and J. W. Tringe, "In-situ monitoring for liquid metal jetting using a millimeter-wave impedance diagnostic," *Nature Scientific Reports*, vol. 10 (22325), 2020.

[43] L. Scime, J. Haley, W. Halsey, A. Singh, M. Sprayberry, A. Ziabari, V. Paquit, Development of Monitoring Techniques for Binderjet Additive Manufacturing of Silicon Carbide Structures, Oak Ridge, Tennessee, 2020.

[44] N. D. Parab, J. E. Barnes, C. Zhao, R. W. Cunningham, K. Fezzaa, A. D. Rollett and T. Sun, "Real time observation of binder jetting printing process using high-speed X-ray imaging," *Nature Scientific Reports* , vol. 9, 2019.

[45] V. Dikshit, A. P. Nagalingam, Y. L. Yap, S. L. Sing, W. Y. Yeong and J. Wei, "Investigation of Quasi-Static Indentation Response of Inkjet Printed Sandwich Structures under Various Indenter Geometries," *Materials*, vol. 10, 2017.

[46] V. Dikshit, A.P. Nagalingam, Y.L. Yap, S.L. Sing, W.Y. Yeong, J. Wei, Crack monitoring and failure investigation on inkjet printed sandwich structures under quasi-static identation test, Mater. Des. 137 (2018) 140–151.

[47] B. Lies, "In-situ metrology for electrohydrodynamic inkjet printing towards micro/nano scale hybrid manufacturing," 2019.

[48] D. Hu, R. Kovacevic, Sensing, modeling and control for laser-based additive manufacturing, Int. J. Mach. Tools Manuf 43 (2003) 51–60.

[49] Y. Ding, J. Warton, R. Kovacevic, Development of sensing and control system for robotized laser-based direct metal addition system, Addit. Manuf. 10 (2016) 24–35.

[50] R. Jendrzejewski, I. Kreja, G. Sliwinski, Temperature distribution in laser-clad multi-layers, Mater. Sci. Eng., A 379 (2004) 313–320.

[51] M. Doubenskaia, P. Bertrand, I. Smurov, Pyrometry in laser surface treatment, Surf. Coat. Technol. 201 (2006) 1955–1961.

[52] J. Yu, X. Lin, J. Wang, J. Chen, W. Huang, Mechanics and energy analysis on molten pool spreading during laser solid forming, Appl. Surf. Sci. 256 (2010) 4612–4620.

[53] G. Bi, C. Sun, A. Gasser, Study of influential factors for process monitoring and control in laser aided additive manufacturing, J. Mater. Process. Technol. 213 (2013) 463–468.

[54] H. Kohler, V. Jayaraman, D. Brosch, F. Hutter, T. Seefeld, A novel thermal sensor applied for laser materials processing, Physics Procedia 41 (2013) 502–508.

[55] F. Meriaudeau, F. Truchetet, D. Grevey, A. Vannes, Laser cladding process and image processing, Lasers in Engineering 6 (3) (1997) 161–187.

[56] G. Bi, A. Gasser, K. Wissenbach, A. Drenker, R. Poprawe, Identification and qualification of temperature signal for monitoring and control in laser cladding, Opt. Lasers Eng. 44 (2006) 1348–1359.

[57] L. Wang, S. D. Felicelli and J. E. Craig, "Thermal Modeling and Experimental Validation in the LENS Process," in *18th International Solid Freeform Fabrication Symposium*, Austin, TX, 2007.

[58] L. Song, V. Bagavath-Singh, B. Dutta, J. Mazumder, Control of melt pool temperature and deposition height during direct metal deposition process, Int. J. Adv. Manuf. Technol. 58 (2012) 247–256.

[59] M. Pavlov, D. Novichenko, M. Doubenskaia, Optical Diagnostics of Deposition of Metal Matrix Composites by Laser Cladding, Physics Procedia 12 (2011) 674–682.

[60] I. Smurov, M. Doubenskaia, S. Grigoriev, A. Nazarov, Optical Monitoring in Laser Cladding of Ti6Al4V, J. Therm. Spray Technol. 21 (2012) 1357–1362.

[61] I. Smurov, M. Doubenskaia, A. Zaitsev, Comprehensive analysis of laser cladding by means of optical diagnostics and numerical simulation, Surf. Coat. Technol. 220 (2013) 112–121.

[62] T. Hua, C. Jing, L. Xin, Z. Fengying, H. Weidong, Research on molten pool temperature in the process of laser rapid forming, J. Mater. Process. Technol. 198 (2008) 454–462.

[63] S. Karnati, N. Matta, T. Sparks and F. Liou, "Vision-based Process Monitoring for Laser Metal Deposition Processes," in *24th International Solid Freeform Fabrication Symposium*, Austin, TX, 2013.

[64] M. Doubenskaia, M. Pavlov, S. Grigoriev, I. Smurov, Definition of brightness temperature and restoration of true temperature in laser cladding using infrared camera, Surf. Coat. Technol. 220 (2013) 244–247.

[65] U. Hassler, D. Gruber, O. Hentschel, F. Sukowski, T. Grulich, L. Seifert, In-situ monitoring and defect detection for laser metal deposition by using infrared thermography, Physics Procedia 83 (2016) 1244–1252.

[66] M. Mazzarisi, S.L. Campanelli, A. Angelastro, F. Palano, M. Dassisti, In situ monitoring of direct laser metal deposition of a nickel-based superalloy using infrared thermography, The International Journal of Advanced Manufacturing Technology 112 (2021) 157–173.

[67] S. Barua, T. Sparks and F. Liou, "Development of low-cost imaging system for LMD processes," *Rapid Prototyping Journal*, Vols. 17 (011010-1), no. 3, pp. 203-210, 2011.

[68] S. Barua, F. Liou, J. Newkirk, T. Sparks, Vision-based defect detection in laser metal deposition process, Rapid Prototyping Journal 20 (1) (2014) 77–86.

[69] L. Tang and R. G. Landers, "Melt Pool Temperature Modeling and Control for Laser Metal Deposition Processes," *Journal of Manufacturing Science and Engineering*, vol. 132, no. 1, 2010.

[70] A.R. Nassar, J.S. Keist, E.W. Reutzel, T.J. Spurgeon, Intra-layer closed-loop control of build plan during directed energy additive manufacturing of Ti-6Al-4V, Addit. Manuf. 6 (2015) 39–52.

[71] D.A. Kriczky, J. Irwin, E.W. Reutzel, P. Michaleris, A.R. Nassar, J. Craig, 3D spatial reconstruction of thermal characteristics in directed energy deposition through optical thermal imaging, J. Mater. Process. Technol. 221 (2015) 172–186.

[72] L. Aucott, H. Dong, W. Mirihanage, R. Atwood, A. Kidess, S. Gao, S. Wen, J. Marsden, S. Feng, M. Tong, T. Connolley, M. Drakopoulos, C. R. Kleijn, I. M. Richardson, D. J. Browne, R. H. Mathiesen and H. V. Atkinson, ''Revealing internal flow behaviour in arc welding and additive manufacturing of metals,'' *Nature Communications,* vol. 9 (5414), 2018.

[73] C.L.A. Leung, S. Marussi, R.C. Atwood, M. Towrie, P.J. Withers, P.D. Lee, ''In situ X-ray imaging of defect and molten pool dynamics in laser additive manufacturing, Nat. Commun. 9 (2018) 1355.

[74] S. J. Wolff, H. Wu, N. Parab, C. Zhao, K. F. Ehmann, T. Sun and J. Cao, ''In-situ high-speed X-ray imaging of piezo-driven directed energy deposition additive manufacturing,'' *Scientific Reports* , vol. 9, 2019.

[75] S. J. Wolff, S. Webster, N. D. Parab, B. Aronson, B. Gould, A. Greco and T. Sun, ''In-situ Observations of Directed Energy Deposition Additive Manufacturing Using High-Speed X-ray Imaging,'' *JOM,* vol. 73, no. 1 (962), pp. 189-200, 2021.

[76] A. Medrano, J. Folkes, J. Segal and I. Pashby, ''Fibre laser metal deposition with wire: parameters study and temperature monitoring system,'' in *SPIE 7131, XVII International Symposium on Gas Flow, Chemical Lasers, and High-Power Lasers*, 2009.

[77] J. N. Zalameda, E. R. Burke, R. A. Hafley, K. M. Taminger, C. S. Domack, A. Brewer and R. E. Martin, ''Thermal imaging for assessment of electron-beam freeform fabrication (EBF3) additive manufacturing deposits,'' in *SPIE 8705, Thermosense: Thermal Infrared Applications XXXV*, 2013.

[78] S. Liu, W. Liu, M. Harooni, J. Ma, R. Kovacevic, Real-time monitoring of laser hot-wire cladding of Inconel 625, Opt. Laser Technol. 62 (2014) 124–134.

[79] W. Liu, S. Liu, J. Ma, R. Kovacevic, Real-time monitoring of the laser hot-wire welding process, Opt. Laser Technol. 57 (2014) 66–76.

[80] F. Wang, H. Mao, D. Zhang, X. Zhao, Y. Shen, Online study of cracks during laser cladding process based on acoustic emissiontechnique and finite element analysis, Appl. Surf. Sci. 255 (2008) 3267–3275.

[81] L. W. Koester, H. Taheri, T. A. Bigelow, L. J. Bond and E. J. Faierson, ''In-situ Acoustic Signature Monitoring in Additive Manufacturing Processes,'' in *AIP Conference Proceedings 1949 (020006)*, 2018.

[82] L. W. Koester, H. Taheri, L. J. Bond and E. J. Faierson, ''Acoustic monitoring of additive manufacturing for damage and process condition determination,'' in *AIP Conference Proceedings 2102 (020005)*, 2019.

[83] H. Taheri, Nondestructive evaluation and in-situ monitoring for metal additive manufacturing, Ames, Iowa, USA, 2018.

[84] H. Taheri, L.W. Koester, T.A. Bigelow, E.J. Faierson, L.J. Bond, In Situ Additive Manufacturing Process Monitoring With an Acoustic Technique: Clustering Performance Evaluation Using K-Means Algorithm, J. Manuf. Sci. Eng. 141 (2019) 041011–41021.

[85] L. Song, J. Mazumder, Real Time Cr Measurement Using Optical Emission Spectroscopy During Direct Metal Deposition Process, IEEE Sens. J. 12 (5) (2012) 958–964.

[86] A. R. Nassar, T. J. Spurgeon and E. W. Reutzel, ''Sensing defects during directed-energy additive manufacturing of metal parts using optical emissions spectroscopy,'' in *25th International Solid Freeform Fabrication Symposium*, Austin, TX, 2014.

[87] J. Whiting, A. Springer, F. Sciammarella, Real-time acoustic emission monitoring of powder mass flow rate for directed energy deposition, Addit. Manuf. 23 (2018) 312–318.

[88] L. Bond, L. Koester and H. Taheri, ''NDE in-process for metal parts fabricated using powder based additive manufacturing,'' in *SPIE 10973, Smart Structures and NDE for Energy Systems and Industry 4.0*, Denver, Colorado, US, 2019.

[89] A. Heralic, A.-K. Christiansson, B. Lennartson, Height control of laser metal-wire deposition based on iterative learning control and 3D scanning, Opt. Lasers Eng. 50 (2012) 1230–1241.

[90] H. Gaja, F. Liou, Defects monitoring of laser metal deposition using acoustic emission sensor, Int. J. Adv. Manuf. Technol. 90 (2017) 561–574.

[91] A. Ramalho, T. G. Santos, B. Bevans, Z. Smoqi, P. Rao and J. Oliveira, ''Effect of contaminations on the acoustic emissions during wire and arc additive manufacturing of 316L stainless steel,'' *Additive Manufacturing,* vol. 51 (102585), 2022.

[92] M.I. Albakri, L.D. Sturm, C.B. Williams, P.A. Tarazaga, Impedance-based non-destructive evaluation of additively manufactured parts, Rapid Prototyping Journal 23 (3) (2017) 589–601.

[93] L.D. Sturm, M.I. Albakri, P.A. Tarazaga, C.B. Williams, In situ monitoring of material jetting additive manufacturing process via impedance based measurements, Addit. Manuf. 28 (2019) 456–463.

[94] Y. Cheng, M.A. Jafari, Vision-Based Online Process Control in Manufacturing Applications, IEEE Trans. Autom. Sci. Eng. 5 (1) (2008) 140–153.

[95] M. Faes, F. Vogeler, K. Coppens, H. Valkenaers, E. Ferraris, W. Abbeloos and T. Goedeme, ''Process monitoring of Extrusion Based 3D Printing via Laser Scanning,'' in *International Conference on Polymers and Moulds Innovations*, Guimaraes, Portugal, 2014.

[96] K. Pooladvand, A.D. Salerni, C. Furlong, ''In-situ Thermal Monitoring of Printed Components During Rapid Prototyping by Fused Deposition Modeling, Residual Stress Thermomechanics & Infrared Imaging and Inverse Problems 6 (2020) 131–140.

[97] Z. Yang, L. Jin, Y. Yan and Y. Mei, ''Filament Breakage Monitoring in Fused Deposition Modeling Using Acoustic Emission Technique,'' *Sensors,* vol. 18, no. x, 2018.

[98] Z. Yang, W. Yan, L. Jin, F. Li and Z. Hou, ''A novel feature representation method based on original waveforms for acoustic emission signals,'' *Mechanical Systems and Signal Processing,* vol. 135 (106365), 2020.

[99] H. Wu, Y. Wang, Z. Yu, In situ monitoring of FDM machine condition via acoustic emission, Int. J. Adv. Manuf. Technol. 84 (2016) 1483–1495.

[100] H. Wu, Z. Yu and Y. Wang, ''A New Approach for Online Monitoring of Additive Manufacturing Based on Acoustic Emission,'' in *Proceedings of the ASME 2016 Manufacturing Science and Engineering Conference*, Virginia, USA, 2016.

[101] J.S. Kim, C.S. Lee, S.-M. Kim, S.W. Lee, Development of Data-Driven In-Situ Monitoring and Diagnosis System of Fused Deposition Modeling (FDM) Process Based on Support Vector Machine Algorith, International Journal of Precision Engineering and Manufacturing-green Technology 5 (4) (2018) 479–486.

[102] H. Wu, Z. Yu, Y. Wang, Experimental study of the process failure diagnosis in additive manufacturing based on acoustic emission, Measurement 136 (2019) 445–453.

[103] G. L. Chen and N. Gupta, ''Image processing and machine learning methods applied to additive manufactured composites for defect detection and toolpath reconstruction,'' Brooklyn, NY, 2021.

[104] I. Cummings, E. Hillstrom, R. Newton, E. Flynn and A. Wachtor, ''In-process Ultrasonic Inspection of Additive Manufactured Parts,'' in *Topics in Modal Analysis & Testing, Volume 10, Chapter 20*, 2016.

[105] I. T. Cummings, M. Bax, I. J. Fuller, A. J. Wachtor and J. D. Bernardin, ''A Framework for Additive Manufacturing Process Monitoring and Control,'' in *Topics in Modal Analysis & Testing*, vol. 10, 2017, pp. 137-146.

[106] E. C. Koskelo and E. B. Flynn, ''Scanning laser ultrasound and wavenumber spectroscopy for in-process inspection of additively manufactured parts,'' in *SPIE 9804 Nondestructive Characterization and Monitoring of Advanced Materials, Aerospace, and Civil Infrastructure*, Las Vegas, Nevada, USA, 2016.

[107] F. Li, Z. Yu, Z. Yang, X. Shen, Real-time distortion monitoring during fused deposition modeling via acoustic emission, Structural Health Monitoring 19 (2) (2020) 412–423.

[108] Z. Jin, Z. Zhang and G. X. Gu, ''Automated Real-Time Detection and Prediction of Interlayer Imperfections in Additive Manufacturing Processes Using Artifical Intelligence,'' *Advanced Intelligent Systems,* vol. 2 (1900130), 2020.

[109] Z. Jin, Z. Zhang, G.X. Gu, Autonomous in-situ correction of fused deposition modeling printers using computer vision and deep learning, Manufacturing Letters 22 (2019) 11–15.

[110] K. He, Q. Zhang, Y. Hong, Profile monitoring based quality control method for fused deposition modeling process, J. Intell. Manuf. 30 (2019) 947–958.

[111] C. Kousiatza, D. Karalekas, In-situ monitoring of strain and temperature distributions during fused deposition modeling process, Mater. Des. 97 (2016) 400–406.

[112] J.A. Slotwinski, E.J. Garboczi, Metrology Needs for Metal Additive Manufacturing Powders, JOM 67 (3) (2015) 538–543.

[113] H.D. Vora, S. Sanyal, A comprehensive review: metrology in additive manufacturing and 3D printing technology, Progress in Additive Manufacturing 5 (2020) 319–353.

[114] J.L. Bartlett, X. Li, An overview of residual stresses in metal powder bed fusion, Addit. Manuf. 27 (2019) 131–149.

[115] L.E. Criales, Y.M. Arisoy, B. Lane, S. Moylan, A. Donmez, T. Ozel, Predictive modeling and optimization of multi-track processing for laser powder bed fusion of nickel alloy 625, Addit. Manuf. 13 (2017) 14–36.

[116] L. Yang, L. Lo, S. Ding, T. Ozel, Monitoring and detection of meltpool and spatter regions in laser powder bed fusion of super alloy Inconel 625, Progress in Additive Manufacturing 6 (2020) 367–378.

[117] V. Pandiyan, R. Drissi-Daoudi, S. Shevchik, G. Masinelli, R. Loge, K. Wasmer, Analysis of time, frequency and time-frequency domain features from acoustic emissions during Laser Powder-Bed fusion process, Procedia CIRP 94 (2020) 392–397.

[118] M.F. Zaeh, G. Branner, Investigations on residual stresses and deformations in selective laser melting, Prod. Eng. Res. Devel. 4 (2010) 35–45.

[119] Y. Chen, X. Peng, L. Kong, G. Dong, A. Remani and R. Leach, ''Defect inspection technologies for additive manufacturing,'' *Int. J. Extrem. Manuf.,* vol. 3 (022002), 2021.

[120] I. Gibson, D. Rosen, B. Stucker, Additive Manufacturing Technologies, 2 ed.,., Springer Science, 2015.

[121] C. Liu, A.C.C. Law, D. Roberson, Z. Kong, Image analysis-based closed loop quality control for additive manufacturing with fused filament fabrication, J. Manuf. Syst. 51 (2019) 75–86.

[122] A.-D. Mazurchevici, R.-I. Popa, C. Carausu, S.-N. Mazurchevici and D. Nedelcu, ''Influence of Layer Thickness, Infill Rate and Orientation on Thermal and Structural Loading of FDM Parts,'' in *Advances in Manufacturing Processes* , Springer Nature Singapore Pte Ltd., 2021, pp. 263-282.

[123] F. Bayle and M. Doubenskaia, ''Selective Laser Melting process monitoring with high speed infra-red camera and pyrometer,'' in *SPIE - The International Society for Optical Engineering* , Saint-Etienne, 2008.

[124] Y. Chivel, I. Smurov, On-line temperature monitoring in selective laser sintering/melting, Physics Procedia 5 (2010) 515–521.

[125] M. Doubenskaia, M. Pavlov, Y. Chivel, Optical System for On-Line Monitoring and Temperature Control in Selective Laser Melting Technology, Key Eng. Mater. 437 (2010) 458–461.

[126] M. Doubenskaia, M. Pavlov, S. Grigoriev, E. Tikhonova, I. Smurov, Comprehensive Optical Monitoring of Selective Laser Melting, J. Laser Micro/Nanoeng. 7 (3) (2012) 236–243.

[127] U. Thombansen, A. Gatej, M. Pereira, Process observation in fiber laser-based selective laser melting, Opt. Eng. 54 (1) (2015) 011008–11011.

[128] B. Foster, E. Reutzel, A. Nassar, B. Hall, S. Brown and C. Dickman, "Optical layerwise monitoring of powder bed fusion," in *Solid Freeform Symposium Proceedings*, Pennsylvania, USA, 2015.

[129] S. Berumen, F. Bechmann, S. Lindner, J.-P. Kruth, T. Craeghs, Quality control of laser- and powder bed-based Additive Manufacturing (AM) technologies, Physics Procedia 5 (2010) 617–622.

[130] T. Craeghs, S. Clijsters, E. Yasa, F. Bechmann, S. Berumen, Determination of geometrical factors in Layerwise Laser Melting using optical process monitoring, Opt. Lasers Eng. 49 (2011) 1440–1446.

[131] S. Clijsters, T. Craeghs, S. Buls, K. Kempen, In situ quality control of the selective laser melting process using a high-speed, real-time melt pool monitoring system, Int. J. Adv. Manuf. Technol. 75 (2014) 1089–1101.

[132] M. Rombouts, J. Kruth, L. Froyen, P. Mercelis, Fundamentals of selective laser melting of alloyed steel powders, CIRP Annals - Manufacturing Technology 55 (2006) 187–192.

[133] C. Van Gestel, "Study of physical phenomena of selective laser melting towards increased productivity," Switzerland, 2015.

[134] Y. Chivel, I. Smurov, Temperature Monitoring and Overhang Layers Problem, Physics Procedia 12 (2011) 691–696.

[135] T. Craeghs, S. Clijsters, E. Yasa, J.-P. Kruth, Online Quality Control of Selective Laser Melting, Heverlee, Belgium, 2011.

[136] T. Craeghs, S. Clijsters, J.-P. Kruth, F. Bechmann, M.-C. Ebert, Detection of process failures in Layerwise Laser Melting with optical process monitoring, Physics Procedia 39 (2012) 753–759.

[137] S. Kleszczynski, J. zur Jacobsmuhlen, J. T. Sehrt and G. Witt, "Error Detection in Laser Beam Melting Systems by High Resolution Imaging," in *Twenty Third Annual International Solid Freeform Fabrication Symposium* , Aachen, 2012.

[138] I. Yadroitsev, P. Krakhmalev, I. Yadroitsava, Selective laser melting of Ti6Al4V alloy for biomedical applications: Temperature monitoring and microstructural evolution, J. Alloy. Compd. 583 (2014) 404–409.

[139] W.S. Land II, B. Zhang, J. Ziegert, A. Davies, In-Situ Metrology System for Laser Powder Bed Fusion Additive Process, Procedia Manuf. 1 (2015) 393–403.

[140] L. Scime, J. Beuth, Anomaly detection and classification in a laser powder bed additive manufacturing process using a trained computer vision algorithm, Addit. Manuf. 19 (2018) 114–126.

[141] L. Scime, J. Beuth, Using machine learning to identify in-situ melt pool signatures indicative of flaw formation in a laser powder bed fusion additive manufacturing process, Addit. Manuf. 25 (2019) 151–165.

[142] L. Pagani, M. Grasso, P. J. Scott and B. M. Colosimo, "Automated layerwise detection of geometrical distortions in laser powder bed fusion," *Additive Manufacturing,* vol. 36 (101435), 2020.

[143] B. Shi and Z. Chen, "A layer-wise multi-defect detection system for powder bed monitoring: Lighting strategy for imaging, adaptive segmentation and classification," *Materials & Design,* vol. 210 (110035), 2021.

[144] G.A. Demir, C. De Giorgi, B. Previtali, Design and Implementation of a Multisensor Coaxial Monitoring System With Correction Strategies for Selective Laser Melting of a Maraging Steel, J. Manuf. Sci. Eng. 140 (2018) 041003–41011.

[145] A. Wegner and G. Witt, "Process monitoring in laser sintering using thermal imaging," in *Solid Freeform Fabrication Symposium*, Austin, Texas, USA, 2011.

[146] Y. Chivel, Optical in-process temperature monitoring of selective laser melting, Physics Procedia 41 (2013) 904–910.

[147] M. Islam, T. Purtonen, H. Piili, A. Salminen, O. Nyrhila, Temperature profile and imaging analysis of laser additive manufacturing of stainless steel, Physics Procedia 41 (2013) 835–842.

[148] S. Kolossov, E. Boillat, R. Glardon, P. Fischer, M. Locher, 3D FE simulation for temperature evolution in the selective laser sintering process, Int. J. Mach. Tools Manuf 44 (2004) 117–123.

[149] S. Dadbakhsh, L. Hao, N. Sewell, Effect of selective laser melting layout on the quality of stainless steel parts, Rapid Prototyping Journal 18 (3) (2012) 241–249.

[150] H. Krauss, C. Eschey and M. F. Zaeh, "Thermography for Monitoring the Selective Laser Melting Process," in *Solid Freeform Fabrication Symposium*, Muenchen, Germany, 2012.

[151] H. Krauss, T. Zeugner, M.F. Zaeh, Layerwise Monitoring of the Selective Laser Melting Process by Thermography, Physics Procedia 56 (2014) 64–71.

[152] J. Schilp, C. Seidel, H. Krauss and J. Weirather, "Investigations on Temperature Fields during Laser Beam Melting by Means of Process Monitoring and Multiscale Process Modeling," *Advances in Mechanical Engineering,* vol. (217584), 2014.

[153] H. Krauss, T. Zeugner and M. F. Zaeh, "Thermographic Process Monitoring in Powderbed Based Additive Manufacturing," in *AIP Conference Proceedings 1650 (No. 1)*, 2015.

[154] B. Lane, S. Moylan, E. Whitenton, L. Ma, Thermographic Measurements of the Commercial Laser Powder Bed Fusion Process at NIST, Rapid Prototyping Journal 22 (5) (2016) 778–787.

[155] M. Grasso, A. Demir, B. Previtali, B. Colosimo, In situ monitoring of selective laser melting of zinc powder via infrared imaging of the process plume, Rob. Comput. Integr. Manuf. 49 (2018) 229–239.

[156] A. J. Dunbar, "Analysis of the Laser Powder Bed Fusion Additive Manufacturing Process Through Experimental Measurement and Finite Element Modeling," 2016.

[157] N. Schnell, M. Schoeler, G. Witt and S. Kleszczynski, "Experimental and numerical thermal analysis of the laser powder bed fusion process using in situ temperature measurements of geometric primitives," *Materials & Design,* vol. 209 (109946), 2021.

[158] J. zur Jacobsmuhlen, S. Kleszczynski, D. Schneider and G. Witt, "High Resolution Imaging for Inspection of Laser Beam Melting Systems," in *IEEE Instrumentation and Measurement Technology Conference*, Aachen, 2013.

[159] J. zur Jacobsmuhlen, S. Kleszczynski, G. Witt and D. Merhof, "Detection of Elevated Regions in Surface Images from Laser Beam Melting Processes," in *26th International Solid Free Form Fabrication (SFF) Symposium*, Aachen, 2015.

[160] J. A. Mitchell, T. A. Ivanoff, D. Dagel, J. D. Madison and B. Jared, "Linking pyrometry to porosity in additively manufactured metals," *Additive Manufacturing,* vol. 31 (100946), 2020.

[161] J.-B. Forien, N. P. Calta, P. J. DePond, G. M. Guss, T. T. Roehling and M. J. Matthews, "Detecting keyhole pore defects and monitoring process signatures during laser powder bed fusion: A correlation between in situ pyrometry and ex situ X-ray radiography," *Additive Manufacturing,* vol. 35 (101336), 2020.

[162] Y. Plotnikov, D. Henkel, J. Burdick, A. French, J. Sions and K. Bourne, "Infrared-assisted acoustic emission process monitoring for additive manufacturing," in *AIP Conference Proceedings 2102 (020006)*, 2019.

[163] J. Yin, L. Yang, X. Yang, H. Zhu, D. Wang, L. Ke, Z. Wang, G. Wang and X. Zeng, "High-power laser-matter interaction during laser powder bed fusion," *Additive Manufacturing,* vol. 29 (100778), 2019.

[164] J. Yin, D. Wang, L. Yang, H. Wei, P. Dong, L. Ke, G. Wang, H. Zhu and X. Zeng, "Correlation between forming quality and spatter dynamics in laser powder bed fusion," *Additive Manufacturing,* vol. 31 (100958), 2020.

[165] W.E. King, H.D. Barth, V.M. Castillo, G.F. Gallegos, J.W. Gibbs, D.E. Hahn, C. Kamath, A.M. Rubenchik, Observation of keyhole-mode laser melting in laser powder-bed fusion additive manufacturing, J. Mater. Process. Technol. 214 (2014) 2915–2925.

[166] G. Repossini, V. Laguzza, M. Grasso, B.M. Colosimo, On the use of spatter signature for in-situ monitoring of Laser Powder Bed Fusion, Addit. Manuf. 16 (2017) 35–48.

[167] J. Trapp, A.M. Rubenchik, G. Guss, M.J. Matthews, In situ absorptivity measurements of metallic powders during laser powder-bed fusion additive manufacturing, Appl. Mater. Today 9 (2017) 341–349.

[168] D. Wang, G. Ye, W. Dou, M. Zhang, Y. Yang, S. Mai and Y. Liu, "Influence of spatter particles contamination on densification behavior and tensile properties of CoCrW manufactured by selective laser melting," *Optical and Laser Technology,* vol. 121 (105678), 2020.

[169] L.E. Criales, Y.M. Arisoy, B. Lane, S. Moylan, A. Donmez, T. Ozel, Laser powder bed fusion of nickel alloy 625: Experimental investigations of effects of process parameters on melt pool size and shape with spatter analysis, Int. J. Mach. Tools Manuf 121 (2017) 22–36.

[170] F. Bai, D. Gagar, P. Foote, Y. Zhao, Comparison of alternatives to amplitude thresholding for onset detection of acoustic emission signals, Mech. Syst. Sig. Process. 84 (2017) 717–730.

[171] H. Zheng, H. Li, L. Lang, S. Gong, Y. Ge, Effects of scan speed on vapor plume behavior and spatter generation in laser powder bed fusion additive manufacturing, J. Manuf. Processes 36 (2018) 60–67.

[172] A. Gaikwad, B. Giera, G. M. Guss, J.-B. Forien, M. J. Matthews and P. Rao, "Heterogeneous sensing and scientific machine learning for quality assurance in laser powder bed fusion - A single-track study," *Additive Manufacturing,* vol. 36 (101659), 2020.

[173] B. Zhang, J. Ziegert, F. Farahi, A. Davies, In situ surface topography of laser powder bed fusion using fringe projection, Addit. Manuf. 12 (2016) 100–107.

[174] C. Zhao, K. Fezzaa, R. W. Cunningham, H. Wen, F. De Carlo, L. Chen, A. D. Rollett and T. Sun, "Real-time monitoring of laser powder bed fusion process using high-speed X-ray imaging and diffraction," *Scientific Reports,* vol. 7 (3602), 2017.

[175] N. P. Calta, J. Wang, A. M. Kiss, A. A. Martin, P. J. Depond, G. M. Guss, V. Thampy, A. Y. Fong, J. N. Weker, K. H. Stone, C. J. Tassone, M. J. Kramer, M. F. Toney, A. Van Buuren and M. J. Matthews, "An instrument for in situ time-resolved X-ray imaging and diffraction of laser powder bed fusion additive manufacturing processes," *Review of Scientific Instruments,* vol. 89 (055101), 2018.

[176] Q. Guo, C. Zhao, L.I. Escano, Z. Young, L. Xiong, K. Fezzaa, W. Everhart, B. Brown, T. Sun, L. Chen, Transient dynamics of powder spattering in laser powder bed fusion additive manufacturing process revealed by in-situ high-speed high-energy x-ray imaging, Acta Mater. 151 (2018) 169–180.

[177] Q. Guo, C. Zhao, M. Qu, L. Xiong, L.I. Escano, S.M.H. Hojjatzadeh, N.D. Parab, K. Fezzaa, W. Everhart, T. Sun, L. Chen, In-situ characterization and quantification of melt pool variation under constant input energy density in laser powder bed fusion additive manufacturing process, Addit. Manuf. 28 (2019) 600–609.

[178] Q. Guo, C. Zhao, M. Qu, L. Xiong, S. M. H. Hojjatzadeh, L. I. Escano, N. D. Parab, K. Fezzaa, T. Sun and L. Chen, "In-situ full-field mapping of melt flow dynamics in laser metal additive manufacturing," *Additive Manufacturing,* vol. 31 (100939), 2020.

[179] N.D. Parab, C. Zhao, R. Cunningham, L.I. Escano, K. Fezzaa, W. Everhart, A.D. Rollett, L. Chen, T. Sun, Ultrafast X-ray imaging of laser-metal additive manufacturing processes, Journal of Synchrotron Radiation 25 (2499) (2018) 1467–1477.

[180] S. M. H. Hojjatzadeh, N. D. Parab, W. Yan, Q. Guo, L. Xiong, C. Zhao, M. Qu, L. I. Escano, X. Xiao, K. Fezzaa, W. Everhart, T. Sun and L. Chen, "Pore elimination mechanisms during 3D printing of metals," *Nature Communications,* vol. 10 (3088), 2019.

[181] J. L. McNeil, K. Sisco, C. Frederick, M. Massey, K. Carver, F. List III, C. Qui, M. Mader, S. Sundarraj and S. Babu, "In-Situ Monitoring for Defect Identification

in Nickel Alloy Complex Geometries Fabricated by L-PBF Additive Manufacturing," *Metallurgical and Materials Transactions A,* October 2020.

[182] G. Mohr, S. J. Altenburg, A. Ulbricht, P. Heinrich, D. Baum, C. Maierhofer and K. Hilgenberg, "In-Situ Defect Detection in Laser Powder Bed Fusion by Using Thermography and Optical Tomography—Comparison to Computed Tomography," *Metals,* vol. 10 (103), no. 1, 2020.

[183] N. Eschner, L. Weiser, B. Hafner and G. Lanza, "Classification of specimen density in Laser Powder Bed Fusion (L-PBF) using in-process structure-borne acoustic process emissions," *Additive Manufacturing,* vol. 34 (101324), 2020.

[184] N. Eschner, L. Weiser, B. Hafner and G. Lanza, "Development of an acoustic process monitoring system for selective laser melting (SLM)," in *Solid Freeform Fabrication 2018: Proceedings of the 29th Annual International Solid Freeform Fabrication Symposium*, 2018.

[185] M.G. Mohammadi, M. Elbestawi, Real Time Monitoring in L-PBF Using a Machine Learning Approach, Procedia Manuf. 51 (2020) 725–731.

[186] K. Ito, M. Kusano, M. Demura and M. Watanebe, "Detection and location of microdefects during selective laser melting by wireless acoustic emission measurement," *Additive Manufacturing,* vol. 40 (101915), 2021.

[187] H. Rieder, A. Dillhofer, M. Spies, J. Bamberg and T. Hess, "Ultrasonic online monitoring of additive manufacturing processes based on selective laser melting," in *AIP Conference Proceedings 1650 (184)*, 2015.

[188] K.A. Fisher, J.V. Candy, G. Guss, M. Mathews, Evaluating Acoustic Emission Signals as an in situ process monitoring technique for Selective Laser Melting (SLM), DOE, Livermore, CA, USA, 2016.

[189] S. Shevchik, C. Kenel, C. Leinenbach, K. Wasmer, Acoustic emission for in situ quality monitoring in additive manufacturing using spectral convolutional neural networks, Addit. Manuf. 21 (2018) 598–604.

[190] S.A. Shevchik, G. Masinelli, C. Kenel, C. Leinenbach, K. Wasmer, Deep Learning for In Situ and Real-Time Quality Monitoring in Additive Manufacturing Using Acoustic Emission, IEEE 15 (9) (2019) 5194–5203.

[191] D. Kouprianoff, N. Luwes, I. Yadroitsava and I. Yadroitsev, "Acoustic emission technique for online detection of fusion defects for single tracks during metal laser powder bed fusion," in *Solid Freeform Fabrication 2018: Proceedings of the 29th Annual International Solid Freeform Fabrication Symposium* , Bloemfontein, South Africa, 2018.

[192] D. Ye, G.S. Hong, Y. Zhang, K. Zhu, J.Y.H. Fuh, Defect detection in selective laser melting technology by acoustic signals with deep belief networks, The International Journals of Advanced Manufacturing Technology 96 (2018) 2791–2801.

[193] V. Pandiyan, R. Drissi-Daoudi, S. Shevchik, G. Masinelli, T. Le-Quang, R. Loge, K. Wasmer, Semi-supervised Monitoring of Laser powder bed fusion process based on acoustic emissions, Virtual and Physical Prototyping 16 (4) (2021) 481–497.

[194] R. Drissi-Daoudi, V. Pandiyan, R. Loge, S. Shevchik, G. Masinelli, H. Ghasemi-Tabasi, A. Parrilli, K. Wasmer, Differentiation of materials and laser powder bed fusion processing regimes from airborne acoustic emission combined with machine learning, Virtual and Physical Prototyping 17 (2) (2022) 181–204.

[195] D. Kouprianoff, I. Yadroitsava, A. du Plessis, N. Luwes and I. Yadroitsev, "Monitoring of Laser Powder Bed Fusion by Acoustic Emission: Investigation of Single Tracks and Layers," *Frontiers in Mechanical Engineering,* vol. 7 (678076), 2021.

[196] D. S. Ye, Y. H. J. Fuh, Y. J. Zhang, G. S. Hong and K. P. Zhu, "Defects Recognition in Selective Laser Melting with Acoustic Signals by SVM Based on Feature Reduction," in *IOP Conf. Series: Materials Science and Engineering*, 2018.

[197] K. Wasmer, T. Le-Quang, B. Meylan, F. Vakili-Farahani, M. Olbinado, A. Rack, S. Shevchik, Laser process quality monitoring by combining acoustic emission and machine learning: a high-speed X-ray imaging approach, Procedia CIRP 74 (2018) 654–658.

[198] A. Neef, V. Seyda, D. Herzog, C. Emmelmann, M. Schonleber, M. Kogel-Hollacher, Low coherence interferometry in selective laser melting, Physics Procedia 56 (2014) 82–89.

[199] J.A. Kanko, A.P. Sibley, J.M. Fraser, In situ morphology-based defect detection of selective laser melting through inline coherent imaging, J. Mater. Process. Technol. 231 (2016) 488–500.

[200] T. G. Fleming, S. G. Nestor, T. R. Allen, M. A. Boukhaled, N. J. Smith and J. M. Fraser, "Tracking and controlling the morphology evolution of 3D powder-bed fusion in situ using inline coherent imaging," *Additive Manufacturing,* vol. 32 (100978), 2020.

[201] K. Gutknecht, M. Cloots, R. Sommerhuber and K. Wegener, "Mutual comparison of acoustic, pyrometric and thermographic laser powder bed fusion monitoring," *Materials & Design,* vol. 210 (110036), 2021.

[202] J. Schwerdtfeger, R.F. Singer, C. Korner, In situ flaw detection by IR-imaging during electron beam melting, Rapid Prototyping Journal 18 (4) (2012) 259–263.

[203] R. B. Dinwiddie, R. R. Dehoff, P. D. Lloyd, L. E. Lowe and J. B. Ulrich, "Thermographic In-Situ Process Monitoring of the Electron Beam Melting Technology used in Additive Manufacturing," in *SPIE Defense, Security, and Sensing*, Oak Ridge, 2013.

[204] J. Mireles, Process Study and Control of Electron Beam Melting Technology Using Infrared Thermography, Open Access Theses & Dissertations (2013) 1682.

[205] J. Raplee, A. Plotkowski, M. M. Kirka, R. Dinwiddie, A. Okello, R. Dehoff and S. S. Babu, "Thermographic Microstructure Monitoring in Electron Beam Additive Manufacturing," *Scientific Reports,* vol. 7, no. 1 (43554), 2017.

[206] E. Rodriguez, F. Medina, D. Espalin, C. Terrazas, D. Muse, C. Henry, E. MacDonald, R.B. Wicker, Integration of a Thermal Imaging Feedback Control System in Electron Beam Melting, Mater. Sci. (2012) 945–961.

[207] S. Price, K. Cooper and K. Chou, "Evaluations of Temperature Measurements by Near-Infrared Thermography in Powder-based Electron-beam Additive Manufacturing," in *23rd Annual International Solid Freeform Fabrication Symposium*, Austin, TX, 2012.

[208] S. Price, J. Lydon, K. Cooper and K. Chou, "Experimental temperature analysis of powder-based electron beam additive manufacturing," in *24th International Solid Freeform Fabrication Symposium*, Austin, TX, 2013.

[209] X. Gong, B. Cheng, S. Price and K. Chou, "Powder-bed Electron-beam-melting Additive Manufacturing: Powder Characterization, Process Simulation and Metrology," in *ASME Early Career Technical Journal*, Birmingham, Alabama, USA, 2013.

[210] S. Ridwan, J. Mireles, S. Gaytan, D. Espalin and R. Wicker, "Automatic Layerwise Acquisition of Thermal and Geometric Data of the Electron Beam Melting Process Using Infrared Thermography," in *International Symposium of Solid Freeform Fabrication*, 2014.

[211] J. Mireles, C. Terrazas, S.M. Gaytan, Closed-loop automatic feedback control in electron beam melting, Int. J. Adv. Manuf. Technol. 78 (2015) 1193–1199.

[212] J. Mireles, S. Ridwan, P. A. Morton, A. Hinojos and R. B. Wicker, "Analysis and correction of defects within parts fabricated using powder bed fusion technology," *Surface Topography: Metrology and Properties,* vol. 3 (034002), 2015.

[213] O. Holzmond, X. Li, In situ real time defect detection of 3D printed parts, Addit. Manuf. 17 (2017) 135–142.

[214] J. Yang, J. Han, H. Yu, J. Yin, M. Gao, Z. Wang, X. Zeng, Role of molten pool mode on formability, microstructure and mechanical properties of selective laser melted Ti-6Al-4V alloy, Mater. Des. 110 (2016) 558–570.

[215] D. Chen, P. Wang, R. Pan, C. Zha, J. Fan, S. Kong, N. Li, J. Li, Z. Zeng, Research on in situ monitoring of selective laser melting: a state of the art review, The International Journal of Advanced Manufacturing Technology (2021).

[216] S. Clijsters, T. Craeghs and J.-p. Kruth, "A priori process parameter adjustment for SLM process optimization," in *Innovative developments on virtual and physical prototyping*, Leuven, Belgium, 2012.

[217] S. Mirzababaei, B.K. Paul, S. Pasebani, Metal Powder Recyclability in Binder Jet Additive Manufacturing, JOM 72 (9) (2020) 3070–3079.

[218] B. Fullenwider, P. Kiani, J. M. Schoenung and K. Ma, "From Recycled Machining Waste to Useful Powders for Metal Additive Manufacturing," in *REWAS 2019 Manufacturing the Circular Materials Economy*, Vols. The Minerals, Metals & Materials Series, Springer Nature, 2019, pp. 3-8.

[219] A. Averardi, C. Cola, Z. E. Steven and N. Gupta, "Effect of particle size distribution on the packing of powder beds: A critical discussion relevant to additive manufacturing," *Materials Today Communications,* vol. 24 (100964), 2020.

[220] S. Clijsters, T. Craeghs, M. Moesen and J.-p. Kruth, "Optimization of thin wall structures in SLM," in *Direct Digital Manufacturing Conference*, Fraunhofer, Berlin, 2012.

[221] Y. Zhang, S. Yang, Y.F. Zhao, Manufacturability analysis of metal laser-based powder bed fusion additive manufacturing - a survey, The International Journal of Advanced Manufacturing Technology 110 (2020) 57–78.

[222] L. Thijs, F. Verhaeghe, T. Craeghs, J. Van Humbeeck, J.-P. Kruth, A study of the microstructural evolution during selective laser melting of Ti-6Al-4V, Acta Mater. 58 (2010) 3303–3312.

[223] P. Jin, H. Sumeng, W. Xingxing, W. Jiansheng and Z. Furong, "Effect of Filler Metal on Three-Dimensional Transient Behavior of Keyholes and Molten Pools in Laser Welding," *Chinese Journal of Lasers,* vol. 45, no. 1 (0102003), 2018.

[224] P. Bidare, I. Bitharas, R. Ward, M. Attallah, A. Moore, Fluid and particle dynamics in laser powder bed fusion, Acta Mater. 142 (2018) 107–120.

[225] J. Peng, L. Li, S. Lin, F. Zhang, Q. Pan and S. Katayama, "High-Speed X-Ray Transmission and Numerical Study of Melt Flows inside the Molten Pool during Laser Welding of Aluminum Alloy," *Mathematical Problems in Engineering,* vol. (1409872), 2016.

[226] H. Nakamura, Y. Kawahito, K. Nishimoto and S. Katayama, "Elucidation of melt flows and spatter formation mechanisms during high power laser welding of pure titanium," *Journal of Laser Applications,* vol. 27, no. 3 (032012), 2015.

[227] S. Shevchik, T. Le-Quang, B. Meylan, F. V. Farahani, M. P. Olbinado, A. Rack, G. Masinelli, C. Leinenbach and K. Wasmer, "Supervised deep learning for real-time quality monitoring of laser welding with X-ray radiographic guidance," *Scientific Reports,* vol. 10 (3389), 2020.

[228] S.A. Khairallah, A.T. Anderson, A. Rubenchik, W.E. King, Laser powder-bed fusion additive manufacturing: Physics of complex melt flow and formation mechanisms of pores, spatter, and denudation zones, Acta Mater. 108 (2016) 36–45.

[229] G. B. Bang, W. R. Kim, H. K. Kim, H.-K. Park, G. H. Kim, S.-K. Hyun, O. Kwon and H. G. Kim, "Effect of process parameters for selective laser melting with SUS316L on mechanical and microstructural properties with variation in chemical composition," *Materials and Design,* vol. 197 (109221), 2021.

[230] "How process parameters drive successful metal AM part production," *Metal Additive Manufacturing,* vol. 4, no. 2, pp. 127-135, Summer 2018.

[231] J. Liu, Y. Song, C. Chen, X. Wang, H. Li, C. Zhou, J. Wang, K. Guo and J. Sun, "Effects of scanning speed on the microstructure and mechanical behavior of 316L stainless steel fabricated by selective laser melting," *Materials and Design,* vol. 186 (108355), 2020.

[232] J. Li, L. Cao, J. Xu, S. Wang and Q. Zhou, “In situ porosity intelligent classification of selective laser melting based on coaxial monitoring and image processing,” *Measurement,* vol. 187 (110232), 2022.
[233] P. Lott, H. Schleifenbaum, W. Meiners, K. Wissenbach, C. Hinke, J. Bultmann, Design of an Optical system for the In Situ Process Monitoring of Selective Laser Melting (SLM), Physics Procedia 12 (2011) 683–690.
[234] V. Vavilov and D. Burleigh, Infrared Thermography and Thermal Nondestructive Testing, Springer Nature Switzerland AG, 2020.
[235] P. Bidare, R. Maier, R. Beck, J. Shephard, A. Moore, An open-architecture metal powder bed fusion system for in-situ process measurements, Addit. Manuf. 16 (2017) 177–185.
[236] B. Wisner, K. Mazur, V. Perumal, K. Baxevanakis, L. An, G. Feng, A. Kontsos, Acoustic emission signal processing framework to identify fracture in aluminum alloys, Eng. Fract. Mech. 210 (2019) 367–380.
[237] J. Liu, Y. Hu, B. Wu, Y. Wang, An improved fault diagnosis approach for FDM process with acoustic emission, J. Manuf. Processes 35 (2018) 570–579.
[238] S.W. Smith, The Scientist and Engineer’s Guide to Digital Signal Processing, San Diego, California Technical Publishing, California, 1999.
[239] M. Sezgin, B. Sankur, Survey over image thresholding techniques and quantitative performance evaluation, J. Electron. Imaging 13 (1) (2004) 146–165.
[240] S. A. Gold and T. G. Spears, “Acoustic Monitoring Method for Additive Manufacturing Processes”. Patent US 20170146488A1, 25 May 2017.
[241] M. R. Redding, S. A. Gold and T. G. Spears, “Non-contact acoustic inspection method for additive manufacturing processes”. Patent US20170146489A1, 25 May 2017.
[242] O. Kwon, H.G. Kim, M.J. Ham, W. Kim, G.-H. Kim, J.-H. Cho, K. Kim, N.L. Kim, A deep neural network for classification of melt-pool images in metal additive manufacturing, J. Intell. Manuf. 31 (2020) 375–386.
[243] M.F. Khan, A. Alam, M.A. Siddiqui, M.S. Alam, Y. Rafat, N. Salik, I. Al-Saidan, Real-time defect detection in 3D printing using machine learning, Mater. Today:. Proc. 42 (2021) 521–528.
[244] V. Pandiyan, R. Drissi-Daoudi, S. Shevchik, G. Masinelli, T. Le-Quang, R. Loge and K. Wasmer, “Deep transfer learning of additive manufacturing mechanisms across materials in metal-based laser powder bed fusion process,” *Journal of Materials Processing Tech.,* vol. 303 (117531), 2022.
[245] K. Wasmer, T. Le-Quang, B. Meylan, S. Shevchik, In Situ Quality Monitoring in AM Using Acoustic Emission: A Reinforcement Learning Approach, J. Mater. Eng. Perform. 28 (2019) 666–672.
[246] G.L. Chen, K. Yanamandra, N. Gupta, Artificial Neural Networks Framework for Detection of Defects in 3D-Printed Fiber Reinforcement Composites, JOM (2021).
[247] A. Marro, T. Bandukwala, W. Mak, Three-Dimensional Printing and Medical Imaging: A Review of the Methods and Applications, Curr. Probl. Diagn. Radiol. 45 (2016) 2–9.
[248] I. Campioni and N. Gupta, “Ti6Al4V mandibular devices by additive manufacturing: Assessment of as-built quality,” *Med Devices Sens.,* vol. 4 (e10153), 2021.
[249] M.R. Khosravani, T. Reinicke, On the Use of X-ray Computed Tomography in Assessment of 3D-Printed Components, J. Nondestr. Eval. 39 (2020).
[250] A. Thompson, I. Maskery and R. Leach, “X-ray computed tomography for additive manufacturing: a review,” *Meas. Sci. Technol.,* vol. 27 (072001), 2016.
[251] X. Wang, L. Zhao, J.Y.H. Fuh, H.P. Lee, Effect of Porosity on Mechanical Properties of 3D Printed Polymers: Experiments and Micromechanical Modeling Based on X-ray Computed Tomography Analysis, Polymers 11 (2019) 1154.
[252] V. Aloisi and S. Carmignato, “Influence of surface roughness on X-ray computed tomography dimensional measurements of additive manufactured parts,” *Case Studies in Nondestructive Testing and Evaluation,* Vols. 6, Part B, pp. 104-110, 2016.
[253] A. Townsend, L. Pagani, P. Scott, L. Blunt, Areal surface texture data extraction from X-ray computed tomography reconstructions of metal additively manufactured parts, Precis. Eng. 48 (2017) 254–264.
[254] S. Siddique, M. Imran, M. Rauer, M. Kaloudis, E. Wycisk, C. Emmelmann, F. Walther, Computed tomography for characterization of fatigue performance of selective laser melted parts, Mater. Des. 83 (2015) 661–669.
[255] Y. Hu, S. Wu, P. Withers, J. Zhang, H. Bao, Y. Fu and G. Kang, “The effect of manufacturing defects on the fatigue life of selective laser melted Ti-6Al-4V structures,” *Materials and Design,* vol. 192 (108708), 2020.
[256] A. Sombatmai, V. Uthaisangsuk, S. Wongwises and P. Promoppatum, “Multiscale investigation of the influence of geometrical imperfections, porosity, and size-dependent features on mechanical behavior of additively manufactured Ti-6Al-4V lattice struts,” *Materials & Design,* vol. 209 (109985), 2021.
[257] N.E. Gorji, R. O’Connor, D. Brabazon, X-ray Tomography, AFM and Nanoindentation Measurements for Recyclability Analysis of 316L Powders in 3D Printing Process, Procedia Manuf. 47 (2020) 1113–1116.
[258] B. Zhang, S. Liu, Y.C. Shin, In-Process monitoring of porosity during laser additive manufacturing process, Addit. Manuf. 28 (2019) 497–505.
[259] A. du Plessis, S.G. le Roux, J. Els, G. Booysen, D.C. Blaine, Application of microCT to the non-destructive testing of an additive manufactured titanium component, Case Stud. Nondestr.Test. Eval. 4 (2015) 1–7.
[260] S. Tammas-Williams, H. Zhao, F. Leonard, F. Derguti, I. Todd, P. Prangnell, XCT analysis of the influence of melt strategies on defect population in Ti-6Al-4V components manufactured by Selective Electron Beam Melting, Mater. Charact. 102 (2015) 47–61.
[261] H. Choo, K.-L. Sham, J. Bohling, A. Ngo, X. Xiao, Y. Ren, P. J. Depond, M. J. Matthews and E. Garlea, “Effect of laser power on defect, texture, and microstructure of a laser powder bed fusion processed 316L stainless steel,” *Materials and Design,* vol. 164 (107534), 2019.
[262] M. Bacak, J. Valsecchi, J. Capek, E. Polatidis, A. Kaestner, A. Arabi-Hashemi, I. Kruk, C. Leinenbach, A. Long, A. Tremsin, S. Vogel, E. Watkins and M. Strobl, “Neutron dark-field imaging applied to porosity and deformation-induced phase transitions in additively manufactured steels,” *Materials and Design,* vol. 195 (109009), 2020.
[263] F. Medel, V. Esteban and J. Abad, “On the use of laser-scanning vibrometry for mechanical performance evaluation of 3D printed specimens,” *Materials & Design,* vol. 205 (109719), 2021.
[264] O.K. Bowoto, B.I. Oladapo, S.A. Zahedi, F.T. Omigbodun, O.P. Emenuvwe, Analytical modelling of in situ layer-wise defect detection in 3D-printed parts: additive manufacturing, The International Journal of Advanced Manufacturing Technology 7–8 (2020) 2311–2321.
[265] H. Pearce, K. Yanamandra, N. Gupta and R. Karri, “FLAW3D: A Trojan-based Cyber Attack on the Physical Outcomes of Additive Manufacturing. arXiv: 2104.09562,” 2021.
[266] M. Wu, Z. Song, Y.B. Moon, Detecting cyber-physical attacks in CyberManufacturing systems with machine learning methods, J. Intell. Manuf. 30 (2019) 1111–1123.
[267] L.D. Sturm, C.B. Williams, J.A. Camelio, J. White, R. Parker, Cyber-physical vulnerabilities in additive manufacturing systems: A case study attack on the. STL file with human subjects, J. Manuf. Syst. 44 (2017) 154–164.
[268] M. Wu, V.V. Phoha, Y.B. Moon, A.K. Belman, “Detecting Malicious Defects in 3D Printing Process Using Machine Learning and Image Classification, ASME 2016 International Mechanical Engineering Congress and Exposition Phoenix (2016).
[269] X. Feng and F. Xue, “Characterization of 3D printed bolts based on digital image correlation and infrared thermography,” *Materials and Design,* vol. 191 (108641), 2020.
[270] F.G. Cunha, T.G. Santos, J. Xavier, In Situ Monitoring of Additive Manufacturing Using Digital Image Correlation: A Review, Materials 14 (2021) 1511.